5-2018

Development of Targeted Pro-Angiogenic Therapies for Ischemic Diabetic Foot Ulcer Repair

Jenny B. Lin
Purdue University

Recommended Citation
Lin, Jenny B., "Development of Targeted Pro-Angiogenic Therapies for Ischemic Diabetic Foot Ulcer Repair" (2018). *Open Access Dissertations*. 1760.
https://docs.lib.purdue.edu/open_access_dissertations/1760

DEVELOPMENT OF TARGETED PRO-ANGIOGENIC THERAPIES FOR ISCHEMIC DIABETIC FOOT ULCER REPAIR

by

Jenny B. Lin

A Dissertation

Submitted to the Faculty of Purdue University

In Partial Fulfillment of the Requirements for the degree of

Doctor of Philosophy

Weldon School of Biomedical Engineering

West Lafayette, Indiana

May 2018

THE PURDUE UNIVERSITY GRADUATE SCHOOL
STATEMENT OF COMMITTEE APPROVAL

Dr. Alyssa Panitch, Ph.D., Chair
    Weldon School of Biomedical Engineering
    Purdue University
    University of California, Davis
Dr. Sherry L. Voytik-Harbin, Ph.D.
    Weldon School of Biomedical Engineering
    Purdue University
Dr. Lynetta J. Freeman, DVM, MS, MBA
    Department of Veterinary Clinical Sciences,
    Weldon School of Biomedical Engineering
    Purdue University
Dr. J. Kent Leach, Ph.D.
    Department of Biomedical Engineering
    University of California, Davis

Approved by:
    Dr. George R. Wodicka, Ph.D.
        Head of the Graduate Program

For my parents, who taught me to always strive for excellence

ACKNOWLEDGMENTS

This work would not have been possible without all those supporting me including my friends and family, my lab-mates, my major advisor, and a whole scientific community. It would be impossible to enumerate them all, but I would like to highlight several whose contributions were especially instrumental in my success.

Firstly, I would like to acknowledge those that encouraged me to explore research, led me in pursuit of a PhD, and believed in my abilities as a researcher. I would like to thank my parents for their support in this long journey and for inspiring me to pursue science from a young age. I also thank Dr. Joyce Wong for helping me develop my confidence and independence as a researcher beginning as an undergraduate research assistant and then directing my own studies as a post-baccalaureate visiting scientist. Finally, I would like to thank my boyfriend Jim for always believing in my ability to succeed and supporting me along the way.

For their expertise and guidance in my research training, I acknowledge my committee members, Drs. Alyssa Panitch, Sherry Voytik Harbin, Lynetta Freeman, and Kent Leach. I am especially thankful for Dr. Panitch's continual optimism even amidst confusing data, which was most influential to my persistence in conducting repeated experiments. Additionally, the new insights and directions of our pro-angiogenic decorin mimic work would not have been possible without the ingenuity of Drs. Kit Lam, Aijun Wang, and Ruiwu Liu and their studies on the cyclic RGD peptide 'LXW7'. I would also like to thank Dr. Scott Poh for his initial guidance in mastering manual peptide synthesis and his collaboration on degradable nanoparticles. Collagen-binding nanoparticles and matrigel angiogenesis studies were performed in collaboration with Drs. James McMasters and Ben Hung, respectively, and both Dr. McMasters and Dr. Hung were particularly helpful in editing my writing. Finally, I also thank Sean Batten for his help in performing and analyzing the *in vivo* CAM assays, as well as Kevin Campbell for helping me learn the techniques needed to perform *ex ovo* CAM assays.

The joint Medical Scientist Training Program at Indiana University School of Medicine and Purdue University Biomedical Engineering, and directors Drs. Maureen Harrington and Raghu Mirmira have always been supportive in my endeavors and continually committed to my success. A special thank you is also due to administrators Jan Receveur, Sandra May, Linda Doyle, Tammy Siemers, and other staff members at IUPUI and Purdue who take care of

finances, scheduling, and logistics so that I can focus on my graduate studies and professional development. Lastly, I also acknowledge my funding sources supporting my graduate work: NIAMS R01, NIH Diabetes T32 fellowship, Indiana Clinical Translational Sciences Institute fellowship, and Purdue University’s Bilsland fellowship.

TABLE OF CONTENTS

LIST OF TABLES

LIST OF FIGURES

LIST OF ABBREVIATIONS

aFGF, bFGF, acidic and basic fibroblastic growth factor

AAc, Acrylic Acid

AGE, Advanced Glycation End-product

AMPS, 2-acrylamido-2-methyl-1-propanesulfonic acid

AU, arbitrary units

BAC, N,N'-bis(acryloyl)cystamine (disulfide crosslinker)

BMPH, N-β-Maleimidopropionic acid hydrazide

BSA, bovine serum albumin

CAM, Chorioallantoic membrane

CD, circular dichroism

DCM, dichloromethane

DFU, diabetic foot ulcer

DIPEA, diisopropylethylamine

DMF, dimethylformamide

DMHA, N,O-dimethacryloylhydroxylamine

DMSO, dimethyl sulfoxide

DMTMM, (4-(4,6-dimethoxy-1,3,5-triazin-2-yl)-4-methyl-morpholinium chloride)

DS, dermatan sulfate

DTT, dithiothreitol

EBM, endothelial basal medium

EC, endothelial cell

ECM, extracellular matrix

EDC, 1-ethyl-3-(-3-dimethylaminopropyl) carbodiimide hydrochloride

EGF, epidermal growth factor

eNOS, endothelial nitric oxide synthase

EPC, endothelial progenitor cell

Fmoc, fluorenylmethyloxycarbonyl

GAG, glycosaminoglycan

HMVEC, human microvascular endothelial cells

HUVEC, human umbilical endothelial cells

IGF, insulin-like growth factor

i-PrOH, isopropyl alcohol

KGF, keratinocyte growth factor

LCST, lower critical solution temperature

MBA, N,N’-methylenebisacrylamide

MK2, MAPK-activated protein kinase 2

MMC, mitomycin C

MMP, matrix metalloproteinase

MWCO, molecular weight cut off

NG, pNIPAM-AMPS nanogel

NGMBA, non-degradable pNIPAM-AMPS-MBA

NGPEGMBA, nondegradable PEGylated-pNIPAM-AMPS-MBA

NGPEGSS, PEGylated-pNIPAM-AMPS-disulfide

NGPEGSS, PEGylated-pNIPAM-AMPS-disulfide

NGPEGSSF, PEGylated-pNIPAM-AMPS-disulfide-fluorescein

NGSS, pNIPAM-AMPS-disulfide

NGSSF, pNIPAM-AMPS-disulfide-fluorescein

NMR, nuclear magnetic resonance

OPA, ophthalaldehyde

PBS, phosphate buffered saline

PDGF, platelet derived growth factor

PDGFR, PDGF receptor

PEG, polyethyleneglycol

PEGDA, PEG diacrylate

PLGA, poly(lactic-co-glycolic acid)

PVD, peripheral vascular disease

SS, disulfide crosslinker

TFA, trifluoroacetic acid

TIPS, triisopropylsilane

UV, ultraviolet

VEGF, vascular endothelial growth factor

VEGFR2, VEGF receptor 2

ABSTRACT

Author: Lin, Jenny, B. PhD
Institution: Purdue University
Degree Received: May 2018
Title: Development of Targeted Pro-angiogenic Therapies for Ischemic Diabetic Foot Ulcer Repair.
Major Professor: Alyssa Panitch

Between 15-25% of diabetic patients develop chronic foot ulcers within their lifetime. These ulcers are characterized by delayed wound healing, are highly susceptible to infection, and can lead to lower-limb/foot amputation. Impaired ulcer healing is most often due to ischemia and insufficient formation of new vessels in the wound bed, as well as rapid turnover of healing tissue by excessive matrix metalloproteinase (MMP) activity. To improve healing of chronic ischemic wounds, researchers have sought to increase angiogenesis at the wound site using growth factors such as vascular endothelial growth factor (VEGF). VEGF is a key angiogenic mediator and uniquely participates in multiple aspects of wound healing including revascularization, re-epithelialization, and collagen deposition. However, the clinical success of growth factor therapies such as VEGF has been limited largely due to the overexpression MMPs in the wound environment that degrade or inactivate the growth factors. Furthermore, non-targeted angiogenic growth factor therapies raise significant concerns because they are not restricted to the wound site, but potentially diffuse into systemic circulation and cause malignancies.

This thesis reviews current advances in understanding the pathogenesis and pathophysiology of the compromised wound healing environment leading to DFUs with particular emphasis on the roles of neovascularization and matrix remodeling. It also addresses recent progress in VEGF therapy for DFUs and the current limitations in clinical translation imposed by co-existing pathophysiological defects of diabetic wound healing. Given the current understanding of the impaired healing components suggesting a need to correct multiple derangements while maintaining efficacy in the complex and highly proteolytic environment, we propose multiple collagen-targeted, degradation resistant, proangiogenic therapies to activate and potentiate VEGF pathways and simultaneously protect existing collagen matrices. Specifically, we discuss the development of VEGF-loaded collagen-binding nanoparticles and two variants of engineered

decorin mimetics functionalized with pro-angiogenic VEGF-mimicking or αvβ3 integrin-binding peptides to increase vascularization of the wound bed. Both the nanoparticles and the angiogenic proteoglycan mimics can be targeted to endogenous collagen or exogenous collagen dressings by a collagen-binding peptide and could be used in combination to exploit VEGF activation and potentiation. This project (i) develops a thermosensitive nanoparticle VEGF-delivery system, (ii) develops and characterizes pro-angiogenic peptide-functionalized decorin mimics, and (iii) assesses the *in vitro* and *in vivo* angiogenic potential of these pro-angiogenic decorin mimics as proof-of-concept supporting their potential to accelerate ischemic dermal wound healing in animal models.

1. INTRODUCTION: COMPLEX PATHOPHYSIOLOGY OF IMPAIRED CUTANEOUS WOUND HEALING IN DIABETES POSES BARRIERS TO TRANSLATION OF ANGIOGENIC GROWTH FACTORS

1.1 *Significance and Epidemiology: Diabetic Foot Ulcers*

In 2015, the Center for Disease Control and Prevention estimated a population of 30.3 million diabetic Americans (1), up to 25% of whom will develop diabetic foot ulcers (DFUs) in their lifetime (2, 3). The majority of DFUs, which affect both type I and type II diabetics, develop from a combination of peripheral neuropathy and vascular insufficiency (ischemia) and are thus categorized to have mixed neuropathic and ischemic pathologies (4, 5). Deficits in the macro- and microcirculation are a major factor leading to delayed wound healing (6), and DFUs with an ischemic component caused by concurrent peripheral vascular disease (PVD) and/or microangiopathy are more severe with higher mortality rates (4, 5). Non-healing foot ulcers are prone to serious infections requiring limb amputation; in fact, diabetic complications account for the majority of non-traumatic lower-limb amputations (1, 7) with 5-24% of DFUs leading to lower-limb amputation 6-18 months after the initial evaluation (4). Moreover, ulcers and other foot complications comprise 20% of diabetes-related hospitalizations and thus represent a significant health burden in the United States (8). Accelerating DFU healing would reduce the need for lower-limb amputation, improve survival of patients suffering from DFUs, and decrease diabetes-related hospitalizations.

1.2 *Current Treatments for Non-Healing Chronic Diabetic Foot Ulcers*

The current gold standard for DFU treatment includes wound debridement, antibiotic management of infection, off-loading of the ulcer, and revascularization surgeries if indicated (4, 9). Although many wound dressings are available to protect the DFU and promote a moist environment (10), the efficacy of such wound dressings in DFU healing remains unclear (11); a meta-analysis of recent randomized control trials using advanced wound dressings alone (ie. without growth factors or living cellular components) showed no significant advantages for advanced dressings, such as alginate, over basic wound care (11). If 1 month of traditional management provides insufficient healing, additional advanced DFU therapies including cell-based skin replacements, such as Dermagraft (12) and Apligraf (13), or growth factor therapies, such as Regranex (14) may be indicated. However, only Apligraf is FDA approved for ischemic DFU. Currently, clinically effective DFU treatments, specifically those applicable to ischemic DFUs, remain a significant concern, but developing these treatments has been complicated by the multiple concurrent defects in the DFU environment. These pathophysiological barriers are exemplified by the limited successes in clinical translation of angiogenic growth factor therapies. Future therapies may be more successful if they are combination treatments that take into account the interrelationships between inflammation, angiogenesis, and ECM remodeling.

1.3 *Impaired Neovascularization in Diabetic Wound Healing*

Diabetes is known to impair post-ischemic neovascularization in multiple parts of the body, including the lower-limbs (24, 25). This decreased ability to create new blood vessels severely affects the proliferation/granulation phase of wound healing, which requires angiogenesis to sustain actively proliferating fibroblasts and keratinocytes. Specifically, vascular endothelial growth factor (VEGF) appears to be crucial to granulation since its neutralization causes a severe healing defect (26). Reduced neovascularization in diabetics has been attributed to dysregulation and insufficient levels of angiogenic growth factors (27) (VEGF (28-30), EGF (31), aFGF and bFGF (31, 32), KGF (32), or PDGF (30, 33-35)), endothelial dysfunction with reduced angiogenic response (36), and reduced endothelial progenitor cell recruitment (37-39).

1.3.1 Cell Dysfunction Leads to Insufficient and Uncoordinated Angiogenic Signals

The regulation of both growth factor levels and timing of induction are important in orchestrating wound repair and are abnormal in diabetic wounds. Many cells, including macrophages, keratinocytes, fibroblasts, and endothelial cells, normally secrete angiogenic growth factors, such as PDGF, VEGF, EGF, aFGF, bFGF, and KGF, to mediate the wound healing process (15-17). However, cellular dysfunction within the diabetic wound bed causes both uncoordinated and decreased levels of these growth factors. For example, endogenous PDGF and PDGFR are both decreased in diabetic wounds compared to acute wounds (18, 19). VEGF production in the diabetic wound bed is also reduced due to multiple factors, including reduced expression in diabetic keratinocytes (20), reduced production by diabetic fibroblasts (21, 22), reduced production by diabetic macrophages (23, 24). Diabetes was shown to decrease HIF-1α transactivation, leading to blunted VEGF-induction after hypoxia (21, 22). In diabetic mouse models, wound keratinocytes exhibit reduced induction of FGFs (25, 26). DFU skin biopsies also show that both keratinocytes and endothelial cells at the DFU margin also fail to upregulate VEGF and VEGFR2, PDGF and PDGFR, EGFR, IGF-1, and NOS2 (27).

Given these derangements in growth factor release profiles, many researchers have investigated angiogenic factor supplementation to alleviate impaired healing. Numerous studies show the benefits of angiogenic growth factor supplementation in wound healing in diabetic rodent models, but only PDGF has proven sufficient clinical efficacy in diabetic patients (28, 29).

1.3.2 Endothelial Dysfunction Decreases Angiogenic Responsiveness

Diabetes is a well-known cause of endothelial dysfunction, which encompasses a broad variety of dysregulated endothelial functions, including diminished ability to mediate vasodilation, disrupted intimal layer barrier function, abnormal leukocyte recruitment and diapedesis, decreased proliferation and migration, and abnormal angiogenic responses (30).

In addition to insufficient growth factor levels, impaired neovascularization in diabetics is compounded by endothelial dysfunction, reflected by decreased responsiveness to local growth factors and exemplified by decreased proliferation and migration (30-33) and increased apoptosis (34, 35) in endothelial cells cultured in hyperglycemic media. Decreased endothelial proliferation in diabetics can, at least in part, be attributed to accelerated accumulation of advanced glycation end-products (AGEs) and oxidative stress signaling through receptor for AGEs (RAGE) to decrease endothelial responsiveness to angiogenic factors (36-38). For example, RAGE-mediated VEGFR2 degradation subsequently attenuates signaling transduction of VEGF (38). It is apparent then that introducing greater levels of growth factors might not adequately compensate for decreased angiogenic responses if the number of receptors is reduced and all receptors are saturated. It follows that therapeutic modulation of increasing overall receptor levels and/or decrease degradation of receptors may be necessary in conjunction to administering increased growth factors to achieve appropriate angiogenic responses.

1.3.3 Reduced Endothelial Progenitor Cell Recruitment and Pro-Angiogenic Paracrine Signaling Capacity

During tissue granulation, both local endothelial cells and bone marrow-derived endothelial progenitor cells (EPCs) participate in neovascularization. Exogenously administered EPCs have been shown to accelerate wound closure in diabetic mice by incorporating into the vasculature and increasing angiogenesis and granulation (39). Endogenous EPCs mobilize into systemic circulation through VEGF-induced endothelial nitric oxide synthase (eNOS) activation (39, 40) and are recruited to the wound by SDF-1α, where they promote angiogenesis by expressing high levels of VEGF and bFGF (39, 40). In diabetes, EPCs have both impaired mobilization (due to reduced eNOS activity) and homing (due to reduced SDF-1α at the wound), resulting in fewer EPCs present in circulation (41-43) and at the wound site (43), respectively. Furthermore, EPCs successfully homing to the wound site may fail in paracrine signaling, as HUVECs exposed to diabetic-EPC-conditioned media display reduced tube formation in comparison to their non-diabetic media equivalents (42). Clinical studies of EPCs harvested from diabetic patients support this notion of EPC dysfunction in the diabetic environment (44), which is mediated by oxidative stress resulting from inappropriately reduced eNOS activity (45).

1.4 *Dysregulated ECM Remodeling in Diabetic Wound Healing*

The ECM serves multiple essential purposes within a healing wound, as it both regulates growth factor levels through binding and provides a support for cell attachment and proliferation (46). A balance in ECM synthesis by parenchymal cells and ECM degradation by MMPs is integral to successful wound closure, and this balance is disturbed in diabetes.

1.4.1 Abnormal ECM Synthesis

Several growth factors including TGF-β, IGF, PDGF, EGF, and FGF are involved in promoting ECM synthesis (47, 48). Many studies have shown that collagen, a predominant skin ECM component, is reduced and abnormally organized in the diabetic wound (47, 49-52), leading to decreased tensile strength in both uninjured (53) and injured (47, 54) diabetic skin. *Bitar et al.* showed that the reduction in tensile strength of wounded skin directly correlated with the induction of diabetes by STZ in a diabetic rat model and is partially restored by a single application of TGF-β (47), indicating the importance of growth factors such as TGF-β and IGF in maintaining appropriate ECM levels in wounded tissue (47). Interestingly, while TGF-β and IGF levels were decreased in diabetic wounds, transcription of TGF-β was actually increased, suggesting post-transcriptional inhibition of TGF-β expression (49). Since TGF-β also inhibits collagenase induction by other growth factors (EGF and bFGF) and synergistically increases TIMP expression(55), decreased TGF-β may also reduce TGF-β-mediated collagenase suppression, contributing to increased collagenase activity.

Since fibroblasts are the main cells involved in collagen synthesis, another possible source of dysregulated collagen synthesis is diabetic fibroblast dysfunction. For example, fibroblasts isolated from DFU have exhibited decreased response to growth factors (56) and hypoxia (21) and have impaired proliferation, indicating a change to a senescent phenotype (57-60). Work by *Hehenberger et al.* suggests that factors specific to the diabetic wound are responsible for this dysfunction, since fibroblasts from uninjured skin (both diabetic and non-diabetic) have the same proliferation rates (58). Fibroblasts from uninjured skin of diabetic mice also did not have impaired proliferation, but did show reduced migration (21), indicating that even though fibroblast proliferation is not affected by diabetes, other baseline diabetic fibroblast defects may be present.

Research also suggests there is a pre-existing abnormality in ECM maintenance that predisposes diabetic skin to injury and may propagate through to impair the wound healing process (49, 53). *Bermudez et al.* has shown that the total collagen content of dermal ECM is reduced in uninjured diabetic skin (53), which *Caskey et al.* suggests is due to posttranscriptional repression by miRNA-25 and miRNA-29a (49). Collagen glycation may also account for unstable collagen, since glycated collagen correlates strongly with collagenase activity leading to accelerated collagen breakdown (52) and has been shown to delay wound healing, decrease biomechanical properties, and decrease deposition of other ECM proteins, like fibronectin and elastin (61).

The ECM serves multiple essential purposes within a healing wound, as it both regulates growth factor levels through binding and provides a support for cell attachment and proliferation (46). A balance in ECM synthesis by parenchymal cells and ECM degradation by MMPs is integral to successful wound closure, and this balance is disturbed in diabetes. This suggests that an exogenous ECM tissue replacement such as a supplemental collagen matrix that integrates into the healing wound may be beneficial in improving ECM organization and integrity.

1.4.2 Excessive Metalloproteinase Activity

Although normal acute wound healing involves MMP induction in the wound environment (62, 63), many studies have implicated excessive and prolonged (64) MMP activity (specifically MMP-2, MMP-8, and MMP-9) in non-healing DFUs (65-72); elevated MMP-9 (66, 67, 70, 73, 74) in DFU has been shown to predict poor healing. Other groups have additionally identified an elevated ratio of MMP-9 to TIMP-1 as a predictor of the non-healing state (65) and an elevated ratio of MMP-1 to TIMP-1 as a predictor of successful healing (66). Similar MMP imbalances have been identified in diabetic wounds (47, 64) and uninjured skin fibroblasts (21) from diabetic rodent models. Furthermore, expression of TIMP-2 is reduced in DFU (68), and TIMP-3 reduction was found to be specific for ischemic but not neuropathic DFUs (75). These altered protease and protease inhibitor levels result in accelerated degradation and excessive turnover of healing tissue and essential growth factors responsible for coordinating wound resolution (47). Modulation of these MMPs has been shown to increase collagen synthesis and improve healing in diabetic rodent models (76-78).

Elevated MMP levels may arise from diabetes-induced abnormalities of parenchymal cells. Recently, keratinocytes were found to upregulate MMP-9 transcription through loss of focal adhesion kinase (FAK) signaling within epithelium and also cause fibroblast downregulation of TIMP1 in a paracrine manner (79). This mechanism may be relevant to diabetic wound healing since hyperglycemia (80) and glycoaldehyde-modified AGE-BSA (81) have been found to impair FAK activation and results in a corresponding increase in MMP-9 after exposure to AGE-BSA (81). In another example, uninjured diabetic fibroblasts are found to secrete twice the normal amount of latent pro-MMP-9, although active MMP-9 is not significantly elevated from non-diabetic controls (21). However, within the first 4 days of injury in diabetic mouse wounds, significantly higher levels of activated MMP-9 are observed (64). The increased basal levels of pro-MMP-9 in diabetics likely serve as an abundant depot that converts to the activated form upon injury. Together decreased synthesis of ECM and accelerated degradation in the diabetic environment leads to excessive turnover of healing tissue and MMP-susceptible growth factors.

1.5 *VEGF for Therapeutic Angiogenesis and Barriers to Clinical Translation*

1.5.1 The Promise of VEGF Therapy for Ischemic DFU

To improve ischemic DFU healing, researchers have sought to stimulate angiogenesis by increasing growth factors at the wound site, in hope of restoring blood flow and improving the formation of granulation tissue (a loose fibrovascular tissue characterized by blood vessels, collagen, and fibroblasts) in the healing process. VEGF has been identified as one of the most potent and rate-limiting angiogenic factors (82) especially integral to the response to ischemia (83), while simultaneously acting on keratinocytes and fibroblasts to stimulate re-epithelialization and collagen deposition within the treated area (84-86). VEGF therefore uniquely participates in multiple aspects of wound healing, including angiogenesis, epithelialization, and collagen deposition during tissue granulation (85). Furthermore, defective angiogenesis may result, at least in part, from a combination of reduced VEGF levels and/or decreased VEGF receptor expression. Currently, VEGF supplementation has shown promise in diabetic rodent models through both exogenous application (87-89) or gene therapy (84, 90, 91). VEGF supplementation has also demonstrated effectiveness in ischemic injuries, where it has increased granulation tissue formation up to 150% in ischemic wounds in non-diabetic rabbits (83), alleviated non-diabetic PVD ischemia in clinical trials (92) and non-diabetic rodent models of hind-limb ischemia (93), and improved neovascularization and tissue survival in ischemic skin flaps in rats (94).

1.5.2 Clinical Limitations of VEGF Therapy for Ischemic Diabetic Foot Ulcers

A significant barrier to effective VEGF therapy is the hyperactivity of proteolytic MMPs in the chronic wound environment (e.g. 65-fold higher levels of MMP1 in non-healing diabetic foot ulcers compared to acute traumatic wounds (68)), which causes rapid degradation of new granulation tissue and simultaneously degrades any exogenously applied VEGF. Therefore, protection of VEGF and granulation tissue from proteolytic activity is necessary and can be done by co-administration with MMP inhibitors, the use of ECM scaffolds as a competitive substrate, and/or engineering of more cleavage-resistant VEGF mimics.

Another critical limitation is the maintenance of VEGF in its therapeutic range, which is hindered by MMP-mediated degradation, its short half-life, and diffusion away from the site of application into systemic circulation (95, 96). Furthermore, the potential for excessive VEGF activation and systemic exposures raise concerns of uncontrolled angiogenesis forming hyperpermeable and tumor-like tortuous vasculature; this is a particular concern for applications in diabetic patients, who are susceptible to excessive angiogenesis in the eye (diabetic retinopathy) (97). These two interrelated problems illustrate the importance of controlling the degree of VEGF activation and targeting VEGF therapies to limit systemic exposures. Recently, researchers have improved therapeutic efficacy and prevented systemic exposure by modifying VEGF with ECM-binding components to target VEGF activity in both diabetic wound healing models and non-diabetic ischemic flap models (98-102).

Many growth factor therapies have shown measurable improvements in accelerating diabetic wound closure in rodents but have failed to demonstrate sufficient efficacy in clinical trials (103); currently, only PDGF (Becaplermin gel aka Regranex) has been FDA approved for neuropathic DFU and is not appropriate for ischemic DFU, while development of topical VEGF (Telbermin) for DFU was discontinued in 2008 during phase 2 clinical trials (103, 104). Failure in clinical translation of growth factor therapies such as VEGF can be attributed, at least in part, to failed maintenance in its therapeutic range due to growth factor degradation and diffusion away from its targeted site (105, 106). Furthermore, these isolated growth factor therapies are designed to address a singular defect and therefore do not account for multiple pathophysiological deficiencies within the wound. Pro-angiogenic VEGF therapies for ischemic DFU have shown encouraging success in rodent models but these current limitations contribute to its failed translation into the clinic.

1.6 *Our Approach to Improve VEGF Efficacy in the DFU Microenvironment*

Development of effective therapies that can correct multiple derangements while maintaining efficacy in the complex and highly proteolytic environment of the DFU has proven exceptionally challenging. Currently, only modest benefits have been achieved by emerging therapies targeting singular aspects of disease, and thus *Futrega et al.* argues that next-generation DFU therapies should aim to combining growth factor, ECM scaffold, and cell treatments to synergistically maximize repair potential in this complex environment (107). We thus focused on treating multiple aspects of disease with a tiered approach, building in complexity, to induce targeted and controlled angiogenesis through VEGF pathways, while bearing in mind important design parameters of targeting, controlling, and protecting VEGF activity. Targeting and control can be achieved by binding therapies to the wound bed and regulating VEGF release, while protecting VEGF activity was explored using two different mechanisms. First, collagen-targeted nanoparticles loaded with VEGF could protect VEGF and maintain therapeutic concentrations within the proteolytic wound environment, thereby prolonging treatment. Alternatively, degradation-resistant peptides that activate and potentiate VEGF pathways could also be used to prolong angiogenic activity. Furthermore, pro-angiogenic proteoglycans formed by the combination of these peptides and proteoglycan mimics have the added capacity to protect ECM from MMP degradation. Moreover, multiple bioactive peptides could be added to promote cell recruitment by direct integrin-binding or chemotactic mechanisms. We thereby start discussing a synthetic nanoparticle system to protect and deliver VEGF, and then propose two variants of pro-angiogenic decorin mimics that stimulate and potentiate VEGF angiogenesis, the last variant of which also promotes endothelial progenitor cell recruitment. Both variants simultaneously protecting existing ECM and/or exogenous ECM wound dressings from rapid degradation. Each proposed therapy could be administered alone or in conjunction with one another to exploit potentiation of VEGF. For example, a collagen scaffold-based delivery of a pro-angiogenic decorin mimic coupled with controlled release of VEGF from a nanoparticle system will allow potentiation of released VEGF, thereby reducing the necessary dose. We hypothesize that a biomimetic collagen-binding peptidoglycan functionalized with a pro-angiogenic peptide will protect the collagen matrix from rapid degradation, and also promote angiogenesis by potentiating endogenous and exogenous VEGF to accelerate ischemic cutaneous wound healing.

1.7 *SPECIFIC AIMS AND THESIS OVERVIEW: PROPOSED COLLAGEN-TARGETED PRO-ANGIOGENIC THERAPIES*

1.7.1 Aim 1. Develop a nanoparticle system for controlled release of VEGF

Our lab has developed thermosensitive nanoparticles to improve therapeutic efficacy of anti-inflammatory peptides, delivered both intracellularly and extracellularly for various applications ranging from decreasing intraarticular osteoarthritic inflammation (108-113) to reducing post-angioplasty intimal inflammatory damage (114, 115). In Chapter 2 of this thesis, we first discuss characterization and incremental improvements (greater therapeutic loading and prolonged release) to the previously developed solid non-degradable nanoparticle systems and then demonstrate proof-of-concept that these nanoparticle systems can be effectively adapted for extracellular delivery of full length growth factors such as VEGF by employing collagen matrix targeting. The future vision for this therapeutic encompasses fully degradable, hollow, thermosensitive nanoparticles conjugated with collagen-binding peptides for matrix targeting and a prolonged release profile.

1.7.2 Aim 2. Synthesize and characterize pro-angiogenic decorin mimics

Our lab has pioneered a mimetic of decorin, a proteoglycan predominantly found in skin, that binds specifically to collagen matrices and suppresses excess MMP-induced degradation of collagen in an incisional wound environment (116). The decorin mimetic (DS-SILY), composed of a dermatan sulfate (DS) backbone and a collagen-binding peptide (SILY), also decreases dermal scarring by modulating collagen organization (116). Building upon this engineered therapeutic technology, we propose to further functionalize our decorin mimetic with two conjugated pro-angiogenic peptides, VEGF-mimicking “QK” and αvβ3 integrin-binding “LXW7”, to stimulate angiogenesis through direct and indirect VEGF pathway activation, respectively. Pro-angiogenic decorin mimics were synthesized with improved bioconjugation chemistry with a degree of substitution of 4 collagen-binding peptides per dermatan sulfate backbone, but modified with varying degrees of substitution of either the VEGF-mimicking peptide “QK” or integrin-binding peptide “LXW7”. In Chapter 3, we discuss the synthetic chemistry and post-conjugation peptide quantification. We also characterize the secondary structure of pro-angiogenic peptides and matrix-binding capacity of pro-angiogenic decorin mimics, as well as explore biological effects of the EDC synthetic chemistry on dermatan sulfate and the decorin mimic DS-SILY through assessing endothelial cell (EC) proliferation and VEGFR2 activation.

1.7.3 Aim 3. Assess *in vitro* and *in vivo* angiogenesis of pro-angiogenic decorin mimics

In Chapter 4, we quantify *in vitro* and *in vivo* angiogenesis, with and without VEGF, for the two variants of pro-angiogenic decorin mimics by evaluating 1) EC proliferation and migration, 2) two-dimensional EC tubule formation on matrigel embedded with pro-angiogenic decorin mimics, 3) neovascularization from a chick chorioallantoic membrane (CAM assay) growing into a collagen scaffold embedded with pro-angiogenic decorin mimics, reflecting the ability of the scaffold to integrate into existing vasculature, and 4) EC monolayer permeability.

2. DEVELOPMENT OF A DEGRADABLE, THERMOSENSITIVE NANOPARTICLE SYSTEM FOR VEGF DELIVERY

2.1 *Preface*

The final pNIPAM nanoparticle drug delivery system that was tested for VEGF delivery was a collaborative effort with Dr. Scott Poh and Dr. James McMasters and was the product of incremental improvements, described over 3 published articles, outlining its efficacy in delivering an anti-inflammatory peptide in osteoarthritic applications (111-113). The beginning of this chapter therefore first addresses the osteoarthritis work to describe the improvements in the nanoparticle system. Our lab more recently demonstrated that pNIPAM nanoparticles could also deliver its payload extracellularly by implementing matrix-targeting through surface modification with a collagen-binding peptide (114, 115). After illustrating the development of our nanoparticle system through the aforementioned works, I describe the pilot experiments showing translation to VEGF delivery.

2.2 *Poly-N-isopropylacrylamide Nanoparticles for Drug Delivery*

Numerous polymeric nanoparticles have been used to protect bioactive molecules until release, ranging from naturally derived sources such as chitosan and alginate to synthetics such as poly(caprolactone), poly(lactic-co-glycolic acid) (PLGA) and poly(N-isopropylacrylamide) (pNIPAM). We have previously reported that peptide-loaded pNIPAm nanoparticles protect the peptide therapeutic from enzymatic degradation, thus increasing drug half-life in the presence of serum (109, 117). ‘Smart’ pH responsive or temperature sensitive polymers are particularly advantageous because they can facilitate sustained controlled release that can be triggered by a specific event. pNIPAM is one such stimuli-responsive polymer that undergoes a volume phase transition at a lower critical solution temperature (LCST) between 31°C and 33°C (118, 119), exhibiting a hydrophilic swollen state at low temperatures to a hydrophobic collapse at high temperature in an aqueous environment. Due to this thermosensitive property, pNIPAM can be passively loaded with water-soluble therapies in a cold expanded state and subsequently collapse and entrap diffusible agents at physiological temperatures resulting in drug release over a prolonged period of time (120). pNIPAM’s ease of drug loading, biocompatibility, and physiologically relevant LCST independent of concentration and molecular weight make it a highly attractive polymer for drug delivery, although co-polymerization of other monomers can shift the LCST. One of the primary drawbacks of pNIPAM for targeted drug delivery is that its narrow range of physical and chemical properties make it difficult to tune its intrinsic drug release kinetics or directly add targeting moieties to its surface after synthesis. However, doping the polymeric formulation with charged and/or chemically active co-monomers easily overcomes these limitations. For example, previous work from our lab has demonstrated that incorporating a modest 5 mol% of 2-acrylamido-2-methyl-1-propanesulfonic acid (AMPS), an anionic sulfated monomer, into pNIPAM nanoparticles increased loading of cationic peptides and improved colloidal stability (108, 109). Furthermore, co-polymerization with polyethyleneglycol (PEG) can decrease non-specific protein binding (121), and endolytic degradation can be instilled using the degradable crosslinker bis(acryloyl)cystamine (BAC) (113). Inclusion of acrylic acid imparts chemical functionality of carboxylic acids that can be further reacted for surface modifications (114, 115). Finally, the addition of fluorescent monomers such as fluorescein *o*-acrylate (113) or methacryloxyethyl thiocarbamoyl rhodamine B (122) facilitates intracellular visualization.

2.3 *Endolysosomal Intracellular Delivery of Anti-Inflammatory Peptides from PNIPAM Nanoparticles with Reducible Crosslinks Decreases Inflammation in Cartilage Explants*

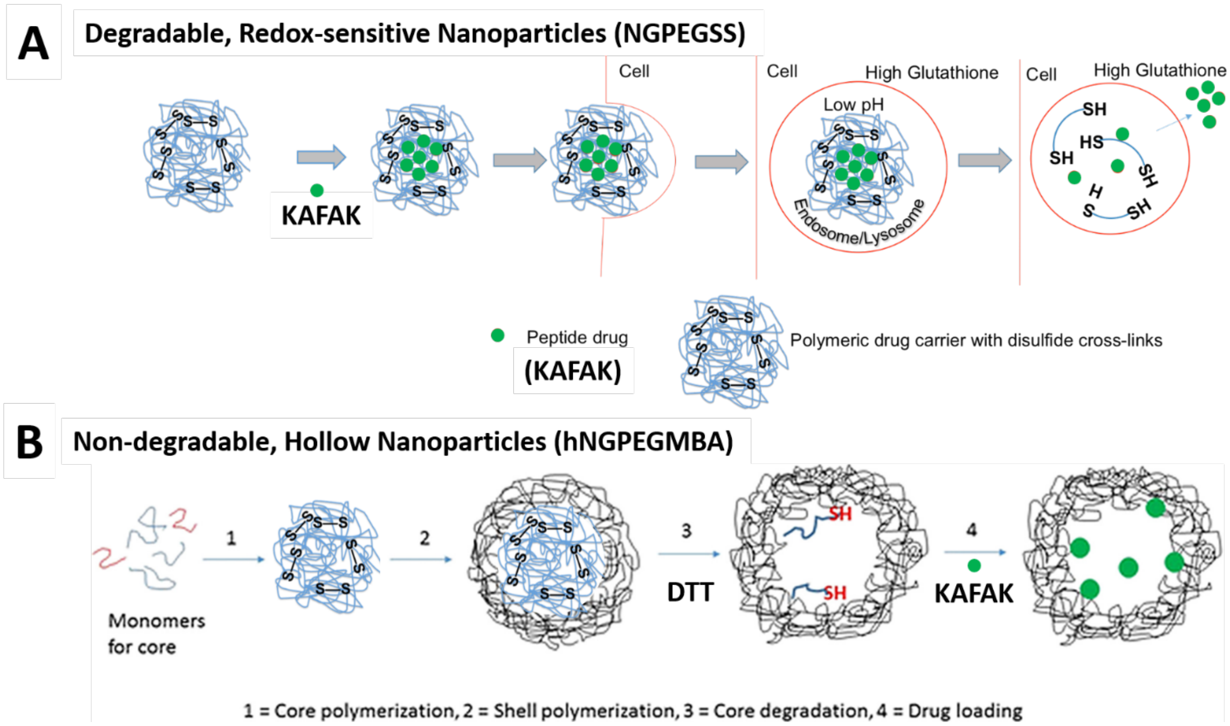

Figure 2-1. **pNIPAM Nanoparticle Schematic.**

(A) Degradable, redox-sensitive nanoparticles (NGPEGSS) were loaded with KAFAK and then taken up into the cellular endolysosomal compartment, where they degraded and released KAFAK. (B) Non-degradable, hollow nanoparticles (hNGPEGMBA) were developed from the nanoparticle platform shown in (A) by polymerizing a non-degradable shell around the reducible core, and then degrading and allowing the core to diffuse out by dialysis before KAFAK loading.

2.3.1 Introduction

Osteoarthritis, affecting ~27 million Americans (123, 124), is the leading cause of chronic disability in the United States (125). It is primarily characterized by a progressive cycle of chronic inflammation (126) and cartilage degradation, causing joint pain and stiffness. In response to sustained levels of pro-inflammatory cytokines, chondrocytes synthesize proteolytic enzymes that degrade extracellular matrix components (127, 128), including aggrecan (129), stimulating additional inflammation and facilitating penetration of inflammation and degradation factors into the cartilage. Osteoarthritis is treated with anti-inflammatory therapies that provide short-term relief and can have adverse side effects. Locally-delivered, degradable, controlled release, anti-inflammatory drug delivery systems could prolong relief and minimize side effects.

Brugnano et al. investigated an anti-inflammatory cell-penetrating peptide KAFAKLAARLYRKALARQLGVAA, (KAFAK), which inhibits MAPK-activated protein kinase 2 (MK2) (117). MK2 controls the synthesis of many pro-inflammatory cytokines, including IL-1, TNF-α, and IL-6 (128, 130-132). The MK2 pathway is triggered in osteoarthritis and promotes release of enzymes that degrade cartilage (128). KAFAK treatments are susceptible to peptidases in the blood and synovial fluid. To limit systemic exposure and premature degradation of KAFAK, our laboratory has designed poly*N*-isopropylacrylamide (pNIPAM) nanoparticle delivery systems to increase the peptide's therapeutic lifetime (108-110, 113, 133).

Bartlett et al. previously reported a thermosensitive non-degradable methylenebisacrylamide (MBA) cross-linked pNIPAM-AMPS nanoparticle system for delivering KAFAK in osteoarthritis applications (108). While *Bartlett et al.* also later reported high pH sensitive, hydrolytically degrading above pH 5.0, pNIPAM nanoparticles with N,O-dimethacryloylhydroxylamine (DMHA) crosslinks to deliver KAFAK to damaged cartilage, the nanoparticles continuously degraded before reaching the target cell, thus limiting the therapeutic potential of the system (110). Therefore, a nanoparticle that would not degrade until reaching the target cell could improve targeted KAFAK delivery. To this end, we incorporated reducible disulfide cross-links to the nanoparticle formulation using bis(acryloyl)cystamine (BAC, represented by SS in nanoparticle nomenclature), and also added PEG_{2000} diacrylate to render improved stability and 'stealth' properties and fluorescein *o*-acrylate for visualization. We thereby developed a thermo- and redox-sensitive nanoparticle platform (referred to as 'NGPEGSS') that degrades in the low-pH and reducing environment of endolysosomes after cellular uptake. When this reducible nanoparticle system was used to deliver KAFAK to RAW 264.7 macrophages, an approximately 6-fold greater KAFAK release and improved anti-inflammatory response was seen compared to non-degradable NGPEGMBA counterparts (113).

As a step toward developing an improved KAFAK delivery system for osteoarthritis, we investigated the ability of the NGPEGSS nanoparticles to selectively penetrate damaged cartilage. We also investigated the ability of NGPEGSS, which show enhanced extracellular stability and improved KAFAK retention and release, to effectively suppress inflammation via chondrocyte uptake in an *ex vivo* model of osteoarthritis.

2.3.2 Materials and Methods

2.3.2.1 Materials.

N-Isopropylacrylamide (≥ 98%, NIPAm) was acquired from Polysciences Inc. (Warrington, PA, USA). Dialysis membrane tubing was purchased from Spectrum Laboratories (Dominguez, CA). (1H-benzotriazole-1-yl)-1,1,3,3-tetramethyluronium hexafluorophosphate (≥ 98%, HBTU), N-hydroxybenzotriazole (> 97%, HOBT), N,N'-methylenebisacrylamide (99%, MBA), sodium dodecyl sulfate (SDS; 10% w/v in water), 2- acrylamido-2-methyl-1-propanesulfonic acid (99%, AMPSA), dithiothreitol (98%, DTT), fluorescein o-acrylate (98%, F), N,N-Diisopropylethylamine (99%, DIPEA), potassium persulfate (99%, $K_2S_2O_8$), N,N'-bis(acryloyl)cystamine (98%, BAC), and dimethyl sulfoxide (DMSO) were acquired from Sigma-Aldrich (St. Louis, MO, USA). NIPAm, MBA, and AMPS were stored under nitrogen at 4 °C. All water used in synthesis, dialysis, and testing was treated by a Milli-Q system (Millipore, Billerica, MA, USA; 18.2 MΩ•cm resistivity). Acrylate-PEG2000 was purchased from Laysan Bio (AL).

2.3.2.2 Peptide Synthesis and Purification

Therapeutic peptide KAFAK was synthesized on knorr resin by standard 9-fluorenylmethyloxycarbonyl (Fmoc) solid phase methodology(113). Knorr amine resin was swollen with dichloromethane (DCM) followed by dimethylformamide (DMF). A solution of 25% piperidine in DMF was added to the resin, bubbling under nitrogen for 15 min, and then washed with DMF (3x) and isopropyl alcohol (i-PrOH, 3x). For amino acid coupling, a solution of Fmoc-amino acid (3 equiv), (1H-benzotriazole-1-yl)-1,1,3,3-tetramethyluronium hexafluorophosphate (HBTU, 3 equiv), N-hydroxybenzotriazole (HOBT, 3 equiv) and N,N-Diisopropylethylamine (DIPEA, 5 equiv) in DMF was added to the resin bubbling under nitrogen for 2 h, and then washed with DMF (3x), DCM (3x) and i-PrOH (3x). To deprotect Fmoc, 25% piperidine in DMF was added to the resin, and nitrogen was bubbled for 20 min. The solvent was then removed and the resin washed with DMF (3x) and i-PrOH (3x). The above sequence was repeated for coupling and deprotection of each amino acid. The final compound was cleaved from the resin with a cocktail of trifluoroacetic acid (Sigma-Aldrich, St. Louis, MO, U.S.A.), triisopropyl silane (TCI America, Boston, MA, U.S.A.), ethane dithiol (Alfa Asara, Ward Hill, Massachusetts, U.S.A.), and Milli-Q water. The cleaved mixture was concentrated under vacuum and then immediately precipitated in diethyl ether, recovered by centrifugation, solubilized in Milli-Q water, and lyophilized (Supporting Scheme 1). Peptides were purified on an FPLC AKTA Explorer (GE Healthcare, Pittsburgh, PA, U.S.A.) with a 22/250 C18 prep-scale column (Grace Davidson, Deerfield, Illinois, U.S.A.) and an acetonitrile gradient with 0.1% trifluoroacetic acid. Purity of peptides were determined by HPLC to be > 98%. Peptide molecular weight was confirmed by matrix-assisted laser desorption ionization time-of-flight (MALDI TOF) mass spectrometry with a 4800 Plus MALDI TOF/TOF Analyzer (Applied Biosystems, Foster City, CA, U.S.A)(Supplemental Figure S1).

2.3.2.3 PNIPAM-AMPS Nanoparticle Synthesis

2.3.2.3.1 Solid Nanoparticles

Solid NIPAM-AMPS nanoparticles were synthesized similar to previous protocols. Briefly, the nanoparticle compositions were formed by dissolving 192.1 mg NIPAM and 5 mol% AMPS in 18 mL degassed MilliQ water in a three-neck round bottom flask. 3 mol% PEG-acrylate and 2 mol% cross-linker (MBA, DMHA, or BAC) was pre-dissolved in 3% (v/v) of dimethyl sulfoxide (DMSO) in water for 10 mins before addition to polymer mixture. 41 μL of a 10% (v/v) SDS in MilliQ water solution was added, and the mixture was heated to 65°C under nitrogen. Potassium persulfate (8.4mg) was dissolved in 2 mL degassed MilliQ water and added after a 35 mins equilibration to initiate polymerization. After 5 h, the reaction was removed from heat and allowed to cool to room temperature. Particles were dialyzed against MilliQ water for 5 days using a 15,000 MWCO membrane.

For fluorescent nanoparticle synthesis, 1 mol% fluorescein o-acrylate (F) was pre-dissolved in 3% DMSO solution. The dye-DMSO solution was added to the polymer mixture and equilibrated for 30 mins. Potassium persulfate dissolved in 2 mL degassed MilliQ water was added to initiate polymerization. Particles were dialyzed against MilliQ water for 5 days using a 15,000 MWCO membrane. All sample were freeze-dried and kept in the dark for further experiments.

2.3.2.3.2 Hollow Nanoparticles

We further used this degradable system to develop hollow nanoparticles by polymerizing a non-degradable MBA cross-linked shell around a reducible disulfide cross-linked nanoparticle core. For core synthesis, 49 mL of Milli-Q water was heated to 70ºC in a 3-neck round bottom flask and refluxed under nitrogen for 30 minutes. 178 mg of NIPAm, 6 mol% BAC, and 20 mg of SDS were dissolved in 10 mL of degassed Milli-Q water and added to the flask. Finally, 35 mg of potassium persulfate was dissolved in 1 mL of Milli-Q water and added to the flask to initiate the reaction. The polymerization was carried out for 5 h under nitrogen. The resultant particles were filtered through a Whatman filter to remove any aggregates, and then cleaned several times by centrifugation and resuspension in Milli-Q water.

To create the non-degradable pNIPAM shell, 4 mg of SDS was added to 5 mL of the disulfide crosslinked cores in a 3-neck round bottom flask and heated to 70°C under nitrogen. A separate solution of 50 mg NIPAm, 5 mol% AMPSA, 2 mol% MBA and, for PEGylated nanoparticles, 3 mol % Acrylate-PEG2000 were prepared in 30 mL of degassed Milli-Q water and allowed to incubate to room temperature under nitrogen for 45 minutes before being added to the heated core solution. To initiate polymerization, 6 mg of potassium persulfate was dissolved in 1 mL Milli-Q water and added to the flask. After 5 hours, the core-shell nanoparticles were collected and dialyzed against Milli-Q water for 6 days using a 15 kDa MWCO dialysis membrane (Spectra-Por).

Following dialysis, the core was degraded by re-suspending the core-shell particles in a 1 mM DTT solution and allowing the solution to react under stirring for 7 days. The hollow particles were then cleaned by centrifugation and resuspension in Milli-Q water, frozen, and lyophilized. For fluorescent nanoparticle synthesis, 1 mol% fluorescein o-acrylate was pre-dissolved in 3% DMSO and then added to the shell polymer mixture and allowed to equilibrate for 30 minutes before reaction initiation with the addition of potassium persulfate.

2.3.2.4 Nanoparticle Characterization

Size measurements were performed using dynamic light scattering (DLS) on a Nano-ZS90 Zetasizer (Malvern, Westborough, MA, USA). Zeta (ζ) potentials were measured at 25 °C using a Nano-ZS90 Zetasizer in capillary cells in PBS. To characterize their degradation, samples with an identical particle concentration were prepared in pH 7.4 PBS buffer. To one solution, an excess of DTT (1 mM) was added and allowed to incubate for 24 h.

2.3.2.5 Nanoparticle Drug Loading and Release

Purified peptide was first dissolved in ultrapure water to create a 5 mg/mL loading solution, and then this solution was added to 5 mg of lyophilized nanoparticles and allowed to incubate for 24 h at 4°C in the swollen state. After incubation, 9 mL of water was added and particles underwent 1 h of centrifugation at 35,000 rpm and 37°C in an Optima L-90k Ultracentrifuge (Beckman Coulter, Indianapolis, IN, USA). The nanoparticle pellet was briefly re-suspended in 2 mL water and lyophilized. To collect peptide release profiles, KAFAK-loaded nanoparticles were suspended in sterile PBS (Invitrogen, Grand Island, NY, USA) with or without DTT over a 96 h period. Measurement of free peptide released into the solution and the amount of peptide loaded were determined using fluorescence analysis with a fluoraldehyde ophthalaldehyde (OPA) solution (Thermo Scientific, Waltham MA, USA) according to the manufacturer’s protocol. For KAFAK release studies, fluorescent measurements of drug release were taken every 15 min for the first hour and then at 1, 6, 12, and 24 h every day afterward for 4 days.

2.3.2.6 Chondrocyte Isolation and Culture

Primary chondrocytes were harvested from the load-bearing region of femoral condyles from 3-month-old calves within 24 h of slaughter (Dutch Valley Veal, South Holland, IL, USA) as described previously(110, 134, 135). Cells between passage 1 and 4 were seeded with 10,000 cells/well in 8-well Lab-Tek chamber slides for experiments.

2.3.2.7 Nanoparticle Uptake in Chondrocytes

To determine intracellular nanoparticle uptake, chondrocytes were incubated with 1.5 mg/mL fluorescein-labeled nanoparticles for 4 h or 24 h at 37°C in culture medium. All samples were performed in triplicate. After washing with medium to remove any unbound nanoparticles, the cells were imaged using confocal microscopy (Olympus FV1000). To analyze co-localization of nanoparticles in endosomal/lysosomal compartments, Lysotracker DND-99 (Life Technologies, Grand Island, NY, USA) staining was added according to the manufacturer’s protocol. Semi-quantitative fluorescence measurements of confocal images were used to compare uptake between degradable and non-degradable nanoparticles. Image analysis by ImageJ determined the number of fluorescent pixels (area) and the integrated fluorescence intensity for the green channel normalized to the red channel within each field of view (n = 3). Overlapping green and red fluorescence indicated co-localization of green nanoparticles inside red endolysosomes.

Cell samples were subjected to the trypan blue dye exclusion to evaluate cell viability, and CellTiter 96 AQueous One Proliferation Assays (Promega, Madison, WI, USA) were performed on chondrocytes according to the manufacturer's protocol to quantify nanoparticle cytotoxicity.

2.3.2.8 *Ex vivo* Osteoarthritis Model

Cartilage plugs (3mm diameter isolated as described above) were washed three times in serum-free medium and equilibrated for 3 days in 5% FBS supplemented media. Osteoarthritis conditions were simulated by removal of native aggrecan and then inducing inflammation using a previously described protocol (135). After culturing for 2 days, nanoparticle treatments were added. Fresh IL-1β and nanoparticles were added every 2 days for an 8-day culture period. Media aliquots were collected and stored in low bind tubes at -80°C until further analysis.

2.3.2.9 Analysis of *ex vivo* IL-6 Secretion

IL-6 cytokine production from cartilage plugs was determined with a bovine IL-6 ELISA development kit (PIESS0029, Thermo Scientific, Rockford, IL, USA) according to the manufacturer's protocol. IL-6 production was normalized to individual plug weight and to the negative control where healthy plugs with intact aggrecan were IL-1β stimulated.

2.3.2.10 Cartilage Penetration by Nanoparticles

Bovine cartilage plugs were either trypsin treated to simulate osteoarthritis-like conditions or left in cell culture media to maintain healthy tissue-like environment. Non-fluorescent nanoparticles (as control) and fluorescent nanoparticles were re-suspended at 0.5 mg/mL in PBS and added to cartilage plugs for 24 h. After treatment, plugs were washed 3 times with PBS and incubated at 37°C for 30 mins to remove any unbound nanoparticles. A mid-sagittal cut (30 µm thickness) was made through the plug using a cryotome. Sections were imaged by confocal microscopy at 488 nm excitation (Olympus FV1000) to examine the depth of fluorescent nanoparticle penetration into the plugs from the articular surface. Fluorescent intensity was quantified using ImageJ, and the intensity in three independent areas near the articular surface of each image was measured with values represented as average intensity ± SEM.

2.3.2.11 Statistical Analysis

Student's t-tests were used to determine statistical significance between treatment groups ($\alpha = 0.05$). Data is expressed as mean values ± standard deviation unless otherwise noted.

2.3.3 Results

2.3.3.1 Nanoparticle Characterization

Previous work from our laboratory showed that 5% AMPS co-monomer in pNIPAM nanoparticles resulted in maximum KAFAK loading capacity (108). Incorporating 5% AMPS into disulfide PEGylated (NGPEGSS) nanoparticles yielded loading efficiency of 34.6%, which was statistically equivalent to non-degradable PEGylated nanoparticles (NGPEGMBA) at 36.7% and high-pH degradable NGPEGDMHA nanoparticles at 34.7% (Table 2-1). In contrast, hollow non-degradable nanoparticles exhibited a significantly increased loading efficiency of 49.8%. All nanoparticles also possess a negative ζ potential as expected due to the incorporation of the sulfated AMPS, although the range of ζ potentials did not vary much among the different nanoparticle formulations. Therefore, changing cross-link type does not have a profound impact on ζ potential for particles when using 2 mol% cross-linker content as shown in Table 2-1.

Table 2-1. **Size, ζ Potential, and Drug Loading**

Size measurements reported here were determined by DLS at ambient temperature in PBS at 25°C and 37°C. Percent drug loading is defined as the mass of KAFAK encapsulated within a given mass of nanoparticles. Zeta potential measurements are provided for nanoparticles in ultrapure water and PBS at room temperature to reflect nanoparticle properties during drug loading and in physiologically relevant solutions, respectively.

Nanoparticle	Size$_{25^\circ C}$ (nm) ± stdev	Size$_{37^\circ C}$ (nm) ± stdev	Drug loading (%) ± stdev	Zeta potential$_{H_2O}$ (mV) ± stdev	Zeta potential$_{PBS}$ (mV) ± stdev
NGPEGMBA	246 ± 8.9	235 ± 1.5	36.7 ± 4.3	-11.3 ± 1.34	-4.28 ± 1.56
NGPEGDMHA	237 ± 8.2	213 ± 1.8	34.7 ± 7.2	-19.1 ± 1.91	-6.05 ± 1.91
NGPEGSS	223 ± 9.7	207 ± 5.0	34.6 ± 3.7	-19.9 ± 2.16	-3.81 ± 2.01
hNGPEGMBA	311 ± 9.3	192 ± 13.3	49.8 ± 8.7	No data	-8.48 ± 3.50

DLS size measurements over a 20°C to 50°C temperature sweep demonstrated that the ability of pNIPAM-AMPS nanoparticles to collapse in response to increasing temperature was maintained with the incorporation of PEG and disulfide cross-links (Table 2-1 and Figure 2-2A). We found that while AMPS addition shifted the LCST to a higher temperature of ~38°C (Figure 2-2A) compared to pure pNIPAM, addition of PEG to the bulk nanoparticle formulation did not affect the LCST (data not shown). The LCST shift with AMPS addition is supported by *Bartlett et al.*'s observation that increasing AMPS content caused a corresponding shift in LCST to higher temperatures (108). LCSTs of nanoparticles with disulfide versus MBA crosslinks are similar, indicating that the change in crosslink type did not significantly affect LCST. Figure 2-2D also shows that hollow non-degradable nanoparticles (hNGPEGMBA) were significantly larger in the expanded state, as expected due to polymerization around a similarly sized core, but also collapsed more at high temperatures than solid non-degradable counterparts. The hNGPEGMBA nanoparticles displayed a ~38% decrease in size from 25°C to 37°C compared to ~4.5% decrease for their solid NGPEGMBA counterparts.

Figure 2-2B demonstrates a progressive decline in NGPEGSS nanoparticle size over time (~30% decrease in diameter) indicating slow nanoparticle degradation over 48 hours when exposed to reducing conditions, whereas NGPEGMBA and NGPEGDMHA did not exhibit a drastic change in size (~4% decrease). Non-degradable nanoparticles did not significantly change in size or drug release over time in either pH 7.4 or pH 4.0 environments (Figure 2-2 B & C), while degradable disulfide cross-linked nanoparticles (NGSS and NGPEGSS) decreased in size corresponding to a significant increase in drug release after addition of DTT (Figure 2-2 B & C) and similar results were also seen at pH 4.0 (113). Figure 2-2B also shows that NGPEGDMHA nanoparticles degraded readily at physiological pH of 7.4 over time.

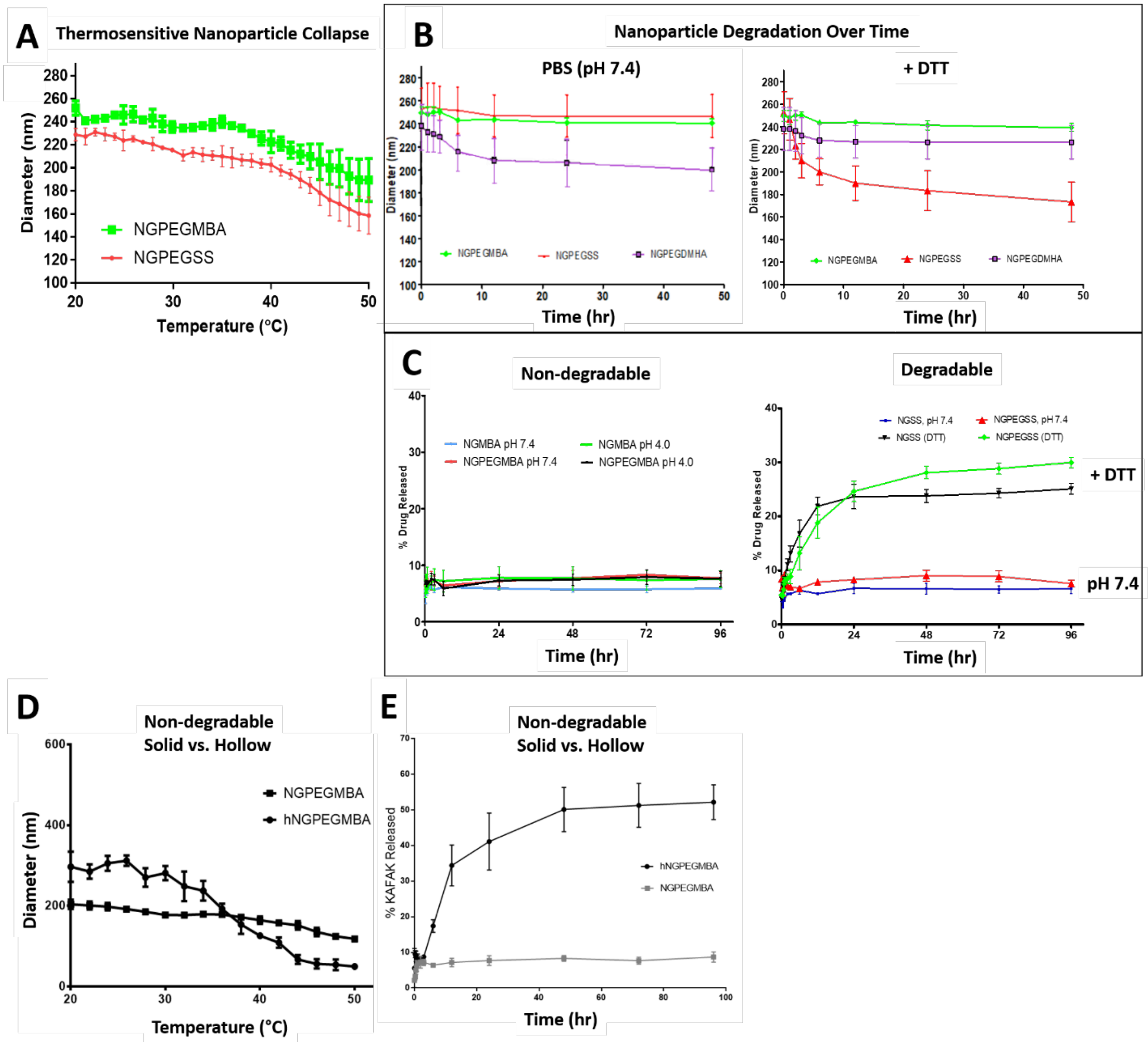

Figure 2-2. **Nanoparticle Characterization by Size and Drug Release.**

DLS size measurements are shown as a function of temperature (A & D) and as a function of time in PBS and upon addition of DTT (B & C). Hollow non-degradable nanoparticles (hNGPEGMBA) were significantly larger in the expanded state and collapsed more at high temperatures than solid non-degradable counterparts (D). Non-degradable nanoparticles do not have a significant change in size or drug release over time in either pH 7.4 or pH 4.0 environments, while degradable disulfide cross-linked nanoparticles (NGSS and NGPEGSS) demonstrate a significant decrease in size corresponding to a significant increase in drug release after addition of DTT (B & C). Hollow non-degradable nanoparticles exhibited the greatest drug release over time (E), exhibiting an improvement over solid degradable nanoparticles in a reducing environment. Sample size n = 3 for all nanoparticle measurements.

2.3.3.2 Chondrocyte Nanoparticle Uptake and Cytotoxicity

Confocal microscopy confirmed the uptake of both fluorescent degradable NGPEGSSF and non-degradable NGPEGMBAF nanoparticles into primary chondrocytes after 24 h incubation but not after 4 h incubation (Figure 2-3). Figure 2-3 also demonstrates co-localization of green fluorescent nanoparticles with red endolysosomal compartments for both MBA and BAC crosslinked nanoparticles. Semi-quantitative green/red fluorescence ratio analysis in Figure 2-4, where green/red pixel area ratio of 1.0 represents 100% co-localization of particles with endolysosomes, suggests that green/red pixel area is statistically similar between the two types of nanoparticles. However, the green/red integrated intensity ratio is significantly greater for the NGPEGSS as compared to the NGPEGMBA nanoparticles suggesting that the total number of nanoparticles taken up into these intracellular compartments is higher for NGPEGSS than NGPEGMBA. The CellTiter assay showed no significant cytotoxicity after incubation for 48 h with NGPEGSS, NGPEGMA, or free KAFAK peptide (Figure 2-5).

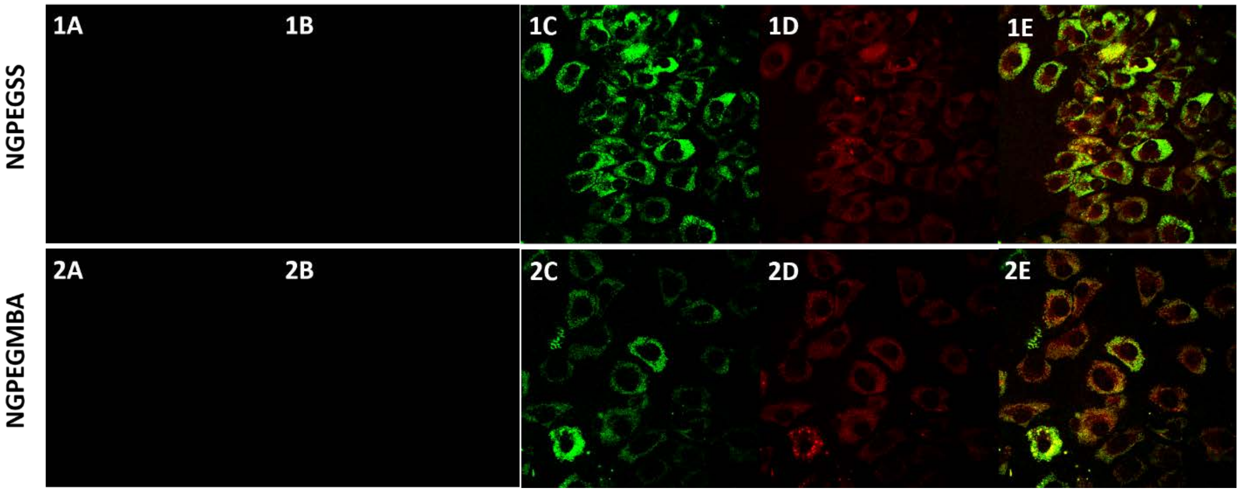

Figure 2-3. **Confocal microscopy of primary bovine chondrocytes incubated at 37°C with (1) NGPEGMBA and (2) NGPEGSS.**

(A) non-fluorescent nanoparticles as negative controls; (B&C) fluorescent nanoparticles after (B) 4 h and (C) 24 h incubation; (D) Lysotracker DND-99; (E) green nanoparticle overlay on red endolysosomes.

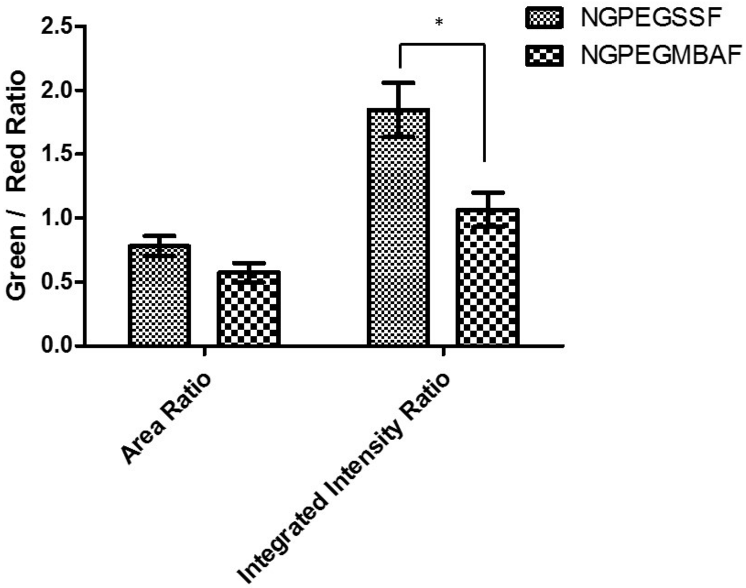

Figure 2-4. **Semi-quantitative fluorescence analysis of green nanoparticles and red lysotracker-labeled endolysosomes co-localization ratios by pixel area (left) and total integrated intensities (right).**

Bars represent averages ± sample standard deviations for 3 images for each condition. The area is the number of pixels above a threshold background value in the green and red fluorescent channels. There is no statistical significance in the area ratio differences. * denotes statistical significance ($p < 0.05$) between NGPEGSSF and NGPEGMBAF in integrated intensity ratio.

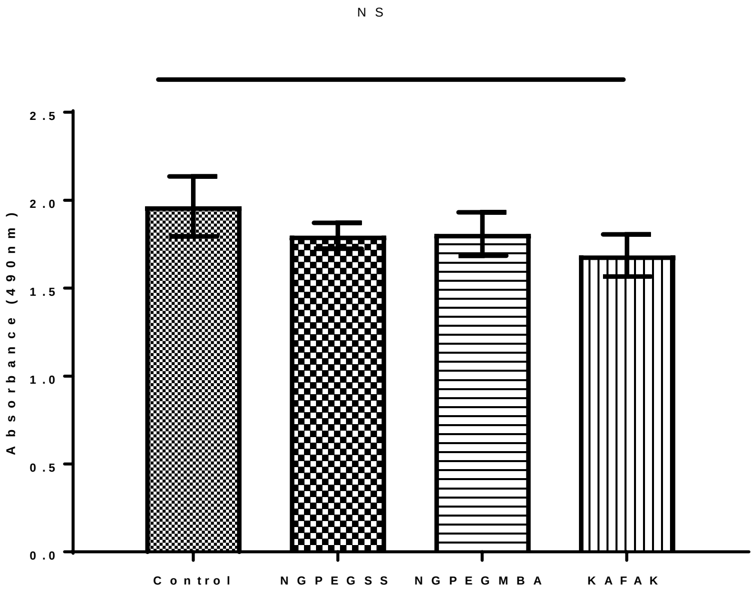

Figure 2-5. **CellTiter absorbance of chondrocytes treated with NGPEGSS, NGPEGMBA, and KAFAK compared to untreated control over a 48 h period at 37 °C. Sample size n = 3. NS = not significant.**

2.3.3.3 Cartilage Penetration by Nanoparticles

Incubation of cartilage explants for 24 h with FITC-labeled nanoparticles revealed greater penetration of nanoparticles throughout inflamed, aggrecan-depleted cartilage plugs compared to their healthy counterparts (Figures 2-6).

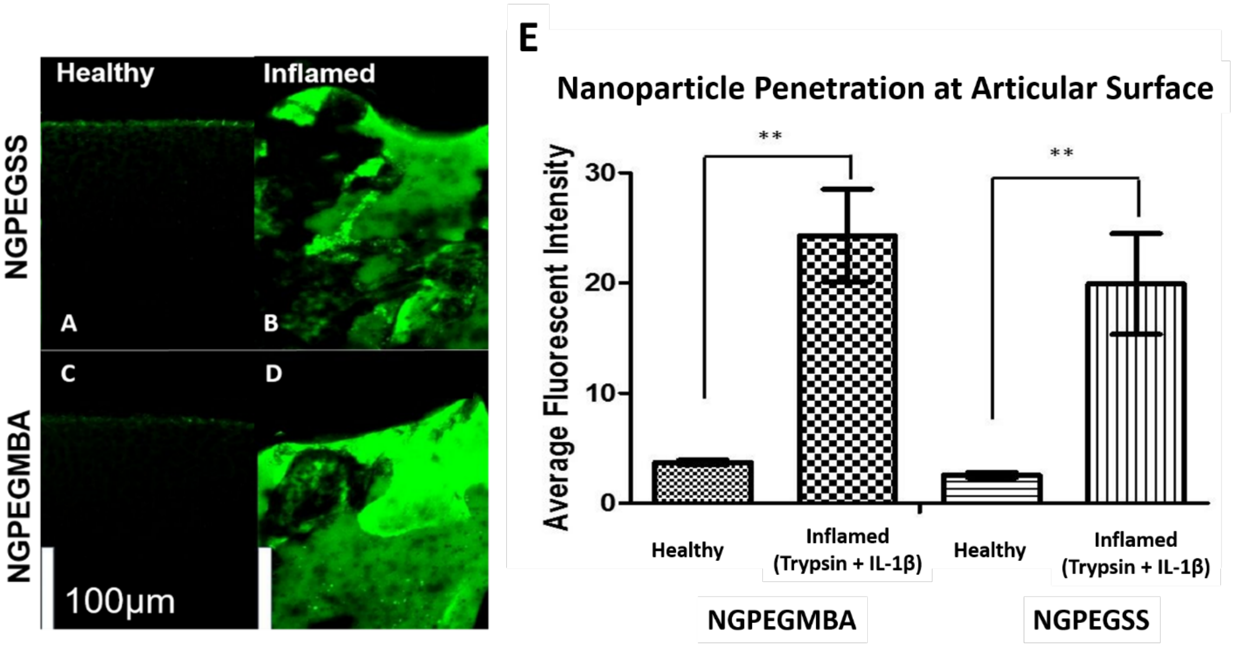

Figure 2-6. **Mid-sagittal cross-sections of bovine knee explants from the load-bearing region of the femoral condyles.**

The interface represents the articular surface after 24 h incubation with FITC-labeled nanoparticles; (Top) NGPEGSSF and (Bottom) NGPEGMBAF. Left panel represents normal healthy cartilage incubated with fluorescent (A) NGPEGSSF or (C) NGPEGMBAF showing minimal diffusion of fluorescent particles. Right panel represents (B) NGPEGSSF and (D) NGPEGMBAF diffusing through the inflamed, aggrecan-depleted *ex vivo* cartilage explants. Scale bar represents 100 µm. (E) Average intensity analysis of the articular surface incubated with fluorescent nanoparticles. Significantly higher fluorescence is observed in inflamed, aggrecan-depleted cartilage (Trypsin + IL-1β) demonstrating greater penetration of nanoparticles. Significance denoted as ** with $p < 0.01$. Bars represent intensity averages ± SEM of 3 independent areas at the articular surface.

2.3.3.4 IL-6 Expression in Cartilage Explants Treated with KAFAK-loaded Nanoparticles

Inflamed, aggrecan-depleted cartilage explants treated with either KAFAK-loaded NGPEGSS or KAFAK-loaded solid or hollow NGPEGMBA exhibited significant suppression of IL-6 secretion on days 4, 6, and 8 (Figure 2-7 E, G, & I). Furthermore, NGPEGSS decreased IL-6 production by a greater degree compared to NGPEGMBA on days 6 and 8. In comparison to solid non-degradable nanoparticles, KAFAK-loaded hollow non-degradable hNGPEGMBA also provided greater IL-6 suppression continuing through day 8 (Figure 2-7 I). These anti-inflammatory effects can be ascribed to KAFAK released from the nanoparticles, as the empty nanoparticles do not suppress IL-6 secretion (Figure 2-7 D, F, & H). As demonstrated by Figure 2-7C, free KAFAK treatment was not effective in inflammatory suppression presumably due to rapid degradation by peptidases present in serum-supplemented media.

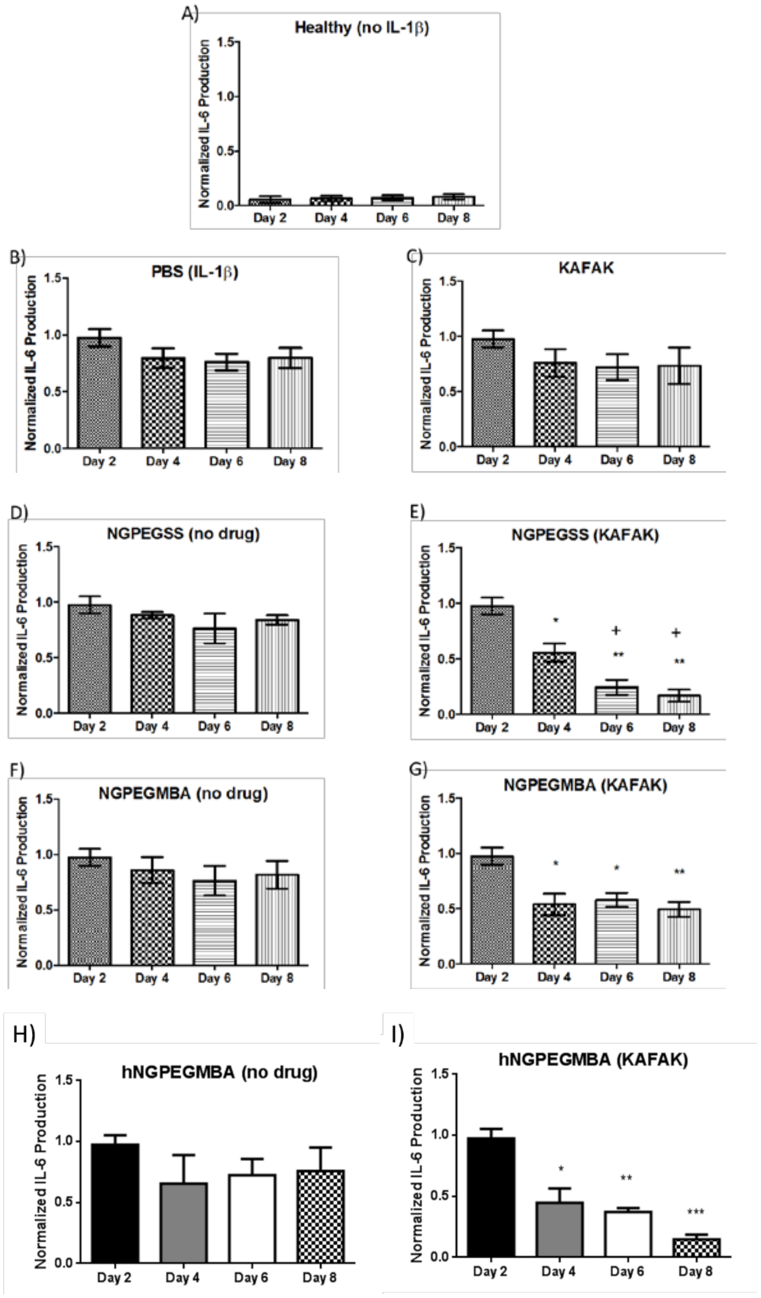

Figure 2-7. **Normalized IL-6 production by IL-1β inflamed, aggrecan-depleted cartilage plugs dosed with nanoparticles loaded with and without KAFAK.**

Treatments were added on day 2 after IL-1β stimulation. (A) Negative control, healthy cartilage without IL-1β stimulation. (B-E) Aggrecan-depleted plugs dosed with IL-1β and treated with (B) PBS, (C) free KAFAK, (D) empty NGPEGSS, (E) KAFAK-loaded NGPEGSS, (F) empty NGPEGMBA, (G) KAFAK-loaded NGPEGMBA nanoparticles, (H) empty hNGPEGMBA, (I) KAFAK-loaded hNGPEGMBA. Plots are normalized to individual plug weight and IL-6 production from the control and represent average ± SEM (n = 3). * denotes $p < 0.05$ and ** $p < 0.01$ with respect to the IL-1β positive control (plot B). + denotes a significant difference ($p < 0.05$) in IL-6 production between KAFAK-loaded NGPEGSS and NGPEGMBA nanoparticles on days 6 and 8.

2.3.4 Discussion & Conclusions

To develop a clinically relevant nanoparticle therapy for intra-articular injection to treat osteoarthritis, it is imperative that the nanoparticles do not aggregate in aqueous solutions and effectively deliver their payload to the target cells. With respect to nanoparticle stability, negative surface charge (ζ potential) can prevent aggregation and was achieved in all nanoparticle formulations explored here through the addition of 5% AMPS. As described previously, in aqueous solutions pNIPAM nanoparticles with 5% AMPS co-monomer remain spherical, well dispersed, and capable of delivering therapeutic peptides (109, 113). KAFAK-loaded pNIPAM nanoparticles with N,O-dimethacryloyl hydroxylamine (DMHA) crosslinks were reported to impart anti-inflammatory activity in cartilage explants and to penetrate deeply into aggrecan-depleted cartilage (110). However, the extracellular instability of the DMHA-crosslinked nanoparticles resulted in rapid release of KAFAK and may not efficiently protect the KAFAK from extracellular proteases. In contrast NGPEGSS nanoparticles were stable and released less than 10% of the loaded KAFAK over 96 h at pH 7.4, but released up to ~30% of loaded KAFAK within the same 96 h period in a reducing environment (shown by both DTT and pH 4.0 degradation studies) where the particles exhibited a significant decrease in size (113). In this study, we demonstrated that NGPEGSS nanoparticles were more effective at delivering KAFAK and produced an enhanced anti-inflammatory response in cartilage explants compared to non-degradable particles with prolonged efficacy lasting up to 8 days in response to bolus nanoparticle treatments every 2 days (Figure 2-7). Although we did not directly compare anti-inflammatory efficacy of KAFAK-loaded NGPEGSS to NGPEGDMHA in this study, it is likely that limiting extracellular KAFAK release would improve payload delivery by protecting KAFAK from proteases within synovial fluid.

Investigation of peptide loading into hollow non-degradable nanoparticles demonstrated loading efficiencies of ~49%, significantly higher than those found in their solid non-degradable counterparts which remained ~35%. In this follow-up study developing hollow non-degradable nanoparticles, we found that the new larger, more collapsible, and less dense system was able to achieve both higher loading and greater release than the aforementioned reducible NGPEGSS, and also provided extended IL-6 inflammatory suppression in the *ex vivo* cartilage explants. The main drawback was that the non-degradable hollow nanoparticles still only achieved maximum release of up to ~50% of the initially loaded peptide. We note that even in the degradable solid

NGPEGSS system, only ~30% of loaded peptide was freed from the particles and thus some amount may always be physically associated with the particle. Future nanoparticle formulations thus focus on creating hollow nanoparticle platforms that could additionally incorporate a triggered degradation after administration in hopes of maximizing peptide release.

Previous studies exploring efficacy of the NGPEGSS nanoparticle system for treatment of osteoarthritis confirmed uptake into macrophages (113), but did not investigate cartilage penetration nor uptake into chondrocytes. In studies presented here, as expected based on chondrocyte uptake of other nanoparticle carriers (chitosan (136), iron oxide (137, 138), and PLGA (139)) ranging from 50 nm to 300 nm, we observed nanoparticle uptake into endolysosomal compartments within chondrocytes (Figures 2-1 & 2-2). Additionally, we observed reduced chondrocyte expression of inflammatory cytokines upon uptake of KAFAK-loaded nanoparticles. Importantly for treatment of osteoarthritis, these nanoparticles reduce pro-inflammatory cytokine expression in macrophages (113) as well as chondrocytes. This suggests that our sulfated pNIPAM nanoparticle system penetrates inflamed cartilage and then gets taken up by both macrophages, which have evolved to endocytose foreign objects, and the chondrocytes present within the cartilage. Therefore this delivery system shows significant promise for treatment of articular cartilage via intraarticular injection.

While the disulfide crosslinked nanoparticles exhibit the majority of their KAFAK release within 48 h of encountering a degradation stimulus, they remain stable and release less than 10% of the loaded peptide prior to entering endolysosome environments (113). Further, they significantly prolonged suppression of the secretion of IL-6 by inflamed, aggrecan-depleted cartilage. Similarly, hollow non-degradable nanoparticles also exhibit the majority of their KAFAK release within 48 h; however this release begins as soon as the nanoparticles are administered. The benefit of the hollow non-degradable nanoparticles is mainly due to their increased loading and total release. Although we only demonstrated the ability of solid nanoparticles to be taken up into chondrocytes, we expect that the hollow nanoparticles discussed here would also have a similar property since the increased particle size is still within the range of reported particles taken up by chondrocytes in literature. The ability of our reported nanoparticles to diffuse into damaged cartilage, get taken up by chondrocytes and macrophages, and maintain the majority of their payload prior to cell uptake (for NGPEGSS) may make these systems ideal for treatment of osteoarthritis.

2.3.5 Towards a VEGF-delivery system

The main takeaways from this work towards an effective VEGF-delivery system was the method for adding redox-sensitive, low pH-triggered degradation in addition to our previously developed high pH (> 5.0) degrading DMHA cross-linked platform, and the implications for pH-triggered VEGF release in the wound environment. Although investigations of the role of pH in wound healing has been largely neglected and poorly understood in recent literature, pH has a key regulatory role in metabolic activity within a healing wound (140). While skin pH between 4-6 is known to be an indicator of healthy skin barrier function (141), chronic wounds are characterized by a significantly alkaline environment (142, 143). *Schneider et al.*'s review on the influence of pH on wound healing concludes that targeted titration of the wound pH back to an acidic milieu restores self-healing properties through inhibition of bacterial growth and promotion of fibroblast proliferation and re-epithelialization. Furthermore, physiological acidosis also significantly inhibits MMP activities, as optimal pH for these proteases has been reported ~pH 8.0 (140). Therefore, acidifying the wound environment at the time of nanoparticle application would be beneficial on multiple counts, in addition to triggering VEGF release from disulfide crosslinked nanoparticles. Alternatively, using previously developed DMHA cross-links could allow rapid VEGF delivery within the alkaline chronic wound environment. Another promising method of promoting nanoparticle degradation in the wound environment would be the use of MMP-degradable peptide-based cross-linkers.

The described reducible nanoparticles could be passively loaded with VEGF at cold temperatures and exhibit minimal release at physiological temperatures until reaching low-pH or reducing environments. We further demonstrated nanoparticle colloidal stability with the tested formulation and that its size at ~207 nm at physiological temperatures results in nanoparticle uptake by non-phagocytic cells such as chondrocytes. This finding highlighted the importance of extracellular tethering for small nanoparticles to ensure extracellular payload release. To this end, *McMasters et al.*'s surface addition of a collagen-targeting peptide tethering pNIPAM nanoparticles to secreted collagen outlines a method of preventing cellular uptake (115).

2.4 *Pilot Studies for VEGF Loading and Release from Hollow Thermosensitive Nanoparticles*

2.4.1 Materials and Methods

2.4.1.1 Materials

VEGF-165 (carrier-free) and VEGF ELISA duoset was purchased from R&D systems. All other materials for nanoparticle synthesis were the same as those reported in previous sections.

2.4.1.2 Hollow Nanoparticle Synthesis

Hollow nanoparticles were synthesized with slight modifications to previously reported methods (112). Uncrosslinked cores, held together by hydrophobic interactions, were first formulated. Shells, including 1 mol% acrylic acid and 50% increased potassium persulfate initiator but without PEG_{2000} diacrylate, were then polymerized around them as previously reported. The core-shell construct was then dialyzed against water in an expanded state over 7 days at 4°C to allow for dissolution of the core through the shell.

2.4.1.3 Nanoparticle Size Characterization

Size measurements were performed using dynamic light scattering (DLS) on a Nano-ZS90 Zetasizer (Malvern, Westborough, MA, USA).

2.4.1.4 Conjugation of Collagen-binding Peptide to Nanoparticles

SILY, with a C-terminal ‘GC’ dipeptide modification (RRANAALKAGELYKSILYGC), was custom synthesized by GenScript and received at 80% purity. This collagen-binding peptide was covalently conjugated to hollow nanoparticles with a previously reported method (114, 115). Briefly, 20 mg of nanoparticles containing 1 mol % acrylic acid were suspended at 1 mg/mL in pH 6.0 coupling buffer consisting of 0.1M MES, 500 mM NaCl. EDC and sulfo-NHS were added to final concentrations of 0.4 mg/mL and 1.1 mg/mL, respectively, for 15 minutes to activate carboxylic acids. 1 molar equivalent of N-β-Maleimidopropionic acid hydrazide (BMPH) for each mole of acrylic acid was added to react for 30 minutes at room temperature. The solution was then centrifuged and supernatant removed. The nanoparticle pellet was washed with water and centrifuged sequentially 3 times and then lyophilized. The maleimide group of the surface functionalized BMPH was then reacted with the free thiol of the C-terminal cysteine of the collagen binding peptide in 1 molar excess to ensure complete reaction with BMPH. Modified nanoparticles were then washed and centrifuged sequentially 3 times to remove excess reactants, and lyophilized.

2.4.1.5 Nanoparticle Drug Loading and Release

Carrier-free VEGF-165 was first dissolved in ultrapure water to create a 1 µg/mL loading solution, and then lyophilized nanoparticles were suspended in loading solution at a final concentration of 1 mg/mL and allowed to incubate for 24 h at 4°C in the swollen state. After incubation, particles were centrifuged for 45 minutes at 18,000g and 37°C. The supernatant was collected and centrifuged through a 100,000 MWCO NanoSep centrifugal filter to remove any residual nanoparticles. Supernatant was used to determine loading efficiency, and the nanoparticle pellet was resuspended briefly in 250 µL water before lyophilization. To assess peptide release profiles, VEGF-loaded nanoparticles were resuspended in 1 mL 37°C PBS and kept shaking in a heated plate shaker. At each time point, the loaded nanoparticles were centrifuged through a 100,000 MWCO NanoSep centrifugal filter for 45 minutes and filtrate removed for each time point. Another 1 mL of warmed PBS was then added to re-suspend the particles and continue VEGF release. For release studies, samples of drug release were taken at 3, 6, 12, and 24 h. Measurement of VEGF loaded and released into the solution were determined using VEGF-165 ELISA (R & D systems) according to the manufacturer's protocol. Solutions were diluted 100-fold to obtain readings within the detection range. It was critical that all solutions were centrifuged through the 100,000 MWCO NanoSep centrifugal filter prior to ELISA since it was found that residual nanoparticles (and their associated VEGF) interfered with ELISA VEGF detection and could cause artificially increased measurements.

2.4.2 Results

2.4.2.1 Nanoparticle Size Characterization

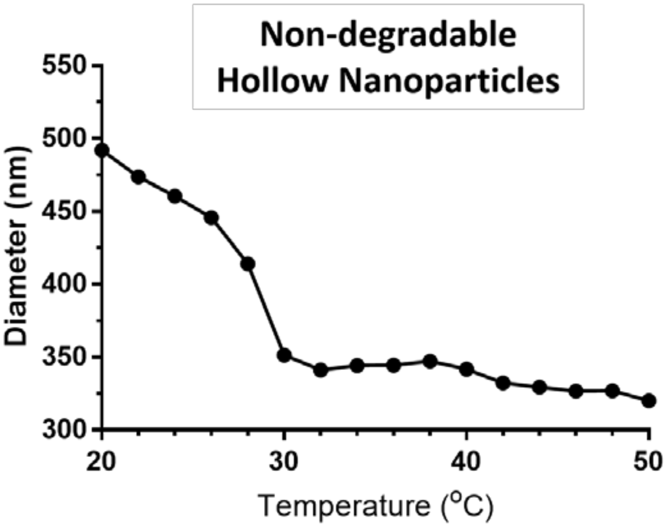

Figure 2-8. **DLS Size Characterization of Non-degradable Hollow Nanoparticles, synthesized by diffusion of an uncrosslinked core, as a function of temperature. Sample n = 3. Error bars are too short to be seen.** Non-degradable hollow pNIPAM nanoparticles exhibit an LCST of ~28°C.

Hollow nanoparticles synthesized by this alternate method using an uncrosslinked core were ~450 nm at 25°C and ~345 nm at 37°C, and exhibited an LCST at ~28°C. It appears that hollow nanoparticles exhibit a significantly lower LCST than solid nanoparticles, perhaps due to a lower particle polymer density leading to less hindered collapse.

2.4.2.2 VEGF Loading and Release

The post-loading supernatant solution revealed remarkably low residual VEGF at ~50 ng/mL resulting in a loading efficiency of 94.8 ± 0.33%, totaling ~0.95 µg VEGF loaded per mg of nanoparticles. However, only 4.9 ± 1.1% of the loaded VEGF, totaling ~47 ng VEGF per mg of loaded nanoparticles, was released over a 72 hour period at 37°C (Figure 2-9B). At the 0.6 mg/mL nanoparticle solution tested, this amounted to ~25 ng/mL released VEGF in solution over 72 hours with release rates ranging from 0.55 ng/mL to 3.4 ng/mL per hour during hours 3-12 (Figure 2-9 A & B). The loaded nanoparticles only exhibit significant VEGF release within the first 12 hours, while the remaining loaded VEGF appears to stay entrapped.

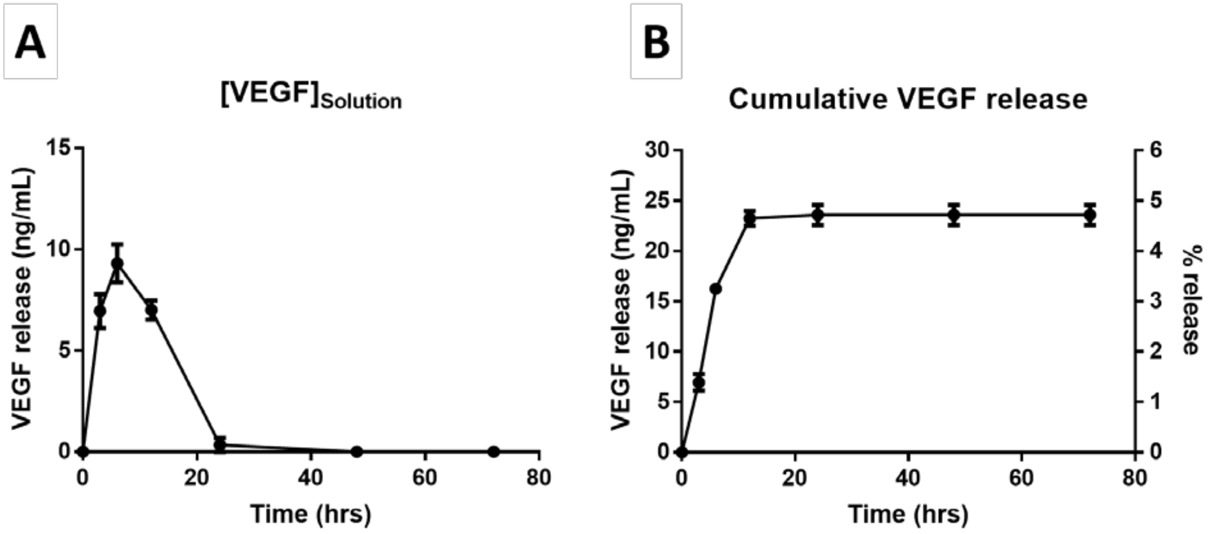

Figure 2-9. **VEGF Release from Hollow Non-degradable Nanoparticles.**

The VEGF concentration of the sample solution at each time point, after which the eluted solution is replenished with fresh PBS, (A).and the corresponding cumulative VEGF release in ng/mL and percent of initial loaded VEGF (B) is depicted as a function of time over 3 days. Sample n = 3. Error bars represent SD.

2.4.3 Discussion and Future Directions

This study demonstrated that hollow non-degradable nanoparticles could be synthesized using an uncrosslinked core, in comparison to the reducible disulfide crosslinked core that we previously reported (112). With this development, we could make the hollow nanoparticles degradable in future studies by using either the BAC or DMHA crosslinks. Given that high loading efficiencies (~95%) were achieved, the main barrier in the use of this system for VEGF delivery is the low percentage of VEGF release (~5%) and that VEGF only appears to release at significant levels for the first 12 hours. Future studies could also investigate whether loading efficiency is dependent on the concentration of the loading solution, and whether the release profile is dependent on the initial load amount. Although the total amount of VEGF released is low, the achieved ranges of 1-10 ng/mL concentrations of VEGF is optimal for stimulating endothelial cells. Future studies focusing on building in controlled release of the remaining VEGF will be important to ensure slow sustained levels of VEGF within the wound environment. This is especially critical since a large proportion of VEGF remained inaccessible and associated with the particles, and the effects of nanoparticles with tightly bound residual VEGF on tissue is unknown.

3. SYNTHESIS AND CHARACTERIZATION OF PRO-ANGIOGENIC DECORIN MIMICS

3.1 *Preface*

In this chapter, we focus on the design, synthesis, and chemical/structural characterization of pro-angiogenic peptides and 2 variants of engineered pro-angiogenic decorin mimics. A number of significant developments and discoveries were made in the synthetic chemistry and post-conjugation peptide quantification. First, we report bioconjugate chemistry using a one-step EDC reaction of peptide hydrazides, synthesized in house, with carboxylic acid moieties on glycosaminoglycans, which has only recently been described for synthesis of proteoglycan mimics. In determining peptide substitution post-conjugation, multiple methods of peptide quantification were explored and we report two high-throughput, non-destructive methods of final peptide substitution quantification. After describing the development of synthetic methods of peptides and decorin mimics, we discuss structural characterization of peptides and peptide conjugates, VEGF receptor binding properties of the VEGF-mimicking peptide ‘QK’, and protein-coated surface-binding properties of pro-angiogenic decorin mimics. Studies revealed chemical and structural changes to the glycosaminoglycans caused by the EDC reaction, and we subsequently report pilot studies exploring the biological ramifications of these changes through studying changes in VEGF receptor 2 activation. In response to these findings, we also discuss preliminary progress towards changing the synthetic chemistry to replace EDC with DMTMM to activate carboxylic acid groups. A design schematic of the proposed pro-angiogenic decorin mimics is depicted in Figure 3-1, and an outline of the breakdown of topics discussed is diagrammed in Figure 3-2.

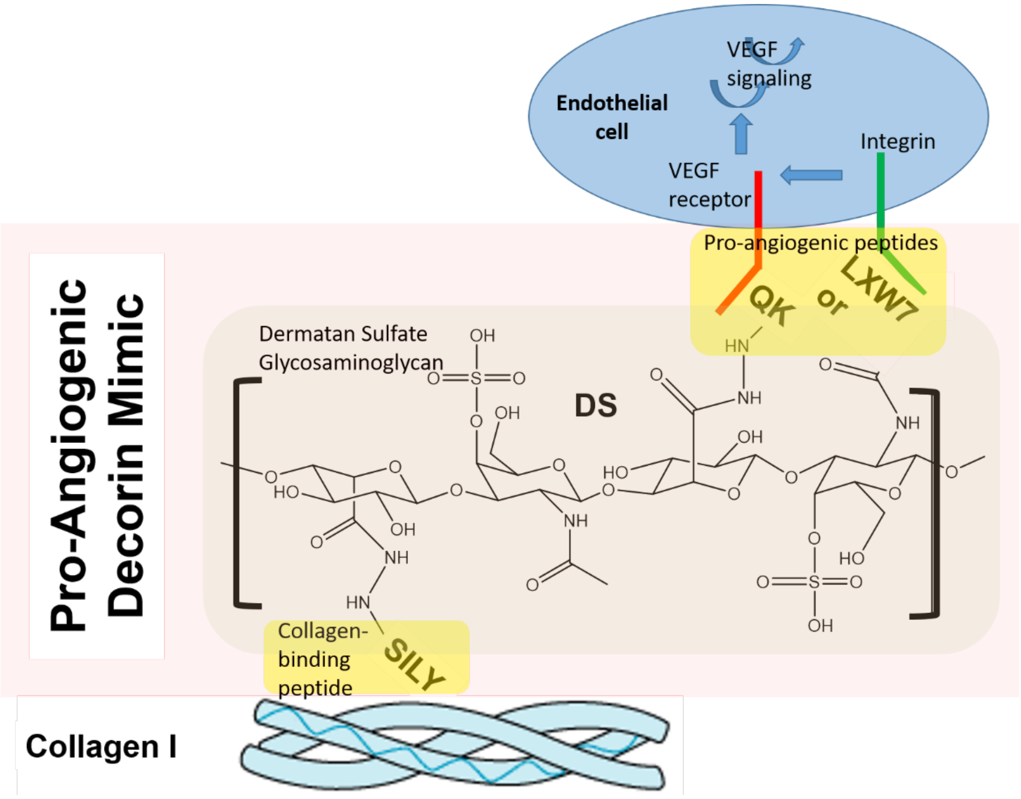

Figure 3-1. **General Design Schematic of Pro-Angiogenic Decorin Mimics**

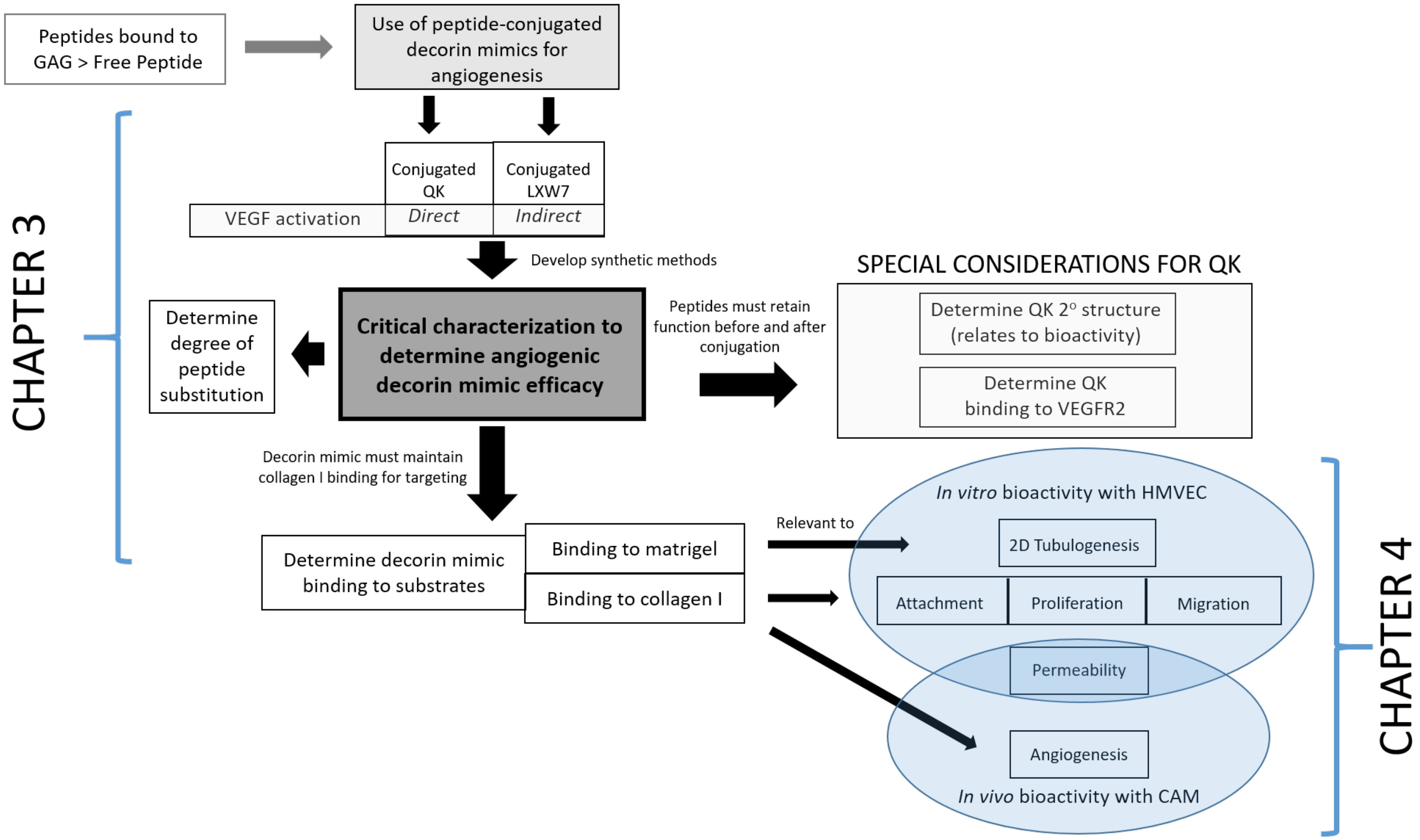

Figure 3-2. **General outline of Chapter 3 and 4 breakdown.**

3.2 *Introduction*

3.2.1 Proposed Pro-Angiogenic Decorin Mimics

Decorin is a small leucine-rich proteoglycan found abundantly in skin involved in maintaining regularity in collagen fibrillogenesis (144-146) and preventing hypertrophic scars (147). It is composed of a collagen-binding protein core attached to a dermatan sulfate (DS) side chain (116). Our lab has developed a decorin biomimetic termed DS-SILY, composed of a short collagen-binding peptide ("SILY", designed from the collagen-binding receptor on platelets (148)) conjugated to a DS backbone. Similar to the functions of decorin, DS-SILY has been shown to bind and modulate collagen fibril formation and organization, suppress excess MMP degradation of collagen, improve wound strength, and decrease scar formation by modulating collagen organization in an incisional wound environment (116). Building on this engineered therapeutic technology as a platform for tethering bioactive peptides to the DS backbone, we explored the ability of 2 different conjugated pro-angiogenic peptides, VEGF-mimicking "QK" and αvβ3 integrin-binding "LXW7", to stimulate angiogenesis through direct and indirect VEGF pathway activation, respectively. The benefits of this therapeutic design are several-fold. As previously stated, the decorin mimetic would protect native or exogenous collagen from rapid proteolytic degradation. Additionally, the use of synthetic pro-angiogenic peptides provides a scalable means of stimulating VEGF-like activity with less susceptibility to proteolytic degradation by way of reduced proteolytic sites and/or incorporation of unnatural amino acids (149, 150). Angiogenic activity would be bound to collagen in the wound bed which would limit systemic exposure, increase the local concentration of the angiogenic molecule, and mimic matrix-bound presentation of VEGF. This tethering of VEGF to the wound bed has been shown to be superior to free VEGF in diabetic wound models (100). Our proposed platform therefore creates a functional bioactive interface mimicking native extracellular matrix (ECM), which could exploit the important ECM-growth factor interactions known to regulate and potentiate growth factor activities (151-154). For instance, VEGF released from alginate beads has been shown to be 4 times more potent than an equivalent mass of VEGF (155), collagen matrix-bound VEGF has been shown to mediate sustained VEGFR2 internalization and clustering, leading to prolonged activation kinetics of the VEGF pathway (156), and heparin/heparan sulfate have been found to act as a co-receptor for VEGF activation in a synergistic manner (157, 158). Therefore our glycosaminoglycan-based therapy may interact with and potentiate endogenous or exogenous FGF and/or VEGF, while simultaneously presenting its own enhanced angiogenic stimulus. Finally, the fact that dermatan sulfate is released at high concentrations in the proliferative phase of wound healing implicates its important role as a cofactor in orchestrating wound repair (153).

3.2.2 Pro-angiogenic Peptides Activating VEGF Pathways

3.2.2.1 VEGF-mimicking Peptide "QK"

VEGF-mimicking peptide "QK", developed by *D'Andrea et al.*, is a 15 amino acid sequence (KLTWQELYQLKYKGI) representing the receptor-binding region of VEGF modified to maintain alpha helical secondary structure and VEGF bioactivity (159, 160). It has been shown to bind and induce dimerization of VEGF receptors, upregulate VEGF receptor expression, potentiate VEGF activity, and stimulate endothelial proliferation, migration, and network formation on matrigel, and induce angiogenic sprouting from *ex vivo* vessels (159, 160). *In vivo*, QK has been shown to stimulate vasodilation and neovascularization similar to VEGF in ischemic hind-limb, excisional wound healing, and matrigel plug angiogenic models (161). In the wound-healing model, QK applied directly to 20 mm diameter full-thickness excisional wounds accelerated wound closure to the same degree as VEGF therapy compared to controls. While QK has not been studied specifically on ischemic dermal wounds, exogenous VEGF therapy has been shown to improve survival of ischemic skin flaps on Sprague Dawley rats (94).

Although these studies demonstrate the promise of QK free-peptide, further studies suggest that immobilization of the peptide to a substrate preserves angiogenic properties and may even provide enhanced bioactivity, similar to previously noted matrix-interaction synergy with VEGF. Researchers have investigated the angiogenic activity both *in vitro* and *in vivo* of tethered QK to extracellular matrices, PEGDA hydrogels, or self-assembling nanofibers (162-165). Recent studies have shown increased endothelial tubule formation after "click" conjugation of QK to decellularized ECM (162), increased VEGF pathway activation and sprout formation by a collagen-binding QK peptide on collagen-coated surfaces and collagen gels (165), enhanced 2D/3D tubulogenesis and mouse corneal micropocket angiogenesis by QK conjugation to PEGDA hydrogels compared to QK alone (163), enhanced endothelial proliferation and outgrowth from encapsulated HUVEC spheroids in elastin-like polypeptide hydrogels with immobilized QK compared to free QK (166), and increased microcirculation and alleviation of hind-limb ischemia in a mouse model by QK conjugation to self-assembling nanofibers compared to its free peptide counterpart (164). Overall, these studies support the potential of an engineered pro-angiogenic proteoglycan using conjugated QK in accelerating healing of ischemic dermal wounds.

3.2.2.2 Integrin-binding Peptide "LXW7"

While the VEGF-mimicking QK peptide presents a straightforward approach of direct VEGF receptor activation, an integrin-binding peptide offers an alternative indirect mechanism of activating VEGF pathways through cross-talk and synergy between integrins and VEGF receptors. Additionally, as the proposed therapy is ECM-based, it follows that an integrin-binding peptide may further facilitate cellular transduction of this extracellular therapy. Integrins are important mediators and transducers of interactions between cells and their surrounding extracellular matrix, directly facilitating cellular attachment and migration and activating signaling cascades that alter gene expression and stimulate proliferation (167). In addition to acting as effectors of extracellular matrix cues, integrins have also been implicated in signal transduction of soluble cues such as pro-angiogenic growth factors (168). For instance, *Byzova et al.* reported that VEGF enhances adhesion and stimulates migration through the simultaneous activation of multiple integrins, including αvβ3, αvβ5, α5β1, and α2β1, via VEGFR2 (168). In particular, the activated αvβ3 integrin is the most abundant and influential in promoting angiogenesis (169-171), as VEGF has been shown to increase adhesion and migration in an αvβ3-dependent manner and activates αvβ3 more effectively than other angiogenic factors such as bFGF, IL-1, IGF, and PDGF (168). Moreover, the αvβ3 integrin has been reported to have many additional roles in angiogenesis, including localizing active MMP-2 on the vessel surface to promote ECM remodeling during endothelial invasion (172) and preventing endothelial apoptosis during active angiogenesis (168, 173). The current understanding is that VEGFR2 activation and integrin activation are heavily interrelated and synergistic in that activation of either receptor class induces binding and activation of the other (174); VEGF activates VEGFR2, physically associates with the β3 subunit to mediate VEGFR2 phosphorylation (170), signals through PI3-kinase/Akt and c-Src, and thereby increases the affinity of αvβ3 integrin to the extracellular matrix. Furthermore, anti-αvβ3 antibodies inhibit phosphorylation of VEGFR2 (170). Recent studies of the cross-talk between the VEGFR and αvβ3 integrin reveal an additional complexity whereby VEGF interactions with the extracellular matrix also modulate the VEGFR/integrin associations, affecting VEGFR clustering and prolonging activation (156).

The use of conjugated LXW7 pro-angiogenic peptide (cyclized cGRGDdvc) capitalizes on the aforementioned cross-talk between the integrin and VEGF signaling pathways while simultaneously providing added benefits of promoting cell attachment and recruitment through direct binding to integrins. This cyclic RGD peptide with unnatural D-amino acids was discovered through one-bead-one-compound screening technology to bind αvβ3 integrin with high affinity and specificity (150). When administered in free-peptide form, its integrin-binding properties are antagonistic to αvβ3-overexpressing cells, providing neuroprotection from cerebral edema after ischemic stroke by downregulating VEGF pathways (175, 176). In contrast, when surface-bound, LXW7 has been found to activate the VEGF pathway indirectly through specific binding αvβ3 integrin on both mature endothelial cells and endothelial progenitor cells (EPCs) over other blood cell types such as platelets and monocytes, and improving endothelial proliferation and directly facilitating endothelial attachment (149). This increased endothelial attachment could improve EPC recruitment and/or support exogenous EPC delivery, which may have profound effects in accelerating ischemic diabetic wound healing.

In addition to the promising potential of VEGF-based therapies for ischemic diabetic wound healing, methods of increasing EPCs at the wound site have been implicated as a therapeutic target because 1) ischemia has been found to significantly decrease the number of EPCs delivered to excisional wounds (177) leading, at least in part, to delayed healing and 2) EPC recruitment has been shown to be impaired in diabetic chronic wounds (43). During tissue granulation, both local endothelial cells and bone marrow-derived endothelial progenitor cells (EPCs) participate in neovascularization; endogenous EPCs mobilize into systemic circulation through VEGF-induced endothelial nitric oxide synthase (eNOS) activation (39, 40) and are recruited to the wound by SDF-1α, where they promote angiogenesis by expressing high levels of VEGF and bFGF (39, 40). In diabetes, EPCs have both impaired mobilization (due to reduced eNOS activity) and homing (due to reduced SDF-1α at the wound), resulting in less EPCs present in circulation (41-43) and at the wound site (43), respectively. Support for the therapeutic benefit of increasing EPCs in diabetic ischemic wounds has been exemplified by *Asai et al.*'s study, where exogenously administered EPCs accelerated wound closure in diabetic mice by incorporating into the vasculature and increasing angiogenesis and granulation (39).

Taken together, the conjugation of LXW7 to our decorin mimic has the potential for angiogenic capacity with expanded therapeutic benefit.

3.3 *Materials and Methods*

3.3.1 Materials

All peptide-hydrazides were synthesized in our lab with standard Fmoc amino acids, DIC, OxymaPure, and piperidine purchased from Aapptec. QK peptide with N-terminal acylation and C-terminal amidation was custom synthesized by GenScript, >90% purity. All organic solvents and premium grade EDC were purchased from Fisher.

3.3.2 Synthesis of Pro-angiogenic and Collagen-binding Peptide-hydrazides

Modified pro-angiogenic peptide-hydrazides of QK and LXW7 and collagen-binding peptide-hydrazide SILY (sequences in Table 3-1 and chemical structures in Figure 3-3) were synthesized based on a previously published protocol for generating hydrazide-loaded 2-chlorotrityl chloride resin (178) and standard Fmoc solid phase peptide synthesis. 2-chlorotrityl chloride resin (1.51 mmol/g, Anaspec) was rinsed sequentially 3 times with DMF, DCM, and DMF, and then swollen in 50% DCM/DMF for 1 hour. The resin was then reacted with 10% hydrazine hydrate (85%, Sigma) in synthesis grade DMF (Fisher) and 0.057M DIPEA (Fisher) for 2 hours at room temperature while bubbling under nitrogen. The solution was drained and the resin was reacted again with fresh solution for 1 more hour, after which the resin was washed 3 times with DMF and reacted with 10% methanol in DMF to cap any remaining unreacted chloride groups. The hydrazide-resin was washed again 3 times with DMF and then reacted directly with the first amino acid (4 equivalents) with HOBt/HBTU (4 equivalents) and DIPEA (10 equivalents) bubbling under nitrogen overnight at room temperature. After coupling, resin was washed thoroughly with 2x DMF, 2x DCM, IPA, and then 2x DMF. Subsequent amino acids were coupled for 20 minutes to 1 hour each at 50C on a Liberty Blue automated microwave peptide synthesizer (CEM) using 5 equivalents each of Fmoc-amino acids (Aapptec), DIC, and OxymaPure with 0.1M DIPEA and deprotected with 20% piperidine in synthesis grade DMF for 3 minutes at 60C. For N-terminal biotinylation, 5 equivalents of D-biotin (Anaspec) was coupled with 4 equivalents HBTU/HOBt and 10 equivalents DIPEA overnight at room temperature. Peptides were cleaved for 3 hours with 88% TFA, 5% phenol, 5% H_2O, and 2%

TIPS and precipitated with cold diethyl ether. Crude peptides were redissolved in 5% acetonitrile and purified to >90% purity through a C18 prep column (Spirit) against an acetonitrile (HPLC grade) gradient on an AKTApure 25 FPLC (GE Healthcare) and confirmed by MALDI-TOF mass spectrometry (Bruker). Before purification, cyclization of LXW7 was performed by oxidizing cysteine residues to form intramolecular disulfide bridges with ClearOx resin (Peptides International) according to the manufacturer's protocol.

Table 3-1**. Peptide Sequences and Conjugation Efficiency**

Sequences in 1 letter amino acid format from N to C terminus, where upper case letters indicate L-amino acids and lower case letters indicate unnatural D-amino acids, Ac indicates acetylation of the N terminus, and aeea is a short (2-(2-aminoethoxy)ethoxy)acetic acid spacer (ChemPep, Inc.) resembling PEG_2. All peptides were synthesized in our laboratory, with the exception of QK, which was custom-ordered from Genscript. Conjugation efficiency is defined as the ratio of conjugated peptide to total peptide in the reaction feed, where the total peptide was the limiting reagent. The conjugation efficiency is thereby a measure of reaction completion. For example, a conjugation efficiency of 100% indicates that all peptide added in the reaction feed was successfully covalently conjugated to the dermatan sulfate.

Peptide Name	Sequence	Chemical Formula	Molecular Weight (g/mol)	Peptide Conjugation Efficiency
QK	Ac- KLT WQE LYQ LKY KGI-amide	$C_{94}H_{146}N_{22}O_{23}$	1952.2	N/A
V	KLT WQE LYQ LKY KGI GSG-hydrazide	$C_{99}H_{156}N_{26}O_{26}$	2126.5	75%
Peg2V	KLT WQE LYQ LKY KGI –(aeea)$_2$-GSG-hydrazide	$C_{111}H_{178}N_{28}O_{32}$	2416.8	66-78%
LXW7	cG RGD dvc -(aeea)$_2$-WG-hydrazide	$C_{54}H_{84}N_{18}O_{20}S_2$	1369.5	35-40%
SILY	RRA NAA LKA GEL YKS ILY GSG-hydrazide	$C_{99}H_{166}N_{32}O_{28}$	2252.6	95-100%

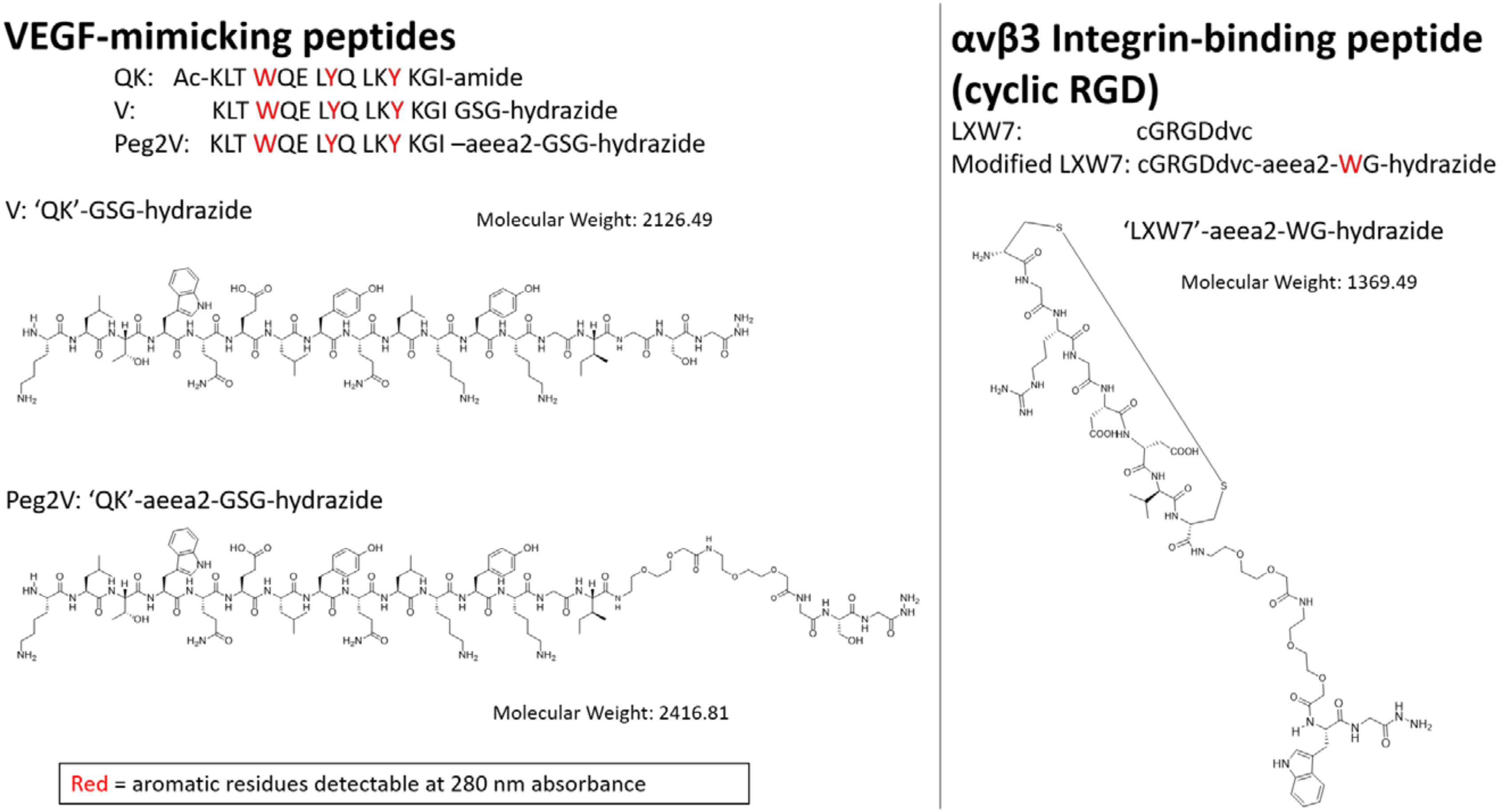

Figure 3-3. **Chemical Structures of Synthetic Peptide-hydrazides**

'GSG' tripeptide spacer sequences and/or aeea short PEG linkers were added to the C-termini of active sequences immediately preceding the C-terminal hydrazide. Note that αvβ3 integrin-binding peptide 'LXW7' is an RGD peptide cyclized by a disulfide linkage between flanking D-cysteines. Sequences are in single letter amino acid notation with upper case letters indicating natural L-amino acids and lower case letters indicating unnatural D-amino acids. Aromatic residues that could be detected by 280 nm absorbance and specific autofluorescence wavelengths (W: excitation 295 nm, emission 350 nm; Y: excitation 280 nm, emission 305 nm) are highlighted in red text.

3-1 continued

Collagen-binding peptide

SILY: RRA NAA LKA GEL YKS ILY

Modified SILY: RRA NAA LKA GEL YKS ILY GSG-hydrazide

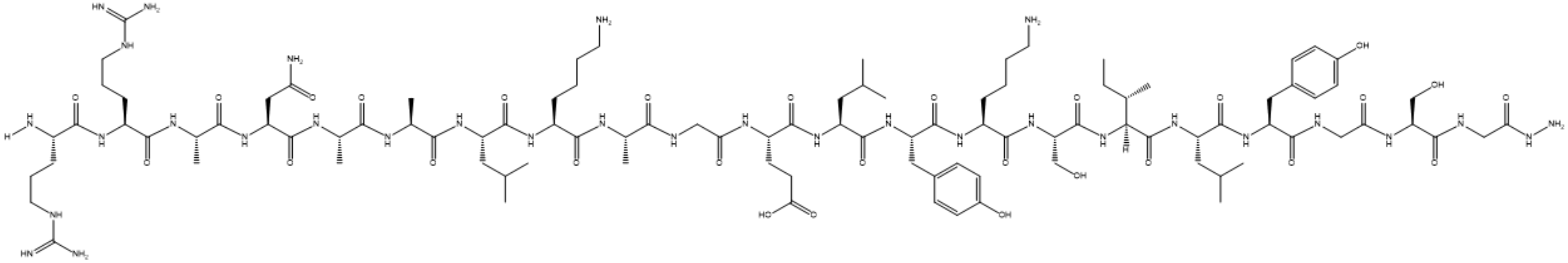

Molecular Weight: 2252.6

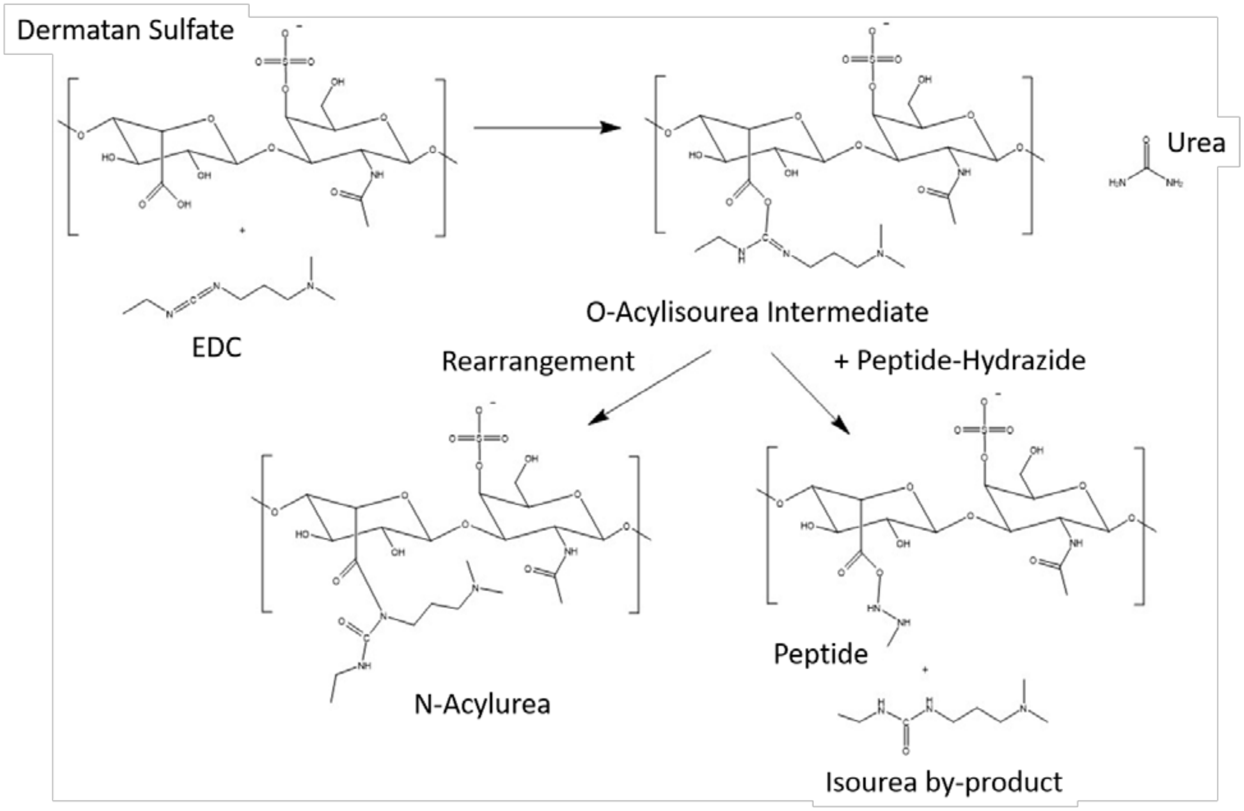

Figure 3-4. **Reaction Scheme for Peptide-hydrazide Conjugation to DS**

3.3.3 Peptide-hydrazide Conjugation to Dermatan Sulfate

3.3.3.1 EDC-activated Reaction with Peptide-hydrazide

The peptide-hydrazide conjugation reaction scheme is depicted in Figure 3-4. Carboxylic acids on dermatan sulfate (Celsus Laboratories, average MW ~46275) were activated with premium grade EDC (thermofisher) for 5 minutes in 0.1M MES buffer with 8M urea titrated to pH 4.5. Peptide-hydrazides were pre-dissolved in reaction buffer before addition to the activated DS solution with a final DS concentration of 10 mg/mL. In all reactions, the peptide-hydrazide was the limiting reagent. After 2 to 48 hours, the reaction was stopped by titrating to pH 8 with 0.5M NaOH for 30 minutes. The product was then purified by size-exclusion through 2 desalting columns (10 mL Bio-gel P6 desalting cartridges, Bio-Rad) in series on an AKTA purifier FPLC (GE Healthcare) and then lyophilized. For constructs with two different peptides, peptides were reacted sequentially with more EDC added upon conjugation of the second peptide, after taking a small sample of the reaction to quantify addition of the first peptide. Biotinylated molecules for detection of surface binding were similarly synthesized by sequentially conjugating 1 equivalent of biotinylated peptide followed by the desired equivalents of non-biotinylated peptide, taking into account conjugation efficiency. For example, a biotinylated DS-SILY$_4$ was synthesized by reacting 1 equivalent of biotinylated-SILY-hydrazide followed by 4 equivalents of SILY-hydrazide; a biotinylated DS-peg2V$_2$ was synthesized by reacting 1.33 equivalents of biotinylated-peg2V-hydrazide followed by 4 equivalents of peg2V-hydrazide. DS control molecules were also synthesized by reacting DS under the same experimental conditions with and without EDC, labeled “EDC-reacted DS” and “processed DS, no EDC” respectively, for 24 hours but without peptide. These products were also purified by size-exclusion to remove buffer salts and any unreacted EDC.

3.3.3.2 DMTMM-activated Reaction with Peptide-hydrazides

Synthetic chemistry replacing EDC with and (4-(4,6-dimethoxy-1,3,5-triazin-2-yl)-4-methyl-morpholinium chloride) (DMTMM) was performed similarly to the EDC method described above with slight modifications. DS was reacted with 4 equivalents of SILY overnight with 100 equivalents of DMTMM (Alfa Aesar) in 0.1 MES buffer with 8M urea (titrated to pH 4.5). A small sample of the solution was removed and purified by size-exclusion chromatography and lyophilized to determine completion of the DS-SILY reaction. Immediately prior to addition of LXW7, 100 equivalents more DMTMM was added to the remaining solution and left to react for either 4 hours or 28 hours before purification by size-exclusion chromatography and lyophilization. All experiments were run at room temperature except when testing the effects of heating the reaction to 37°C in an incubated plate shaker (VWR).

3.3.4 Quantification of Conjugated Peptides

All peptides were detected by concentration dependent 280 nm absorbance of aromatic amino acids on a NanoDrop One UV-Vis spectrophotometer (ThermoFisher). For increased specificity on molecules with multiple peptides, peptide quantification was confirmed by detection of intrinsic tryptophan (ex295 nm, em350 nm) and tyrosine (ex280 nm, em305 nm) autofluorescence on a SpectraMax M5 plate reader (Molecular Devices) in UV transparent 96-

well plates (Corning). All samples were prepared at 2 mg/mL in ultrapure water and analyzed by taking the average of 5 repeated readings.

3.3.5 Nomenclature of QK and LXW7-derived peptide-hydrazides and pro-angiogenic decorin mimics

QK-derived peptide-hydrazides (sequences in Table 3-1 and chemical structures in Figure 3-3) were named V and peg2V to describe the QK sequence with added GSG-tripeptide and GSG-aeea2 (PEG$_4$ spacer) on the C-termini, respectively. LXW7-derived peptide hydrazide with an aeea2-WG spacer at the C-terminus is referred to as LXW7 for simplicity. Engineered molecules were given the following nomenclature to indicate the type and number of conjugated peptides per DS: DS-(peptide)$_{\text{substitution\#}}$. For example, a decorin mimic composed of a dermatan sulfate backbone and 4 SILY substitutions per DS is referred to as DS-SILY$_4$; a mimic with 3 V peptides per DS is referred to as DSV$_3$ and a mimic with 3 peg2V peptides per DS is referred to as DS-(peg2V)$_{3.}$ Pro-angiogenic decorin mimics are indicated as (peg2V)$_{\text{substitution\#}}$-DS-SILY$_4$ or substitution#LXW7-DS-SILY$_4$ to emphasize the differing degrees of LXW7 substitution on LXW7-DS-SILY$_4$ variants. Degrees of substitution are rounded to the nearest 0.5 for simplicity.

3.3.6 Circular Dichroism (Secondary Structure Characterization of Peptides)

Circular dichroism spectra of peptides at 21.8 µM and constructs with equivalent total peptide concentrations were collected at room temperature in 0.01M potassium phosphate buffer (pH 7.1) from 185 nm to 260 nm with 4 accumulations at 50 nm/min scan speed and 4 sec DIT in 1 mm quartz cuvettes (Starna) on a Jasco J-1500 CD Spectrophotometer. CD data is converted and presented as molar ellipticity, [θ], in deg×cm^2/dmol,

$$[\theta] = 100 * \frac{\theta}{C * l} \quad ,$$

where θ is the degrees ellipticity, C is the molar concentration, and l is the pathlength in cm. CD spectra of conjugated peptides were calculated by collecting the spectra of the DS-peptide constructs with concentration adjusted to obtain 21.8 µM conjugated peptide and then subtracting out the signal for an equivalent concentration of EDC-reacted DS.

3.3.7 2-Dimensional Nuclear Magnetic Resonance

High resolution 1H, 13C, and HSQC NMR spectra of 45 mg/mL dermatan sulfate in D_2O were acquired for 6 hours on a Bruker instrument.

3.3.8 Nanodrop Absorbance Spectra

2 mg/mL samples were evaluated by absorbance spectral sweeps from 220 nm to 350 nm acquired on a NanoDrop One Spectrophotometer (ThermoScientific).

3.3.9 Characterization of Molecule Binding to Collagen- and Fibrinogen-coated Surfaces

High-binding 96-well plates (Corning) were coated with 50 µg/mL rat tail collagen I (Corning) at 4°C overnight or 2% reduced growth factor Matrigel (Corning # 354230) in basal EBM media for 30 minutes at 37°C and rinsed 3x with PBS before blocking non-specific binding with 1% Bovine Serum Albumin (BSA) for 1 hour at room temperature. For fibrinogen surfaces, a fibrinogen coating solution of ~2.75 mg/mL fibrinogen (Sigma) and 5.5 µg/mL aprotinin (Sigma) was incubated at 4°C overnight in high-binding plates. Biotinylated samples dissolved in 1% BSA were allowed to bind to the surface for 30 minutes at 37°C on a plate shaker. After 3 washes with PBS, wells were incubated with 1:200 streptavidin-HRP in 1% BSA, rinsed 3x with PBS, developed with a 1:1 A to B color solution for 20 minutes, stopped with the addition 2N H_2SO_4, and read on a Spectramax M5 platereader for absorbance at 450 nm with 540 nm correction.

3.3.10 Characterization of Binding and Activation of VEGF receptor 2 (VEGFR2)

3.3.10.1 VEGF-mimicking Peptide Binding to VEGFR2

Binding affinity was determined using bio-layer interferometry on an Octet® RED384 system (Pall ForteBio). Amine-Reactive Second-Generation (AR2G) biosensors were equilibrated in ultrapure water for 5 minutes prior to starting the protocol. Briefly for biosensor preparation involving VEGFR2 immobilization to the sensor, AR2G biosensors were equilibrated in ultrapure water for 1 minute, activated with 20mM EDC and 10mM sNHS for 5 minutes, loaded with a 25 µg/mL solution of VEGFR2 in pH 5 sodium acetate buffer for 20 minutes, and then remaining unreacted carboxylic acids were quenched with ethanolamine for 7.5 minutes (Figure 3-17A). Optimal timing of each step was determined experimentally to ensure stable equilibrium before proceeding to the next step. The prepared sensors were then immersed in equilibrating 1% milk blocking solutions for 3 minutes before exposure to VEGF or V solutions in 1% milk for 15 minutes and then in 1% milk for 15 minutes to assess VEGF and V association and dissociation, respectively, from the VEGFR2-coated surfaces. Subsequent calculation of the equilibrium dissociation constant, K_D, was calculated using ForteBio analysis of association and dissociation curves generated from multiple analyte concentrations. Concentration gradients used for VEGF were 2 fold serial dilutions from 0.30 nM to 9.5 nM, while those used for V were 94 µM to 3 mM diluted in 1% milk blocking solution.

3.3.10.2 Endothelial VEGFR2 Activation

3.3.10.2.1 Cell Culture

Human Dermal Microvascular Endothelial Cells (HMVEC, Lonza CC-2543) and Human Umbilical Vein Endothelial Cells (HUVEC, Lonza CC-2935) were expanded according to the manufacturers' protocol in EGM2-MV media and EGM-Plus media, respectively, and passaged at 70-90% confluence. Cells were cryopreserved in 80% media, 10% sterile DMSO, and 10% FBS. For experiments, HMVECs were used between passages 6 and 8, and HUVECs were used between passages 3 and 6 and maintained at 37C and 5% CO_2.

3.3.10.2.2 Multiplexed MesoScale Discovery (MSD) assay

HUVECs or HMVECs were seeded at 20000 cells per well in complete EGM-Plus growth media or complete EGM2-MV, respectively. 24 hours after plating, the media was replaced with serum-free, growth factor-free basal media (EBM) to serum-starve and synchronize the cells for 24 hours. The next day, the media was replaced with treatments, dissolved in EBM, for 5 minutes and treatment removed and cells immediately lysed with 50 µL per well of complete lysis buffer (MSD) for 30 minutes on ice. Lysates were frozen at -80C until further analysis for phosphorylated VEGF receptor 2 and total VEGF receptor 2 using a custom ELISA-type Multiplexed MesoScale Discovery (MSD) assay performed according to the manufacturer's protocol.

3.3.11 Statistical Analysis

All quantitative data is presented as mean ± standard deviation, and statistical significance was evaluated by ordinary one-way ANOVA using post-hoc Dunnett's or Tukey's tests for multiple comparisons with values $p < 0.05$ denoted as significant.

3.4 *Results and Discussion*

3.4.1 Pro-angiogenic Decorin Mimic Design and Development

3.4.1.1 Design of Quantifiable Peptide-hydrazide Sequences with Preserved Post-conjugation Bioactivity

Active peptide sequences from literature were modified with short amino acid and/or short PEG spacer sequences to ensure that the peptides were freely accessible for cellular interactions after conjugation to dermatan sulfate. All peptides were synthesized as C-terminal hydrazides to allow preferential C-terminal EDC-conjugation over internal primary amines at low pH. Although unmodified QK and SILY peptides both contain multiple aromatic amino acids facilitating conjugated peptide quantification using 280 nm absorbance and intrinsic autofluorescence, the original LXW7 peptide sequence needed to be further modified by addition of a C-terminal tryptophan for ease of downstream non-destructive quantification. As expected based on greater 280 nm absorbance for tryptophan compared to tyrosine, we found that the 280 nm absorbance method was more sensitive for quantification of QK-derived peptides and LXW7 than SILY (Figure 3-5). Non-destructive quantification of 2 different sequentially conjugated peptides by analyzing 280 nm absorbance of samples immediately before addition of the second peptide provided adequate substitution estimates under the assumption that the conjugation reaction of the first peptide was complete. We achieved more specific quantification of final peptide substitution on proteoglycan mimics containing both LXW7 and SILY measuring intrinsic autofluorescence of tryptophan (ex295 nm, em350 nm) and tyrosine (ex280 nm, em305 nm). For this particular peptide combination, the autofluorescence parameters allowed for specific detection of each peptide without significant signal interference from the other peptide (Figure 3-6). Quantification of mimics with both QK-derived peptides and SILY was also possible by the UV autofluorescence method, although the tyrosine signal included contributions from both peptides.

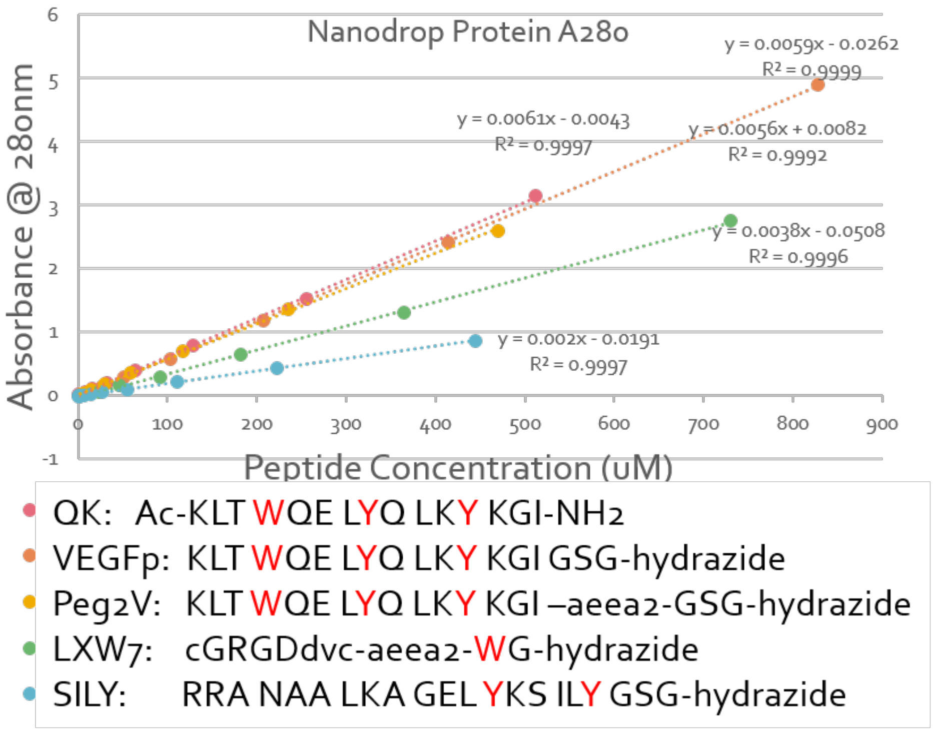

Figure 3-5. **Standard Curves of Peptide Absorbance at 280 nm as a Linear Function of Peptide Concentration.**

These standard curves were used as a high throughput, non-destructive method to quantify peptide conjugation by Nanodrop. A_{280nm} of Tryptophan > A_{280nm} of Tyrosine.

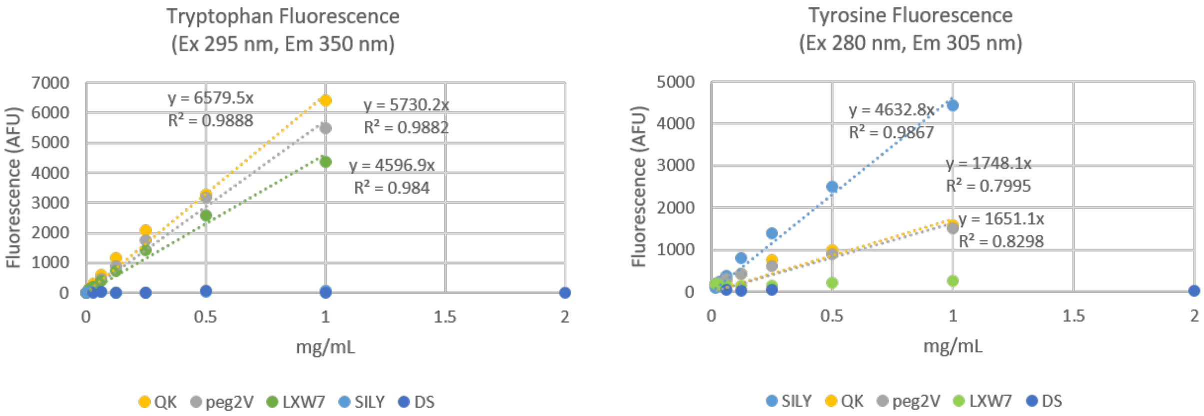

Figure 3-6. **Standard Curves of Peptide UV Autofluorescence at Specified Emission and Excitation for Tryptophan and Tyrosine as a Linear Function of Peptide Concentration.**

These standard curves were used as a high throughput, non-destructive method to quantify peptide conjugation. $UV_{autofluorescence}$ of Tryptophan > $UV_{autofluorescence}$ of Tyrosine.

3.4.1.2 Optimization of Peptide-specific EDC-hydrazide Conjugation Chemistry

In the synthesis process, we discovered that peptide conjugation efficiency (defined as peptide equivalents successfully attached out of total reacted equivalents) to the dermatan sulfate backbone was peptide dependent. Coupling of SILY was nearly 100% efficient after 2 hours of reaction, while coupling of QK-derived peptides was only ~70% efficient after a 4 hour reaction and coupling of LXW7 suffered the lowest efficiency at ~35-40% even after 48 hours of reaction and additional EDC (Table 3-1). In addition to peptide-specific conjugation efficiencies, we also found that comparable conjugation of SILY equivalents, as assessed by similar 280 nm absorbance, could be achieved with EDC activation of as few as 20% of the available carboxylic acids on DS (assuming approximately 100 carboxylic acids per dermatan sulfate) (Figure 3-7), whereas similar reduction of EDC significantly negatively impacted LXW7 conjugation. Given the vast differences in peptide conjugation efficiencies, it is likely that structural and steric effects affect the chemistry in a sequence-specific manner. We attempted to improve LXW7 coupling by using linear LXW7 in hopes of reducing steric hindrance during conjugation and cyclizing the peptide after conjugation; however, Ellman's assay revealed significantly fewer free thiols than expected after conjugation and it was determined that the thiols in the linear peptide were consumed through irreversible reaction with EDC (Figure 3-8), an observation that is supported in literature (179). By adjusting several experimental parameters, including lengthening reaction time, better controlling pH, increasing peptide equivalents, and adding more EDC over the course of the reaction, we achieved a maximum of 5.5 cyclized LXW7 peptides per DS. In dual peptide conjugation, we also discovered that the order of peptide addition was crucial to achieving desired peptide substitution. SILY conjugation efficiency drastically decreased to 20-50% when it was added as the second peptide (depending on the identity and quantity of the first peptide), while other peptides appeared to maintain relatively constant conjugation efficiency regardless of addition order; therefore, SILY peptides were added first in a dual peptide conjugation sequence.

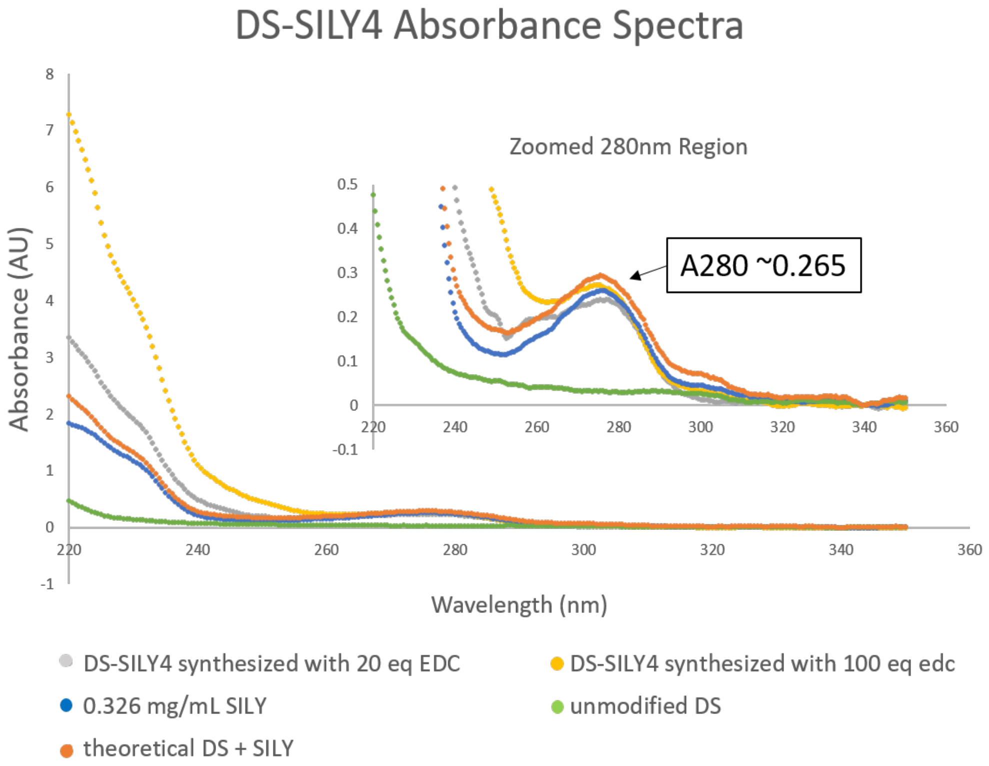

Figure 3-7. **DS-SILY₄ Absorbance Sweeps.**

Comparable SILY conjugation is achieved using 20 versus 100 equivalents of EDC.

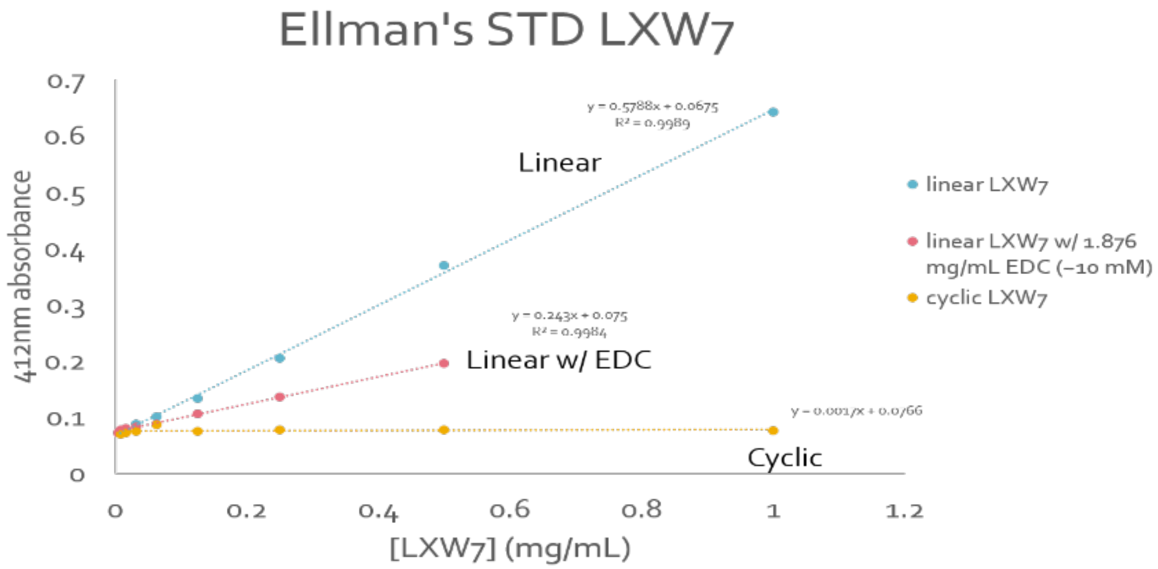

Figure 3-8. **Ellman's Assay Detection of Free Thiols on Linear LXW7 After Reaction with EDC**.

Free thiols in linear LXW7 are reduced after EDC addition, showing that EDC causes irreversible consumption of free thiols. Cyclic LXW7 shows no detection of free thiols, indicating complete cyclization through oxidation of free thiols.

3.4.1.3 Peptide-hydrazide Conjugation using DMTMM: Pilot Studies

Given the low conjugation efficiency of LXW7 using EDC, pilot studies replacing EDC with the DMTMM activator were investigated in the synthesis of LXW7-DS-SILY constructs, based on improved conjugation by DMTMM over EDC/NHS observed by *D'Este et al.* in hyaluronan substitution studies of reactions over 5 days (180). LXW7-DS-SILY constructs were synthesized by first conjugating SILY to form DS-SILY$_4$, and then sequentially adding desired equivalents of LXW7 to the reaction feed. First, we observed that the DMTMM reaction proceeded more slowly than EDC, as some unreacted SILY remained in a 2 hour DMTMM reaction, which was not present for a 2 hour EDC reaction. The DMTMM reaction needed to be extended overnight for complete conjugation of 4 equivalents of SILY. Furthermore, in this initial synthesis of DS-SILY$_4$ after an 18 hour overnight reaction with DMTMM, we observed a 280 nm absorbance of ~0.37, representing a super-theoretical calculated conjugation efficiency of SILY (calculating >4 equivalents conjugated SILY, whereas only 4 equivalents of SILY was added to the reaction). In comparison, 280 nm absorbance was ~0.27 for the corresponding DS-SILY$_4$ sample synthesized with EDC in a 2 hour reaction, representing 100% conjugation efficiency of 4 SILY equivalents. The super-theoretical 280 nm absorbance observed in the DMTMM reaction might be attributed to some co-purified or conjugated DMTMM that did not separate as effectively by size-exclusion chromatography and may cause additional sample absorbance at 280 nm. After sequential LXW7 conjugation, net absorbance values were used to calculate additional absorbance attributed to conjugated LXW7, and the calculated degree of substitution for the tested reaction conditions are presented in Table 3-2. Note that there was a total of 200 equivalents of EDC or DMTMM activator added to the batch reaction, where the first 100 equivalents were added for SILY conjugation and the next 100 equivalents were added immediately prior to LXW7 conjugation.

Table 3-2. **Degree of LXW7 substitution of LXW7-conjugated DS-SILY constructs synthesized by EDC versus DMTMM activation of carboxylic acids on DS.**

200 eq. total EDC	LXW7 equivalents added		
Reaction time	5 eq LXW7	10 eq LXW7	20 eq LXW7
18 hours	**1.9**	**3.3**	**4.6**
48 hours	**--**	**4.0**	**4.7**

200 eq. total DMTMM	LXW7 equivalents added	
Reaction time	5 eq LXW7	10 eq LXW7
4 hours	**1.3**	**2.5**
28 hours	**3.2**	**8.4**
48 hours	**--**	**8.7**

DMTMM activation significantly improved LXW7 conjugation efficiency over EDC for equivalent LXW7 reactant concentrations, reaching ~87% within 48 hours with 10 equivalents of LXW7 added. Although longer reaction time significantly improved the LXW7 conjugation with DMTMM, there was still unreacted product even after 48 hours. Given that the LXW7 conjugation appeared to conjugate slower than SILY or QK conjugation (both peptides reached >60% completion within 4 hours) based on the EDC reaction and that DMTMM reactions progressed slower than EDC reactions, we then tested whether reaction heating could accelerate conjugation. The results for reactions at 37°C are presented in Table 3-3.

Table 3-3. **Degree of LXW7 substitution of LXW7-conjugated DS-SILY constructs synthesized by room temperature versus heated DMTMM reaction.**

200 eq. total DMTMM	10 equivalents of LXW7 added	
Reaction time	Room Temp	37°C
24 hours	**6.8**	**6.1**
48 hours	**8.7**	**6.9**

Heating the DMTMM-activated reaction unexpectedly decreased the efficiency of conjugation in our studies, contrary to findings reported by *Loebel et al.* where heating to 37°C improved conjugation of tyramine to hyaluronan at all reaction times until 120 hours (181). Interestingly, *Loebel et al.* also observed that at 37°C, maximal conjugation occurred after ~10 hours but then decreased conjugation over increasing reaction time, suggesting that the conjugation was reversible and/or the tyramine degraded or detached from the hyaluronan after prolonged heating. In contrast, conjugation continuously improved over 120 hours with DMTMM at room temperature. If the DMTMM conjugation of peptide-hydrazides progresses similarly to that described in *Loebel et al.*, it is possible then that the tested heated reaction times are too long and maximum conjugation could be reached prior to 24 hours. However, since we observed a slight increase in conjugation with prolonged heating at 48 hours, additional studies investigating both shorter and longer time points for the heated reaction may be necessary to understand the kinetics of the heated reaction. Based on the preliminary results, we do not suggest heating the DMTMM reaction for our synthetic scheme unless these additional heated studies are performed, as we achieved the greatest conjugation efficiency at prolonged room temperature reactions.

3.4.2 Characterization of Free and Conjugated Peptides

3.4.2.1 Modified VEGF-mimicking Peptides Maintain Alpha-helical Secondary Structure Before and After Conjugation

From its conception, QK peptide’s α-helical secondary structure was determined to be crucial to its pro-angiogenic bioactivity (159). Thus it was important to first determine any peptide conformational changes upon spacer and hydrazide C-terminal modifications, as single amino acid modifications can have significant effects on secondary structure and the addition of a ‘GSG’ tripeptide spacer was predicted by computational modeling to cause C-terminal uncoiling (Figure 3-9). Upon conjugation to dermatan sulfate, the VEGF-mimicking peptides could also change in structure, as some proteins have been reported undergo conformational and/or structural changes after binding to glycosaminoglycans (GAGs). For example, *Wijelath et al.* reported evidence of heparin modulation of VEGF-A165 (but not VEGF-121) secondary structure, increasing α-helical content (182). Peptide secondary structure is commonly detected by circular dichroism (CD) analysis through identification of characteristic spectral signatures, with an α-helical signature represented by negative peaks at 208 nm and 222 nm and a positive peak at 193 nm. We therefore used CD to investigate 1) whether the modified VEGF-mimicking peptides maintained alpha helical structure before conjugation and 2) whether the close association of peptides with DS after conjugation would alter their structure. As seen in Figure 3-10A, CD spectra of modified QK peptides (V and peg2V) very closely matched the original α-helical QK signature, despite the addition of GSG tripeptide and GSG-peg$_2$ C-terminal spacers for V and peg2V respectively and C-terminal hydrazide modification. Importantly, as seen in Figure 3-10E, V and peg2V also maintained the α-helical signature after conjugation to dermatan sulfate, since the differences between the conjugated and free peptide CD spectra were minimal.

This is an essential finding as it demonstrates that the close proximity of the highly negatively charged dermatan sulfate molecule does not distort peptide secondary structure.

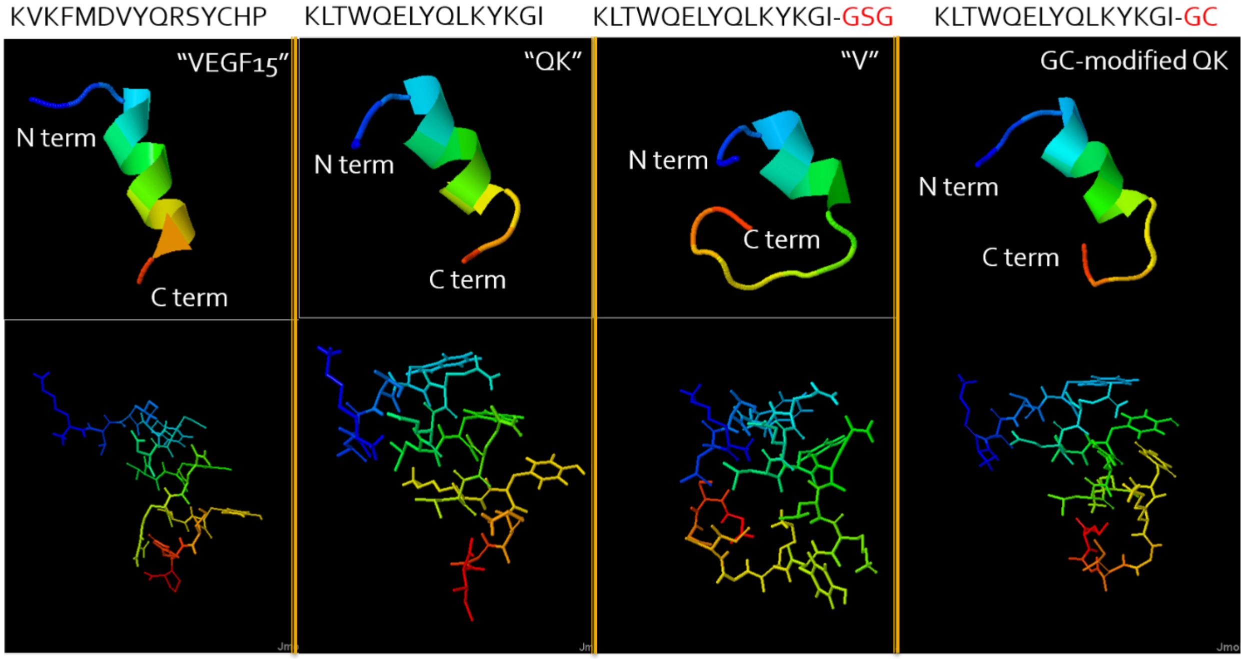

Figure 3-9. **Theoretical Secondary Structure of VEGF-mimicking Peptide Sequences Modeled by PepFold Software (183, 184).**

Top row is a cartoon representation, emphasizing overall backbone secondary structure of the peptide indicated in the upper right corner with the peptide sequence specified above each column. Bottom row represents the corresponding wire model structure highlighting the orientation of side chain projections. "VEGF15" is the native peptide sequence present spanning the VEGF receptor 2 binding region, which was found experimentally by CD to be uncoiled outside the context of the full VEGF protein by *D'Andrea et al (159)*.

For a comprehensive analysis, we also investigated CD of LXW7 and SILY peptides before and after conjugation to dermatan sulfate. In comparison to the α-helical structure of VEGF-mimicking peptides, LXW7 had a slight negative signal from 185 to 205 nm and almost no CD signal in other wavelengths examined, while SILY revealed a signature resembling a random coil of a denatured triple-helix with a minimum at 198 nm and low ellipticity above 210 nm (185). Like free LXW7, conjugated LXW7 also had almost no CD signal, although the minimal signal was slightly positive in the 185 to 205 nm range (Figure 3-10F). For SILY peptide, conjugation resulted in a significantly more negative and slightly right shifted spectrum but still lacking a positive signal in the 210 to 230 nm range, perhaps indicative of a slightly more organized collagen-like triple helix (Figure 3-10F). A finding of a collagen-like triple helix signature for SILY peptide is not surprising and may help SILY bind to fibrillar collagen.

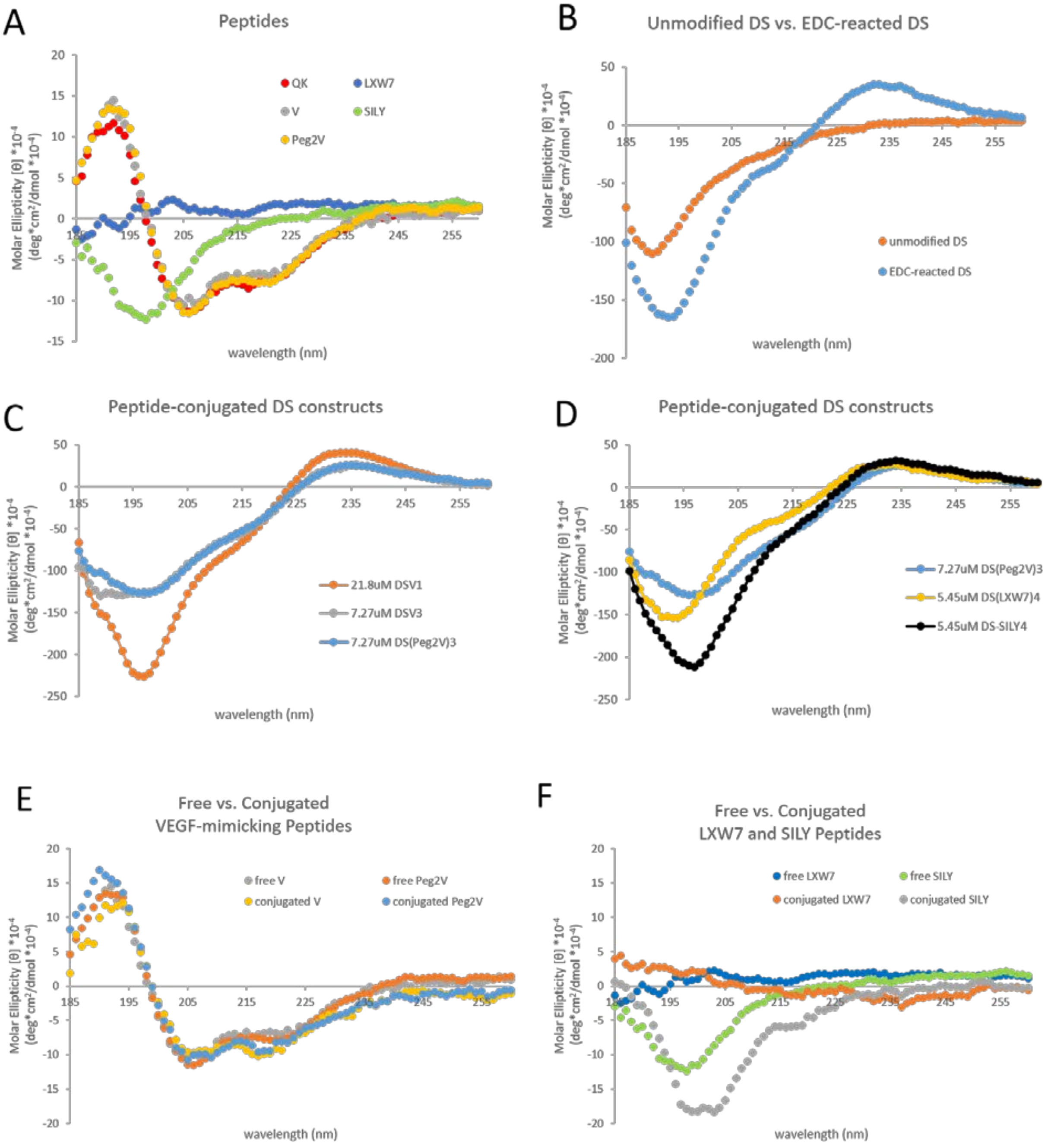

Figure 3-10. **Circular Dichroism (CD) Spectra of Peptides Before and After Conjugation to Dermatan Sulfate.**

CD spectra of free peptides (A) and DS-conjugated peptides (E & F). Subfigure B shows DS structural changes caused by reaction with EDC alone, which served as a background signal that was subtracted from total CD signal observed from peptide-conjugated DS constructs (C & D). Subfigure C highlights the differences in CD signal from DSV_3 compared to $DS(Peg2V)_3$, indicating changes attributed to the addition of a short peg linker present in peg2V. It also highlights that the deepened negative peak around 198 nm and positive peak 235 nm are more pronounced in DSV_1, which is measured at a higher overall concentration to keep peptide concentration constant, and exhibits the same major features seen in the EDC-reacted DS curve in subfigure B. Subfigure D highlights overall CD differences between the $DS(Peg2V)_3$, $DS(LXW7)_4$, and $DS\text{-}SILY_4$ constructs.

3.4.3 EDC Activation Produces Irreversible Structural Changes in Dermatan Sulfate

In gathering the CD spectrum of V peptide conjugated to DS (denoted DSV), we discovered that lower substitution DSV_1 had a greater negative peak around 200 nm than DSV_3 (Figure 3-10C). Since the DSV_1 concentration assessed was 3 times greater than DSV_3 in order to match samples for total peptide concentration, the larger negative peak was attributed to a higher overall concentration of DS. Upon background subtraction of the unmodified DS spectra, the resultant curves generally followed the expected α-helical features but displayed unexpected positive features in the 225 to 245 nm range (data not shown). This led us to explore changes in the DS spectra coming from the EDC reaction. In this investigation, we observed an unexpected change in the CD spectra of EDC-reacted DS (Figure 3-10B), indicating a GAG structural/conformational change induced by the EDC reaction. The CD spectrum had pronounced deepening of the negative peak around 200 nm and a new positive peak at 235 nm, most closely resembling the CD spectra of intact collagen triple helices (185) although the positive peak is slightly more right-shifted. Since the products were purified by size-exclusion prior to CD analysis, these changes could be attributed to covalent addition of EDC or co-purified EDC due to strong association. We then used 1H and 13C 2D NMR analysis, which revealed multiple new protons at 1, 1.1, 2.8, 3, 3.1, and 3.2 ppm (Figure 3-11A) and new carbons at 14, 15, 25, 35, 36, and 160 ppm on DS after the EDC reaction (Figure 3-11B). Additionally, absorbance spectral sweeps seen in Figure 3-12 demonstrated increased absorbance at 220 nm proportional to the amount of reacted EDC, likely due to new imide bonds (resembling amide bonds). CD, NMR, and absorbance data together indicate that EDC reacted covalently and irreversibly through O-acylisourea rearrangement to stable N-acylurea after carboxylic acid activation (Figure 3-4). Furthermore, the progressive increase in 220 nm absorbance with 20 equivalents versus 100 equivalents of EDC in Figures 3-7 and 3-12 suggested that the DS-$SILY_4$ synthesized with 20 versus 100 equivalents of EDC differed in the amount of N-acylurea attached to the DS backbone.

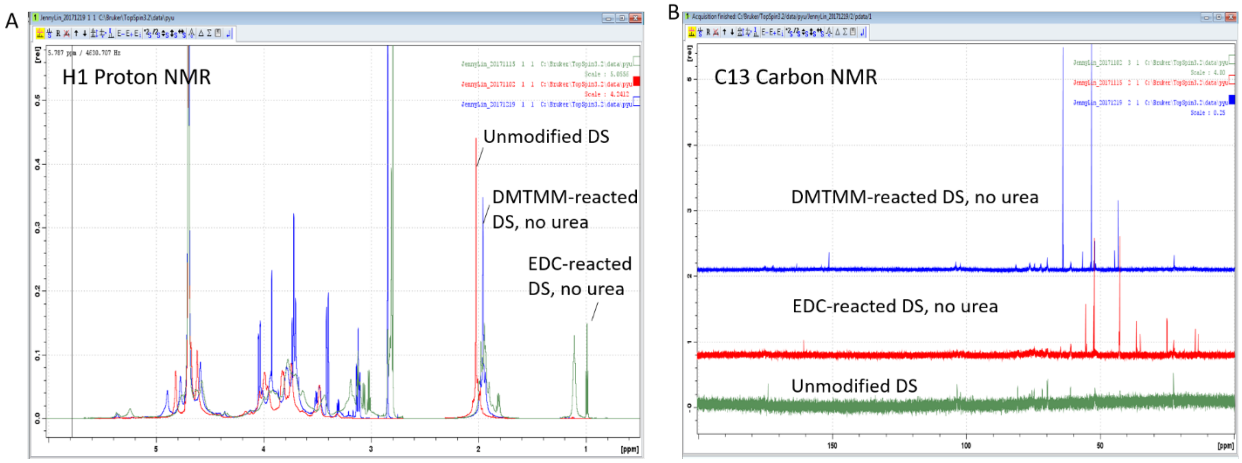

Figure 3-11. **1H Proton NMR (A) and 13C Carbon NMR (B) Spectra of Unmodified DS, EDC-reacted DS, and DMTMM-reacted DS.**

Multiple new protons and carbons are found on EDC-reacted DS compared to unmodified DS.

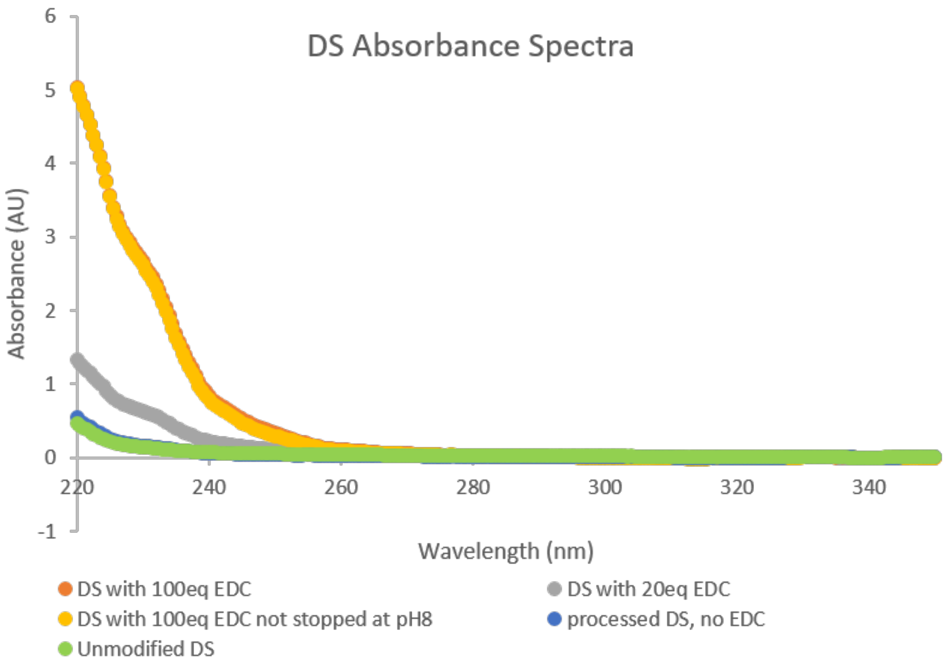

Figure 3-12. **Absorbance Spectral Sweep of Unmodified DS and DS after a 24 Hour Reaction with varying amounts of EDC.**

Absorbance at 220 nm rises with increasing EDC.

3.4.4 Potential Biological Implications of N-acylurea

Irreversible N-acylurea formation with EDC has been well documented in literature (186, 187), and is likely more abundant in the given reaction due to the lack of NHS, even though the molar ratio of EDC to carboxylic acid groups was approximately 1:1. Due to modification of the carboxylic acid, the N-acylurea EDC adduct would reduce the overall negative charge on DS at neutral pH. The change in charge is the most likely cause of the observed conformational change and potentially affects DS' electrostatic interactions with other biological molecules. These types of EDC-altered molecule interactions have previously been reported on proteins by *Huckett et al.* (188), whereby electrostatic changes caused by N-acylurea altered protein binding to DNA. *Oliveira et al.* also reported similar changes to GAGs, whereby the heparin binding to cationic dyes, heparin susceptibility to heparinases, electrophoretic behavior, and anticoagulant properties were impaired by EDC reaction (189). GAG-growth factor interactions are known to be responsible for modifying growth factor biological activity, and thus these irreversible changes to GAG charge and structure may significantly affect DS' therapeutic activity.

In our preliminary investigation of the biological significance of the EDC-induced changes, we compared the proliferative effects of DS-SILY$_4$ synthesized with 20 versus 100 EDC equivalents on HMVECs. Our results suggested that a higher amount of N-acylurea did not negatively impact and may even stimulate proliferation both in soluble (Figure 3-13A) and collagen-bound forms (Figure 3-13B).

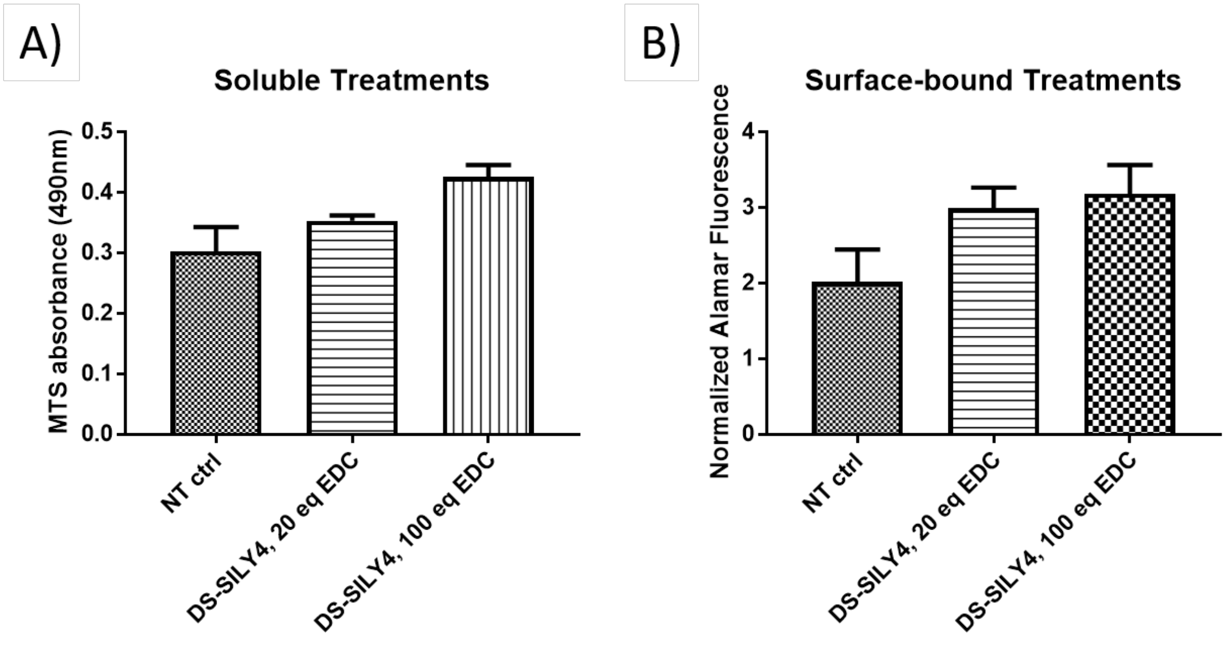

Figure 3-13. **Effects of increasing EDC on HMVEC Proliferation after 72 hour exposure to soluble treatments and 144 hour exposure to surface-bound treatments.**

Sample n = 4, with measurements presented as mean ± standard deviation.

3.4.4.1 N-acylurea Addition to DS Impairs its Ability to Potentiate VEGF

To further explore the biological ramifications of N-acylurea, we studied changes in the VEGF receptor activation and total VEGF receptor 2 levels in the presence and absence of VEGF. Preliminary data showed that, in the absence of VEGF, unmodified DS and EDC-reacted DS produced statistically identical responses, as measured by phosphorylated VEGFR2 and total VEGFR2. Without VEGF, 5 minute stimulation with EDC-reacted DS decreased the total VEGFR2 to the same degree as unmodified DS, and neither unmodified DS nor EDC-reacted DS had any significant effect on phosphorylated VEGFR2 (Figure 3-14 A & B). However, in the presence of VEGF, differences in activity were apparent. 5 minute VEGF stimulation resulted in a significant increase in VEGFR2 phosphorylation (Figure 3-14D), while total VEGFR2 levels decreased (Figure 3-14E), which can be accounted for by endocytosis and subsequent degradation of activated VEGF receptors during recycling/desensitization. Unmodified DS increased the VEGF-induced phosphoVEGFR2 (Figure 3-14D) and simultaneously prevented receptor downregulation thereby prolonging the VEGF response (Figure 3-14E), a significant finding has not yet been reported in literature. In contrast, the EDC-reacted DS was unable to elicit increased phophoVEGFR2 or prevent VEGFR2 downregulation, showing no significant effects compared to the VEGF control (Figure 3-14E). These findings dependent on the presence of VEGF suggested that the N-acylurea addition did not significantly change intrinsic DS interactions with the VEGF receptor, but caused altered DS interactions with VEGF that perhaps prevent it from potentiating and/or prolonging VEGF responses. It is possible that the altered charge and conformation of N-acylurea addition does not allow effective VEGF binding, or alternatively the DS may be binding up VEGF and other growth factors in a manner that does not synergize their activities.

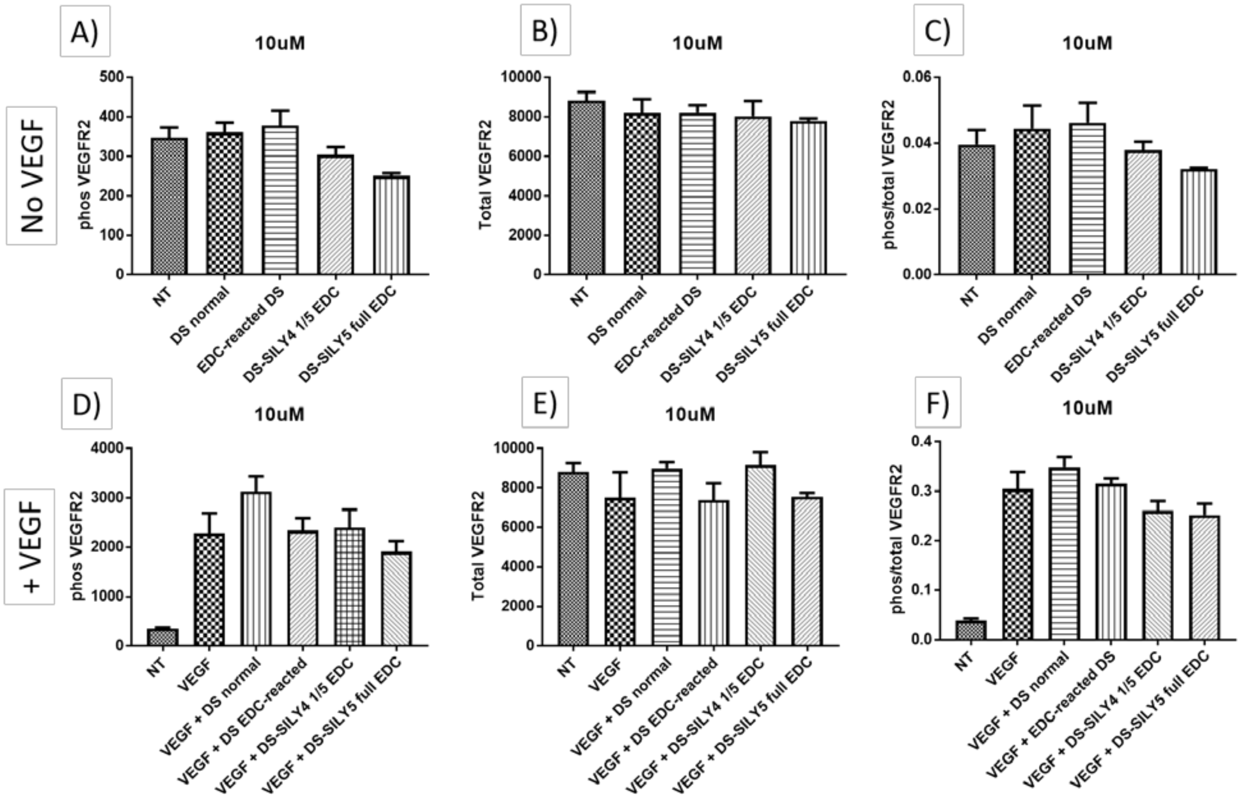

Figure 3-14. **MSD Phosphorylated and Total VEGFR2 Activity after 5 minute Stimulation of HMVECs.** Subfigures A and D represent phosphorylated VEGFR2, while subfigures B and E represent total VEGFR2 levels. Subfigures C and F are calculated phosphorylated/total VEGFR2. Sample n = 3, with measurements presented as mean ± standard deviation.

3.4.4.2 SILY Addition to DS does not Affect Total VEGFR2 Levels, but Decreases VEGFR2 Phosphorylation and N-acylurea Exacerbates this Effect

Interestingly, the addition of SILY changed the dynamics of the DS with VEGF receptors in both the absence and presence of VEGF. In the absence of VEGF, while DS-SILY$_4$ had no effect on total VEGFR2 compared with DS (Figure 3-14B), DS-SILY$_4$ with 20 EDC equivalents decreased phosphoVEGFR2 below the DS and untreated controls, and this effect was amplified in DS-SILY$_4$ with 100 EDC equivalents (Figure 3-14A). SILY addition thereby appeared to decrease constitutive VEGFR2 phosphorylation, and greater amounts of N-acylurea seemed to exacerbate this effect. In the presence of VEGF, DS-SILY$_4$ with 20 EDC equivalents had a similar effect as unmodified DS on total VEGFR2 (Figure 3-14E), allowing a prolonged response by preventing VEGFR2 degradation. In contrast, DS-SILY$_4$ with 100 EDC equivalents resulted in responses similar to EDC-reacted DS. Therefore the effects seen in the presence of

VEGF is governed by the amount of N-acylurea. It follows that SILY addition itself did not affect DS' ability to prevent total VEGFR2 degradation in the presence of VEGF, but rather the total VEGFR2 level caused by DS-SILY$_4$ made with 100 EDC equivalents is governed by its increased N-acylurea. Although SILY addition appeared to quench DS' ability to potentiate VEGF-induced receptor phosphorylation (Figure 3-14D), this can largely be attributed to the fact that SILY itself decreases receptor phosphorylation. The even greater decrease in phosphoVEGFR2 seen with DS-SILY$_4$ made with 100 EDC equivalents is thus the result of a combination of greater N-acylurea substitution prevented phosphoVEGFR2 synergy, and the addition of SILY further negatively affected receptor phosphorylation.

The negative effect of SILY on VEGFR2 phosphorylation might be explained at least in part by the fact that the SILY carries a positive net charge of 3^+ per peptide, such that its conjugation to DS not only eliminates a carboxylic acid, but also adds positive charge, serving to change the overall charge of DS. Based on the VEGFR2 activation studies alone, DS-SILY$_4$ should not stimulate endothelial proliferation, contrary to our observations in Figure 3-13 and previously reported proliferative effects for DS-SILY$_{20}$ using oxidation-type synthetic chemistry (190). Furthermore, the VEGFR2 activation studies do not support the observation that the increased N-acylurea had no negative effects on proliferation. Therefore, we must conclude that DS-SILY and N-acylurea stimulate proliferation through mechanisms not elucidated by this study. However, there are some limitations to our VEGFR2 activation analysis. First, the experimental design only allows us to compare acute responses to soluble factors, while the VEGFR2 activation is a highly dynamic process in which a singular time point cannot capture the nuances of sustained activities likely present due to the known ability of GAGs to sequester growth factors and function as a controlled release system. Thus there may be other complexities in the pathway that we cannot account for, and the discrepancy between the receptor activation data and the biological proliferative response needs to be explored further by specifically looking at growth factor binding and controlled release, as well as the time-dependent levels of downstream second messengers like MAPK and ERK.

3.4.5 Pro-angiogenic Decorin Mimic Targeting: Relative Surface-binding of Molecules to Extracellular Matrices

Since our proposed therapy is designed to target angiogenic activity to an ischemic wound site by tethering to extracellular matrix, investigating these binding properties was critical to determine whether decorin mimic targeting was altered after conjugation of additional peptides. The ability of pro-angiogenic decorin mimics to bind to collagen and fibrinogen coatings was investigated using streptavidin-HRP detection of surface-bound biotinylated molecules after a 30 minute incubation with a protein-coated surface. The initial experiments shown in Figure 3-15A demonstrate baseline characterization of DS-SILY$_4$ to collagen I, matrigel, and fibrinogen surfaces. Previously, our lab has characterized collagen I targeting and subsequent modulation of collagen fibrillogenesis, critical for providing scarless healing in incisional wounds (116), by similar decorin mimics DS-SILY$_{20}$ synthesized with oxidation chemistry (191). We were also interested in the decorin mimic's ability to bind other collagens such as collagen IV, which is important during the re-epithelialization of dermal wounds (192). In previous cardiovascular applications of DS-SILY$_{20}$, the decorin mimic was also studied for anti-platelet activity by binding to injured luminal vascular surfaces in cardiovascular applications (191), further justifying investigation of its targeting to basement membrane proteins, such as collagen IV and laminin, and binding to these proteins was studied through molecule binding to matrigel. Finally, given the role of clotting in the primary stages of wound healing and dermatan sulfate's anti-thrombotic activity, the ability of DS-SILY$_4$ to bind fibrin/fibrinogen was also of interest.

3.4.5.1 DS-SILY$_4$ has higher binding capacity and affinity for collagens I and IV compared to fibrinogen.

Using standard surface coating procedures for collagen (50 µg/mL) and matrigel (2%), ~7.5 µg/cm^2 rat tail collagen I and ~28 µg/cm^2 matrigel were allowed to bind to a high bind plate. Based on Corning's reported composition of matrigel (60% laminin, 30% collagen IV, and 8% entactin), the amounts of collagen I versus collagen IV in the standard coating protocols should be comparable and thus the results of this experiment were assumed to reflect differential binding of molecules to collagen I versus collagen IV and laminin. Figure 3-15A shows that DS-SILY$_4$ bound in a dose-dependent manner to collagen I, collagen IV/laminin, and fibrinogen with *binding* capacities of 1.6, 1.1, and 0.30 AU respectively. Figure 3-15A also shows that binding detection on a plate coated with collagen following our reported protocol was roughly equivalent to the binding on a commercially available collagen coated plate (Corning Biocoat) up to 1 µM of DS-SILY$_4$. In the ranges of 1 to 10 µM, DS-SILY$_4$ exhibited a negative binding trend on the Biocoat plate, likely resulting from preferential association of DS-SILY$_4$ with itself over the surface at higher concentrations. A similar downward binding trend was also seen for DS-SILY$_4$ on the collagen-coated plate in the 5 to 10 µM range. Differing collagen surface densities may account for these observed differences in binding behavior.

While DS is known to bind thrombin as well as heparin cofactor II in regulating fibrin formation (193-195), it has also been found to bind fibrinogen (196, 197), and therefore our designed molecule could possess binding capacity for both collagen and fibrinogen. Fibrinogen surfaces were exposed to ~400 µg/cm^2 fibrinogen, but despite this high coating density, the fibrinogen surfaces exhibited a low level of dose dependent DS-SILY$_4$ binding relative to collagen I and matrigel surfaces (Figure 3-15A). Therefore, our results show that a DS-based construct with a collagen I binding peptide, SILY, has greater binding capacity and affinity for collagens than fibrinogen. The results also support preferential binding to collagen I over other matrix proteins, as well as some small amount of binding to fibrinogen that could impart some anti-thrombotic activities. Preliminary investigation of inhibition of fibrin formation by decorin mimics *in vitro* did indicate preserved anti-thrombotic activity (data not shown), but these properties need more thorough exploration in future studies.

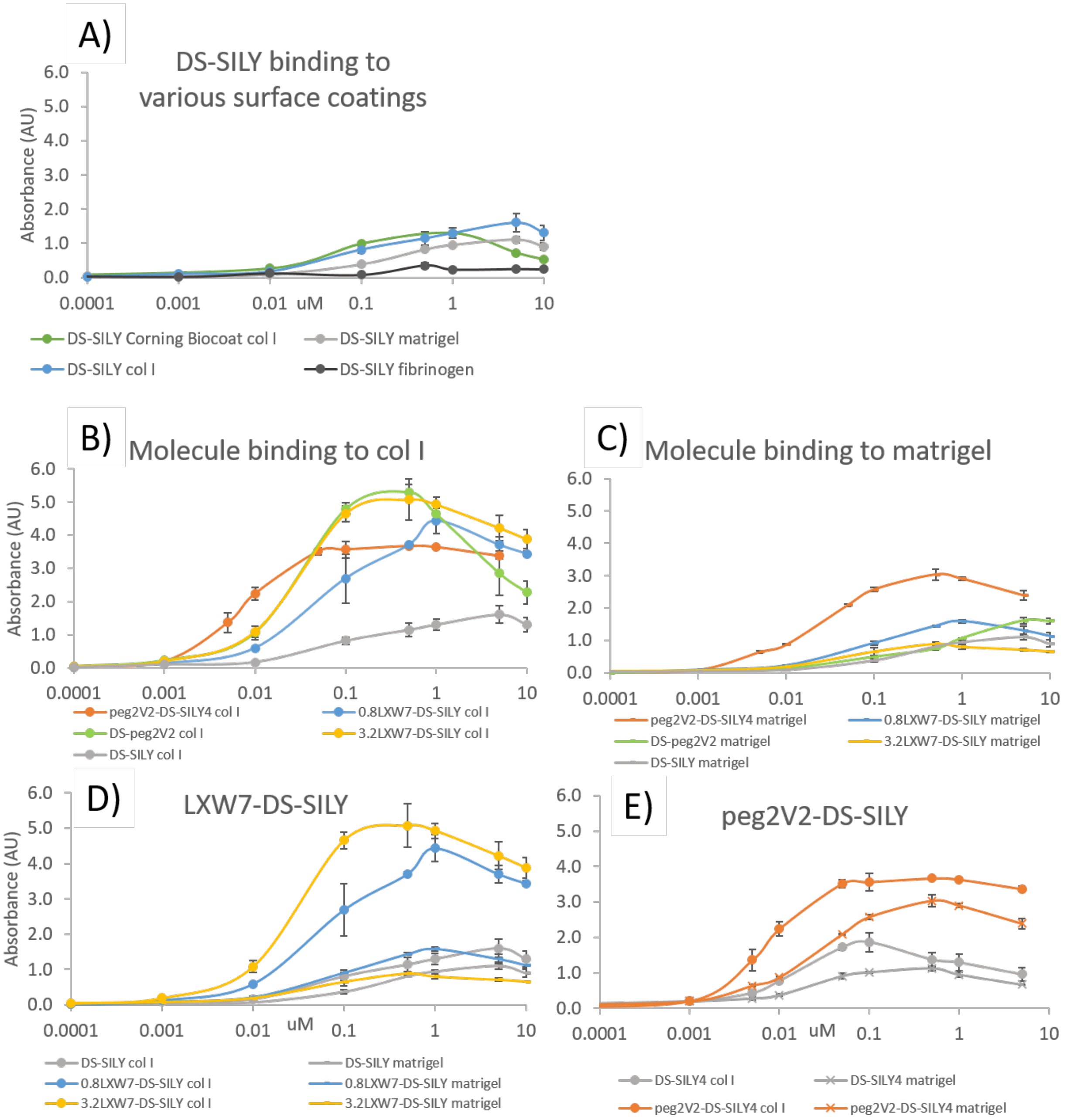

Figure 3-15. **Surface Binding of Molecules to Collagen I-, Matrigel-, and Fibrinogen-coated surfaces.**

DS-SILY has greater binding capacity for collagen I than matrigel surfaces and exhibits very low binding of fibrinogen surfaces (A). Conjugation of peg2V or LXW7 increases DS-SILY binding to both collagen I (B) and matrigel surfaces (C). Peg2V also exhibits intrinsic collagen I (B) and matrigel (C) binding properties even greater than SILY, but shows a significant drop in collagen binding at concentrations exceeding 0.5 µM. LXW7 conjugation improves LXW7-DS-SILY collagen I specificity over matrigel (D). Peg2V conjugation increases peg2V-DS-SILY binding to both collagen I and matrigel.

3.4.5.2 Peg2V Conjugation to DS-SILY4 Increases Collagen I and Matrigel Binding Capacity and Synergistically Strengthens Collagen I and Matrigel Binding Affinity

As seen in Figures 3-15B and 3-15C, peg2V conjugation to DS-SILY$_4$ increased binding to collagen I and matrigel. To determine whether this increase was caused by non-specific b inding due to greater peptide substitution or intrinsic collagen I affinity, we studied whether removing the known collagen-binding SILY peptide would still allow for dose-dependent collagen I binding. Figure 3-15B (green curve DS-(peg2V)$_2$) reveals that, when conjugated to DS, peg2V does have very high intrinsic collagen I affinity but appears to aggregate more readily at concentrations above 0.5 µM, represented by a significant drop in binding at high concentrations. In fact, between the concentrations of 0.05 to 1 µM, DS-(peg2V)$_2$ had the highest collagen I binding capacity of all the molecules studied (Figure 3-15B), although it was statistically similar to the 3.2LXW7-DS-SILY$_4$ variant. Interestingly, since DS-(peg2V)$_2$ exhibited higher collagen I binding capacity than DS-SILY$_4$, collagen may have more binding sites for peg2V than SILY. This is especially significant given that the addition of only 2 peg2V peptides produced greater binding than 4 SILY peptides, and noting that both molecules were synthesized with the same amount of EDC and assuming that biotinylated SILY produced a comparable signal to biotinylated peg2V. This suggests that the amounts of N-acylurea should be comparable and differences between the DS-SILY$_4$ and DS-(peg2V)$_2$ molecules could not be accounted for by EDC. However, one possible unaccounted variable is the use of biotinylated SILY versus biotinylated peg2V for detection of these two molecules. If, for example, biotinylated peg2V somehow produced an enhanced signal compared to biotinylated SILY, this would compromise any conclusions made comparing the surface-binding properties of these two molecules. Notably, Figure 3-15B also demonstrates that DS-(peg2V)$_2$ has a higher affinity for collagen I than DS-SILY$_4$, while their matrigel binding affinities were similar (Figure 3-15C). However, it appears that the combination of peg2V with SILY synergistically strengthens binding affinity to both collagen I and matrigel as (peg2V)$_2$-DS-SILY$_4$ demonstrated the highest collagen I and matrigel affinities with significantly greater binding at lower concentrations <0.05 µM. The data taken altogether suggests that peg2V exhibits specific collagen I binding even greater than SILY, but the simultaneous conjugation of both peptides increases collagen I and IV affinity and reduces molecular aggregation high concentrations.

3.4.5.3 LXW7 Conjugation to DS-SILY$_4$ Increases Total Collagen I Binding Capacity and Improves Collagen I Specificity over Collagen IV

As seen in Figures 3-15B and 3-15C, LXW7 conjugation to DS-SILY$_4$ also increased binding to collagen I and matrigel. Taking a different approach to investigating the effects of LXW7 on collagen binding, we compared variants with differing degrees of LXW7 substitution. 3.2LXW7-DS-SILY$_4$ had greater binding capacity than 0.8LXW7-DS-SILY$_4$ at all concentrations and both bound collagen I better than DS-SILY$_4$ alone, suggesting that the addition of LXW7 increased collagen I binding sites. From Figure 3-15B, addition of LXW7 also improved molecule affinity to collagen I since 3.2LXW7-DS-SILY4 had significantly greater affinity than 0.8LXW7-DS-SILY$_4$. Most notably, as seen in Figures 3-15C and 3-15D, a higher LXW7 substitution also improved collagen I specificity over matrigel since 3.2LXW7-DS-SILY$_4$ had higher collagen I binding but lower matrigel binding than 0.8LXW7-DS-SILY$_4$. It is possible that LXW7 does this by more specifically binding collagen I or that it imparts non-specific collagen I binding and simultaneously hinders matrigel binding by unknown mechanisms, but biotinylated DS-LXW7 variants (lacking SILY) were not synthesized to rule out non-specific binding.

3.4.5.4 Prolonged Room Temperature Incubation in 1% BSA Decreases Effective Molecule Concentrations and Reduces Specificity for Collagen I over Collagen IV

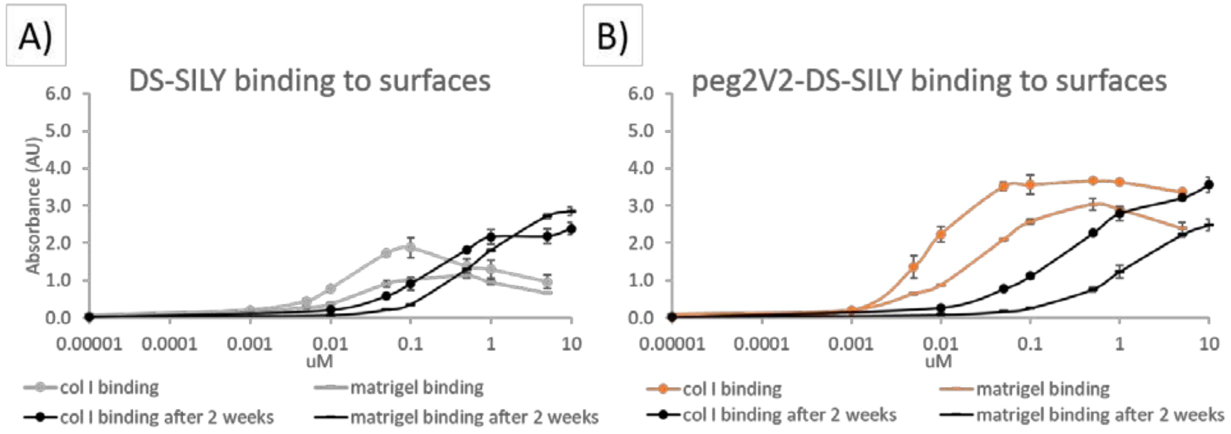

Figure 3-16. **Changes in Surface Binding after Molecule Incubation for 2 weeks in 1%BSA.**

After application to the wound bed, it is possible that slow hydrolytic degradation of the pro-angiogenic decorin mimics over several days could change binding properties and thereby cause increased likelihood of diffusing into systemic circulation. To study the hydrolytic deterioration of binding activity over time, we observed surface binding properties of DS-SILY$_4$ and (peg2V)$_2$-DS-SILY$_4$ after 2 weeks in 1% BSA at room temperature (Figure 3-16 A & B). This experimental design assumes that differences in binding properties after molecules were incubated for a prolonged period in 1% BSA were due to hydrolytic degradation of the molecules rather than interactions with BSA. It was presumed that similar interactions with BSA would occur when molecules were freshly dissolved (~1 hour in 1% BSA) and when they were in 1% BSA solution for the 2 week period. From Figures 3-16 A & B, it is clear that both the collagen I and matrigel binding curves shifted after the 2 week incubation such that higher concentrations are needed to achieve the same binding, reflected by lower molecule affinities. However while total binding capacity of DS-SILY$_4$ to collagen I is maintained after partial hydrolysis, the partially degraded DS-SILY$_4$ had increased total matrigel binding capacity at concentrations > 0.5 µM. This observation suggests that hydrolytic degradation and/or interactions with BSA over the 2 weeks not only decrease effective molecule concentration, but also alters the total number of DS-SILY$_4$ binding sites for matrigel. In contrast for (peg2V)$_2$-DS-SILY$_4$, the molecule maintains higher binding capacity for collagen I than matrigel over the full concentration spectrum and total binding capacities for collagen I and matrigel are unchanged. Taken together with the observation that peg2V renders intrinsic collagen I and matrigel binding, the addition of peg2V to DS-SILY$_4$ provides additional collagen binding capacity that maintains collagen I specificity over matrigel after the 2 week incubation period. However we are unable to make any conclusions about peg2V degradation. The overall observed concentration shifts suggest that the effective molecule concentration has decreased after the 2 week incubation, which could be caused by degradation of the full molecule or hydrolysis of the collagen-binding SILY peptide. Although more pronounced molecule aggregation after the 2 week incubation may be a confounding factor, agglomeration alone cannot account for the changes in total matrigel binding capacity observed for DS-SILY$_4$.

3.4.6 Binding and Activation of VEGFR2

3.4.6.1 Characterization of V Binding Affinity to VEGFR2

As a preliminary assessment of the angiogenic potential of our engineered therapies, we first assessed the ability of our modified VEGF-mimicking peptide, V, to bind VEGFR2 using biolayer interferometry on an OCTET instrument (Pall ForteBio). The steps for biosensor preparation are diagrammed in Figure 3-17A and a sample binding curve depicted in Figure 3-17B. We observed concentration-dependent binding of VEGF and V peptide to immobilized VEGFR2 (Figure 3-17 C & D) with binding curves resembling heterogeneous binding of the analytes to the receptor. In our initial testing, we found that similar binding curves with greater signals could also be achieved using 0.1% BSA as a blocking agent, but the blocking was not sufficient to prevent non-specific binding. Use of 1% powdered milk dissolved in PBS was required to remove non-specific binding background. The resulting dissociation constants, K_D, were found to be ~0.146 nM and ~80.1 uM for VEGF and VEGF-mimicking peptide V, respectively. The measured K_D for VEGF, an average from 6 curves, is comparable that reported in literature of 410 pM (198). For V peptide, the K_D reported is measured as an average of the 3 lowest concentration curves, since the higher concentration curves did not match the modeled binding lines shown in red (Figure 3-17D) and exhibited a heterogeneous binding curve (Figure 3-17B). For VEGF, k_{on} was $3.22*10^6$ M^{-1} s^{-1} and k_{off} was $3.86*10^{-4}$ s^{-1}. The corresponding k_{on} for VEGF-mimicking peptide was 2.48 M^{-1} s^{-1} and k_{off} was $1.75*10^{-3}$ s^{-1}. The significantly higher measured K_D for the VEGF-mimicking peptide indicates that its VEGFR2 binding affinity is multiple orders of magnitude lower than native VEGF and thus significantly higher peptide concentrations would be needed to exert the same binding responses. As k_{on} is also much larger but k_{off} is smaller for VEGF, it also appears that VEGF binds quicker and dissociates slower than the VEGF-mimicking peptide. These binding experiments clearly show measurable differences in the binding affinity, association, and dissociation kinetics of peptides compared to the full growth factor. It follows that VEGFR2 activation dynamics likely differ significantly as well.

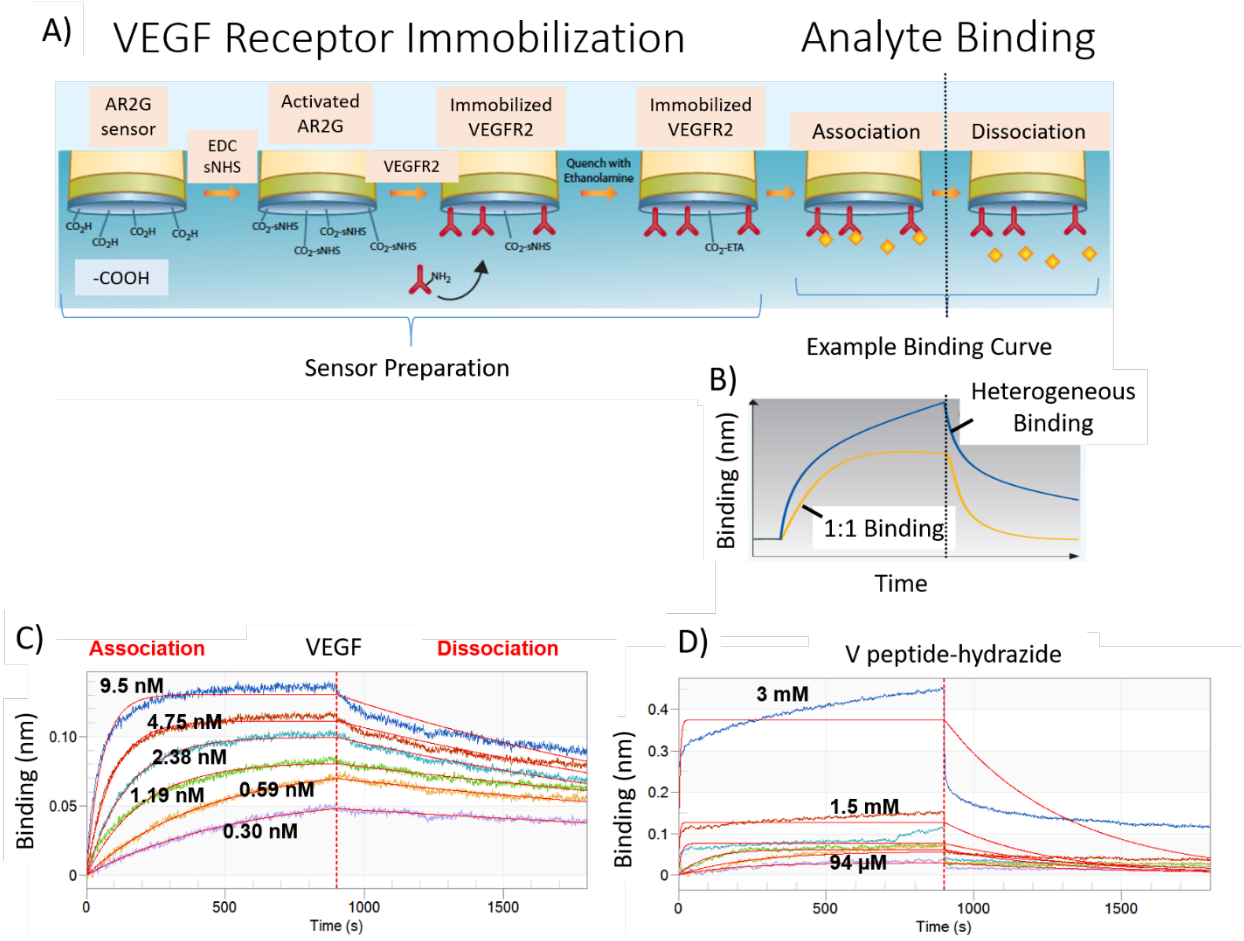

Figure 3-17. **OCTET Interferometry Characterization of VEGF-mimicking Peptide Binding Affinity to Immobilized VEGFR2.**

Subfigure A is modified from ForteBio Technical note 26. The dissociation constants, K_D, were found to be ~0.146 nM and 80.1 µM for VEGF and VEGF-mimicking peptide, respectively. V has a much lower affinity for VEGFR2 than native VEGF.

3.4.6.2 Characterization of VEGFR2 Activation due to Pro-Angiogenic Decorin Mimics

Prolonged VEGF stimulation elicits a quick increase and rapid decline of VEGFR2 phosphorylation over 30 minutes (Figure 3-18A). After 5 minute treatments, HUVECs showed a synergistic response to VEGF with peptides QK or V and an even greater potentiation with DSV4 (Figure 3-18B). Peptides or DSV4 alone did not show significant increases in % VEGFR2 phosphorylation after 5 minute exposures to treatments (Figure 3-18B). Increasing treatment time to 30 minutes increased %VEGFR2 phosphorylation marginally and very slowly over time for both peptides QK and V and all DS-based constructs (Figures 3-18 C & D). It therefore appeared that binding kinetics of free peptides and DS molecules differed from VEGF, an observation that is supported by the OCTET binding studies.

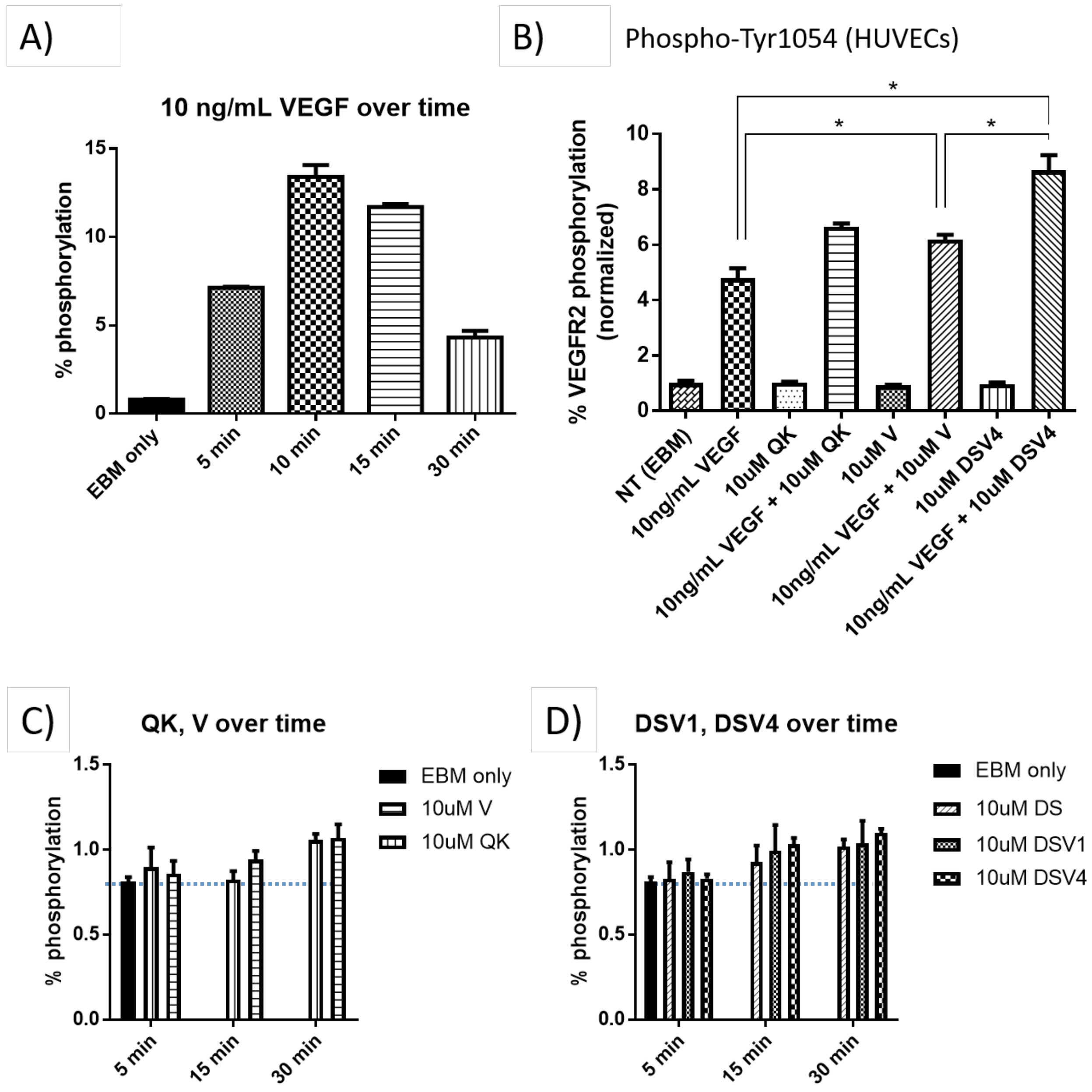

Figure 3-18. **Dynamics of VEGF activation in HUVECs in Response to Peptides and DS-based constructs.**

Subfigure A depicts the rapid increase and subsequent decrease in %VEGFR2 activation within 30 minutes in response to constant stimulation by 10 ng/mL VEGF, while peptides and DS-based constructs produce a very slow low amplitude increase in % phosphorylation over 30 minutes. Subfigure B shows %VEGFR2 activation after treating HUVECs for 5 minutes with VEGF or DSV4 showing significant synergism. Differences in %VEGFR2 activation from QK synergism compared with V synergism are not statistically significant. Sample n = 3, with measured values presented as mean ± standard deviation. Bracketed pairs with * denote statistically significant differences in treatment groups.

3.5 *Conclusion*

In completion of the aims of this chapter, we described the design, development, and characterization of pro-angiogenic decorin mimics. We developed synthetic methods for peptide-hydrazides and pro-angiogenic decorin mimics, as well as non-destructive quantification methods to determine degree of peptide substitution. In special consideration for the VEGF-mimicking peptides, we ensured that alpha-helical secondary structure was maintained before and after conjugation. We also ensured that the VEGF-mimicking peptide could bind VEGFR2 in a concentration dependent manner and characterized its binding affinity, association, and dissociation rates compared to native VEGF. Moreover, we explored how the EDC synthetic chemistry may produce unintended biological effects, and provided preliminary results for an alternative DMTMM chemistry. Next, ECM binding properties with special interest in their ability to target collagen I and matrigel were characterized. These binding properties are pertinent to the bioactivity experiments explored in chapter 4, where surface-bound molecules are assessed for angiogenic activity. Finally, we also briefly explored VEGFR2 activation.

4. ASSESSMENT OF IN VITRO AND IN VIVO ANGIOGENESIS OF PRO-ANGIOGENIC DECORIN MIMICS

4.1 *Preface*

Having discussed in detail the developmental synthesis and characterization of pro-angiogenic decorin mimics along with some preliminary exploration of the molecule's effects on receptor activation in Chapter 3, Chapter 4 focuses on assessing *in vitro* and *in vivo* angiogenic bioactivity, with and without VEGF, of two variants of pro-angiogenic decorin mimics ($(peg2V)_3$-DS-$SILY_4$ and 4LXW7-DS-$SILY_4$). We evaluate 1) endothelial cell (EC) proliferation and migration, 2) two-dimensional EC tubule formation on matrigel embedded with pro-angiogenic decorin mimics, 3) neovascularization from a chick chorioallantoic membrane (CAM assay) growing into a collagen scaffold embedded with pro-angiogenic decorin mimics, reflecting the ability of the scaffold to integrate into existing vasculature, and 4) EC monolayer permeability. Refer back to Figure 3-2 for the overall breakdown of Chapter 3 and Chapter 4. In addition to discussing the angiogenic activity of the two variants, our biological results highlight the importance of peptide presentation (soluble versus bound and varying surface densities) in affecting bioactivity.

4.2 *Introduction*

4.2.1 Special Considerations for Preserving Pro-angiogenic Properties of QK

In the introduction to Chapter 3, numerous examples of recent studies were provided showing that surface-bound QK could exert an angiogenic response, often even greater than the free QK peptide alone. In solution, free QK is always reported to exert an angiogenic response. However, it is worth noting that two studies have also revealed that QK presentation in an immobilized form, specifically at high densities (166, 199), can also elicit anti-angiogenic effects, perhaps due to the complexities of the VEGF signaling pathway. VEGF receptors become activated by tyrosine kinase phosphorylation after receptor dimerization (200, 201). As VEGF molecules preferentially form homodimers, each VEGF within a homodimer binding a receptor brings two VEGF receptors into close proximity of each other to allow phosphorylation and activation. The most compelling explanation for the anti-angiogenic property observed in some studies of immobilized QK is a proposed phenomenon *Koepsel et al.* has termed “receptor pinning” by which a given surface density of QK occupies VEGF receptors in a manner that prevents dimerization; *Koepsel et al.* also speculates that very short linkers from QK to the substrate may exacerbate this “receptor pinning” because short linkers cause the occupied VEGF receptors to become less mobile (199). These particular studies demonstrate the importance of characterizing our system and carefully designing moderate surface densities. The proposed mechanism of receptor pinning also suggests that it is advantageous to use longer peptide linkers for pro-angiogenic applications.

4.2.2 Special Considerations for Preserving Pro-angiogenic Properties of LXW7

LXW7 peptide was originally developed as a targeting ligand to inhibit αvβ3 integrin and deliver therapies to cancer cells overexpressing this integrin (202). In these studies, free LXW7 acts as a competitive inhibitor of αvβ3 integrin to block cell binding and angiogenesis (203, 204) and is proposed to act by down-regulating VEGF and its associated pathways (175, 176). It follows then that LXW7 is anti-angiogenic in soluble presentation and needs to be surface-bound to be pro-angiogenic.

4.3 *Materials and Methods*

4.3.1 Cell Culture

Human Dermal Microvascular Endothelial Cells (HMVEC, Lonza CC-2543) were expanded according to the manufacturers’ protocol in EGM2-MV media, and passaged at 70-90% confluence. Cells were cryopreserved in 80% media, 10% sterile DMSO, and 10% FBS. For experiments, HMVECs were used between passages 6 and 8, and maintained at 37°C and 5% CO_2.

4.3.2 Endothelial Proliferation in Response to Soluble Molecules

HMVECs were seeded at 2000 cells per well in a CellBind® 96-well plate (Corning) using complete EGM-2MV media. After 24 hours, media was replaced with EBM (serum and growth-factor free) for 4 hours and then replaced with treatments dissolved in EGM-2MV media lacking VEGF or lacking both FGF and VEGF. After 24 or 72 hours, proliferation was evaluated by an endpoint MTS assay (CellTiter 96® AQueous One Solution, Promega), by adding 10 µL of 3-

(4,5-dimethylthiazol-2-yl)-5-(3-carboxymethoxyphenyl)-2-(4-sulphophenyl)-2H-tetrazolium (MTS) inner salt reagent to each well, incubating for 4 hours at 37C, and then measuring absorbance at 490 nm. A standard curve to determine appropriate cell seeding numbers and correlation of initial cell number to metabolic activity was also performed.

4.3.3 Endothelial Attachment and Proliferation in Response to Surface-bound Molecules

50 µL treatments dissolved in 1% BSA in PBS were added to a Biocoat Collagen I 96-well plate (Corning) and incubated for 30 minutes at 37C before washing 3 times with PBS to remove unbound treatment. HMVECs were then seeded in either EGM2-MV media or EGM2-MV media without VEGF at a density of 1500 cells per well (low cell density) or 8000 cells per well (high cell density). To evaluate initial attachment, media was aspirated 6 hours after seeding and exchanged with alamarBlue® cell viability reagent (1:10, 110 µL/well, Molecular Probes) and incubated for 2.5 hours at 37°C according to the manufacturers' protocol. 100 µL from each well was pipetted into a new plate and assayed for fluorescence at 560 nm excitation and 590 nm emission. Remaining reagent was aspirated and replaced with fresh media and the alamarBlue® viability assay was performed every 2 days thereafter for 1 week. To control for initial differences in HMVEC attachment, proliferation data is presented as the alamarBlue® fluorescence signal normalized to the signal at 8 hours.

4.3.4 Endothelial Migration

ORIS 96-well plates (Platypus technologies) were coated with 50 µg/mL human fibrillar collagen I (Chronolog) overnight at 4°C. Wells were rinsed 3x with PBS and left to air dry under UV for 1 hour before inserting ORIS silicone stoppers and seeding HMVECs at 8000 cells per well around the stoppers. Cells were allowed to grow to confluence for 48 hours before a 30 minute incubation with 4 µg/mL mitomycin C (Sigma) to halt proliferation. After removal of ORIS stoppers, cells and the collagen-coated surface were incubated with 10 µM of DS-SILY constructs dissolved in EGM-2MV without VEGF for 15 minutes. The treatments were removed and replaced with growth media (EGM-2MV without VEGF) for 48 hours before staining with 10 µM CellTracker Green (molecular probes) and fluorescent imaging on a Keyence BZ-X700 microscope. Fluorescent images were quantified by pixel area analysis on ImageJ.

4.3.5 Endothelial Tubulogenesis

Reduced growth factor Matrigel (Corning) was mixed with treatments on ice to obtain the final desired concentrations (10, 20, and 30 µM) within the gel and distributed to Ibidi angiogenesis µ-slides at 10 µL per well to polymerize at 37°C for 30 minutes. HMVECs were seeded at 7500 cells per well in reduced growth factor media (EGM-2MV lacking FGF, VEGF, and IGF supplements). After 8 hours of incubation, cells were stained with 2 µM calcein AM and imaged on a Keyence BZ-X700 microscope. Image analysis tubule quantification was performed by AngioQuant software with a prune factor of 25 to remove artefacts from cellular debris (205).

4.3.6 *Ex Ovo* Chick Chorioallantoic Membrane (CAM) Assay

The *ex ovo* CAM assay and vessel quantification was performed similarly to previously established protocols for treatments eluting from alginate gels (206-208) and for *de novo* vessels invading collagen gels (209, 210). Fertilized Hyline eggs obtained from the Avian Facility at UC Davis were incubated at 37°C for 72 hours with 6 rotations per day at 80% humidity in a Grumbach egg incubator. On day 3, eggs were cracked open into disinfected weighboats (VWR) and covered with lids from square petri dishes (Fisher), and the embryos developed over a week in the incubator. On day 10, treatments encapsulated in collagen I gels were gently placed on the developing CAM. For experiments involving treatments freely eluting from the collagen gels, 100 µL of gel was polymerized in a 10 mm diameter rubber mold against a sterilized glass slide, and 1 treatment gel and 1 control gel was placed per CAM. Gels were imaged using a 12 megapixel camera. The number of vessels in a 2 mm radius immediately surrounding the gel was manually counted in imageJ immediately after placement and 24 hours later to determine changes surrounding vessels. The change in vessels over 24 hours for treatment gels were normalized to the respective change in the control gel on the same developing embryo. For experiments studying vascular invasion into collagen gels, 30 µL collagen I gels with an embedded 3 mm x 3 mm nylon mesh (Fisher) were used. 4-5 gels were placed on each CAM, with 2-3 treatment gels of the same type and 2 blank gels as internal controls to correct for embryo variability. In some embryos, the nylon meshes were dyed to improve visualization of the mesh and vessels growing into the gel. Large (4 cm x 10 cm) nylon meshes were dyed by reacting in 226 mL of a 77 mM acetic acid (Sigma) solution with 10 drops of green food coloring

(McCormick) or 250 µL of 3 mg/mL Evans blue (Alfa Aesar) at 121°C for 15 minutes in an autoclave, and then cut to 3 mm x 3 mm squares for embedding. Gels were imaged daily through a Dino-Eye AM7025X camera installed on a stereomicroscope; for images more than 2 days after gel implantation, 0.25 mL PBS was pipetted on top of gels to help visualize vessels. On day 16, 0.1mL of 1mg/mL RITC-dextran (70 kDa, Sigma) or Evans blue was injected into the CAM vasculature using a 30G needle, and the membrane was cut away from the embryo and placed in a petri dish for brightfield and fluorescent imaging. To quantify vascularity within the gel between 72-96 hours after gel placement, two independent observers scored each gel for the proportion of grids within the mesh that showed positive vessel growth, as described in *Zijlstra et al.* (210).

4.3.7 Endothelial Monolayer Permeability

Using EGM2-MV media lacking VEGF, HMVECs were seeded onto 3 µm pore 24-well transwell inserts (Corning) at 10,000 cells per insert. The following day, an additional 50,000 cells were seeded to each insert and allowed to grow for another 24 hours. Media was then removed and replaced with 0.5 mL media to the bottom well and 0.1 mL of treatment media to the insert for 10 minutes. Treatment was removed and 0.3 mL of 1mg/mL RITC-dextran in media was then added to each transwell insert and allowed to permeate for 30 minutes. Sample permeate was then assayed on a SpectraMax M5 plate reader for fluorescence (ex: 570 nm; em: 590 nm). RITC-dextran solutions and sample permeates were then aspirated and replaced with another 0.1mL of treatment media in the transwell insert and 0.5mL media in the bottom chamber. This procedure was repeated daily over 4 days. Treatments were also compared to inserts with cells removed by rubbing away with a pipette tip to determine the barrier efficacy of the monolayer and the degree of increased permeability.

4.3.8 Statistical Analysis

All quantitative data is presented as mean ± standard deviation, and statistical significance was evaluated by ordinary one-way ANOVA using post-hoc Dunnett's or Tukey's tests for multiple comparisons with values $p < 0.05$ denoted as significant.

4.4 *Results and Discussion*

4.4.1 HMVECs Attachment to Surface-bound Molecules

4.4.1.1 Peg2V Conjugation to DS-SILY$_4$ Decreases Cell Attachment

Microvascular endothelial cell adhesion to surface-bound molecules was studied for its relevance to endothelial recruitment in the wound healing process. Figure 4-1 demonstrates that at low cell densities, both 1 µM and 10 µM DS-SILY$_4$ surface treatments caused a slight 7% decrease in HMVEC attachment compared to a BSA blocked collagen surface (untreated control), although the decrease was only statistically significant at 10 µM (asterisks indicate treatments that were statistically different from DS-SILY$_4$ control). This was a significant finding since our lab has not previously investigated the effects of decorin mimic-coated collagen surfaces on cell attachment. Since DS-SILY$_4$ binds and masks collagen fibrils (116, 191), decreased adhesion is likely due to a decrease in exposed collagen and therefore reduced cell adhesion sites. Surprisingly, both 1 µM and 10 µM (peg2V)$_3$-DS-SILY$_4$ caused an even greater 15% decrease in HMVEC attachment compared to DS-SILY$_4$ alone (Figure 4-1). This additional decrease could be attributed to increased surface concentrations of (peg2V)$_3$-DS-SILY$_4$ due to higher surface binding discovered through the binding experiments (Figure 3-14B), thereby masking the underlying collagen more effectively and further decreasing adhesion sites for cells. Alternatively, it is possible that the conjugated peg2V peptide directly prevents cell attachment by unknown mechanisms. Although soluble QK has been shown to improve endothelial proliferation in numerous studies (159, 160, 163, 166), its effects on endothelial attachment have not been explicitly studied. *Wang et al.'s* study shows no significant effects of matrix-bound QK on endothelial adhesion (162) and *Koepsel et al.*'s study highlights one instance where immobilized QK exhibited anti-angiogenic effects and specifically decreased endothelial attachment, as it had no effects on fibroblast adhesion (199). Further adhesion studies of other cell types lacking significant levels of VEGF receptors are necessary to determine whether our observations result from VEGF receptor interactions or simply due to reduced exposed collagen.

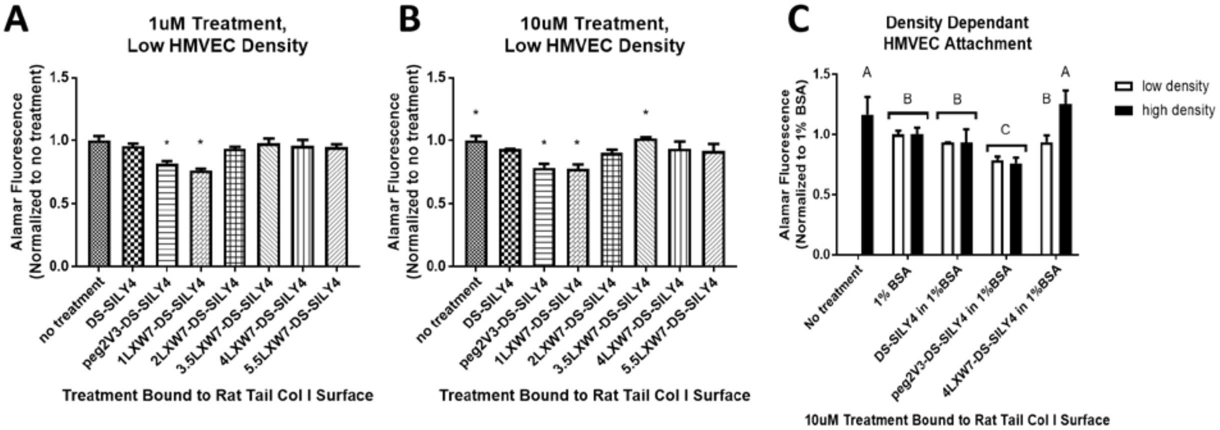

Figure 4-1. **HMVEC Attachment to Surface-bound Molecules with Varied Surface Treatment Concentration (A & B) and Varied Cell Seeding Density (C).**

HMVECs were seeded at a low density of ~4500 cells/cm^2 (optimal for proliferative assays) on collagen I surfaces treated with either 1 uM or 10 uM molecules in 1% BSA, allowed to attach for 6 hours, and then metabolic activity was assessed by AlamarBlue activity (n = 3). The responses with 1 uM and 10 uM surface treatments were comparable, which was to be expected due to approximate saturation of the surface at 1 uM. In a follow-up study (subfigure C), cells were seeded at a nearly confluent, > 6-fold higher density of ~28500 cells/cm^2 (optimal for migration assays) on collagen I surfaces treated with 10 uM molecules in 1% BSA and similarly assessed for attachment with AlamarBlue ($n \geq 8$). * indicates a statistically significant difference compared to DS-SILY$_4$ control. Bars labeled with the same letter (A, B, or C) are statistically equivalent to each other.

4.4.1.2 High LXW7 substitution to DS-SILY$_4$ increases cell adhesion especially at high cell seeding densities, but low LXW7 substitution decreases cell adhesion

To determine the effects of LXW7 conjugation on cell adhesion, multiple variants with varying degrees of LXW7 substitution were investigated. A low LXW7 substitution of 1 caused a significant 18% decrease in cell adhesion at both 1 µM and 10 µM concentrations similar to the peg2V addition; however, increasing LXW7 substitution caused a trending increase in HMVEC attachment, with the greatest positive effect at 3.5 LXW7 (Figure 4-1 A and B). At both 1 µM and 10 µM, it appears that a threshold substitution degree of at least 2 LXW7 is required to prevent negative effects on attachment. Although cell adhesion was similar between the 1 and 10 µM concentrations for all treatments, a 10 µM concentration was required to observe that a moderate degree of substitution between 3 and 4 provides an optimal attachment level significantly greater than DS-SILY$_4$ by 8% and comparable to attachment to an untreated collagen I surface blocked with 1% BSA (Figure 4-1B). This phenomenon could be explained by significantly higher molecule binding to the collagen surface and masking exposed collagen or by repulsive effects from DS' negative charge. We also observed that conjugation of 1 LXW7 leads to lower cell attachment that could be compensated by increased LXW7 substitution that either directly facilitated increased cell attachment or improved cell survival by decreasing apoptosis. Given LXW7's role facilitating cell adhesion through integrin-binding, it was surprising that increased LXW7 substitution beyond 3.5 did not significantly increase cell attachment when cells were seeded sparsely for proliferation assays (~4500 cells/cm^2 as recommended for HMVEC expansion by Lonza), since other groups have observed increased endothelial attachment to LXW7-coated surfaces (149). The discrepancy in our observations might be attributed to the much lower surface densities of LXW7 in our studies due to low LXW7 substitution on DS-SILY. Furthermore, cell attachment is assessed after a relatively long period of 6 hours, whereas studies by other groups assessed attachment to LXW7 surfaces after < 2 hours incubation (149). It is therefore possible that differences in cell attachment that can be observed at earlier time points, indicating the speed of attachment, are not captured in our study. Nevertheless, at our relatively low LXW7 surface densities, increasing the cell seeding density more than 6 fold (~28,500 cells/cm^2) to confluence was able to reveal the expected increases in cell binding in response to 4LXW7-DS-SILY$_4$ with restored HMVEC attachment comparable to an unblocked collagen I surface (Figure 4-1C). Since the cell seeding density needed to be confluent to see increased cell attachment on our surface, the LXW7-induced increases in cell attachment and/or survival must be dependent on direct cell-cell interactions, although further investigation is needed to elucidate the mechanisms by which cell-cell communication in combination with integrin signaling improved cell survival/attachment.

4.4.2 HMVEC Proliferation in Response to Soluble Molecules and Surface-bound Molecules

4.4.2.1 Assay Selection for Assessment of Cell Proliferation

Although both the MTS and alamarBlue assays are indicative of total metabolic activity rather than actual cell number, direct analysis of discrepancies between metabolic versus DNA assays have suggested that metabolic assays can be appropriate for high throughput analysis, taking into account their limitations of potentially overestimating proliferation compared to DNA quantification (211). One of the advantages to using the non-endpoint metabolic assay alamarBlue for the study of cell response to surface-bound molecules was the ability to follow multiple samples overtime while reducing the overall amount of treatment needed. This was especially beneficial in our studies since our treatments and peptides were synthesized in small batches in our lab. In the experiments studying response to soluble molecules, the alamarBlue was not suitable because the solution needed to be replenished after every time point, thus requiring a greater overall amount of treatment. Proliferation tests for soluble molecules were therefore assessed with MTS and confirmed by direct Cyquant DNA analysis (data not shown).

4.4.2.2 Short PEG linker in peg2V peptide is important in maintaining proliferative bioactivity after conjugation.

Initial investigation of proliferative bioactivity using an endpoint MTS metabolic assay revealed a trending increase in HMVEC proliferation in response to constant 24 hour and 72 hour stimulation by soluble DS(peg2V)$_3$ and (peg2V)$_3$-DS-SILY$_4$ but not DSV$_3$ when compared to DS and DS-SILY$_4$ alone (Figure 4-2). These same trends were seen in media lacking both VEGF and FGF. First, the experiment demonstrated that conjugated peg2V peptide was responsible for the observed increased proliferation, since 10 µM soluble (peg2V)$_3$-DS-SILY$_4$ also significantly increased proliferation compared to 10 µM soluble DS-SILY$_4$. Next, the trending increase in bioactivity for DS(peg2V)$_3$ compared to DSV$_3$ suggests that the longer spacer between the active QK sequence and the DS backbone improved the proliferative response, perhaps by allowing better access for peptide binding to the VEGF receptor or by better conserving the α-helical secondary structure. However, any differences in the secondary structure are very slight, as demonstrated by our CD analysis (Figure 3-9 A and E). The slightly increased bioactivity for (peg2V)$_3$-DS-SILY$_4$ over DS(peg2V)$_3$ may be accounted for by higher local concentrations around the cell when bound to secreted collagen and other matrix molecules (assessed in binding experiments Figure 3-14) and could therefore exert a more potent proliferative response. Since the longer peptide spacer was found to be important for improving conjugated VEGF-mimicking peptide bioactivity, all further studies of bioactivity exclusively used peg2V rather than V peptides. The LXW7-conjugated variants were not tested in the soluble proliferation assay, since LXW7-DS-SILY$_4$ variants required surface binding to enact proliferative bioactivity through integrin-binding.

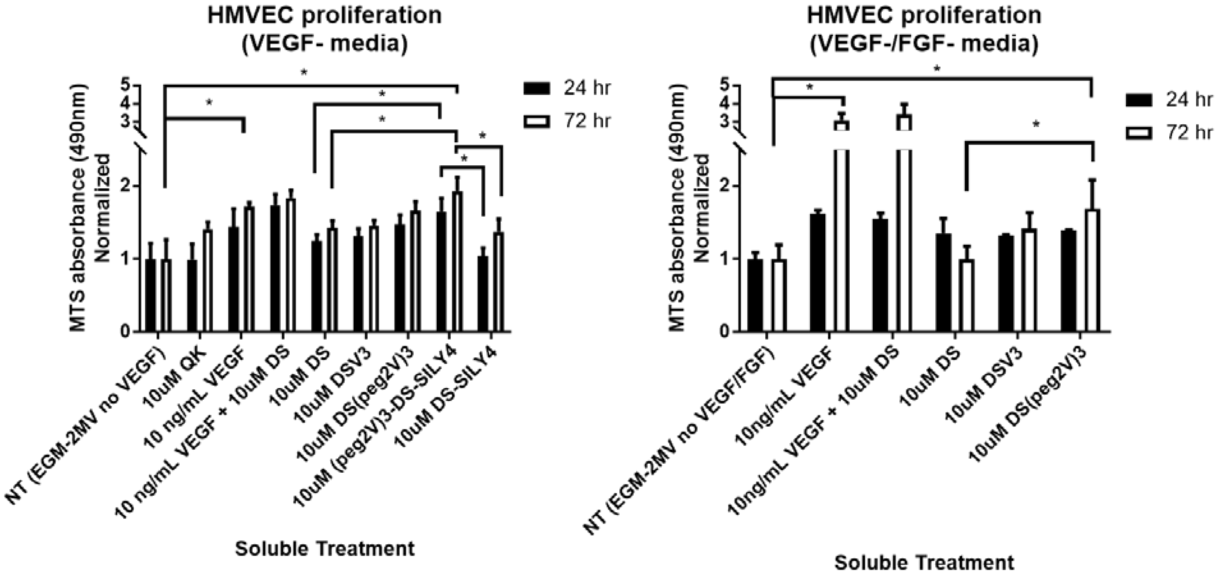

Figure 4-2. **HMVEC Proliferation in Response to Soluble VEGF-mimicking Treatments.**

HMVECs showed trending increases in proliferation after 72 hours of treatment with soluble VEGF-mimicking treatments DSV_3, $DS(peg2V)_3$, and $(peg2V)_3$-DS-$SILY_4$. Since $DS(peg2V)_3$ was more effective than DSV_3, the extra PEG linker is important for preserving bioactivity of the VEGF-mimicking peptide after conjugation to DS. Sample $n \geq 4$, with measurements representing mean ± standard deviation. * denotes statistically significant differences between bracketed groups. Note that not all groups are explicitly compared.

4.4.2.3 Surface-bound decorin mimics significantly enhance endothelial proliferation

Both soluble and bound forms of molecules would be present in a dynamic equilibrium in this initial experimental design and the two forms may produce differing effects, and thus we sought to investigate the effects of bound molecules alone. Furthermore, the bioactivity of a collagen-bound form would more directly reflect the application of a targeted pro-angiogenic therapy in a chronic wound. To investigate the effects of surface-bound molecules, collagen surfaces were first incubated with treatments to bind and then washed thoroughly to remove any unbound molecules before seeding and following cell growth every other day for a week with media replenished every other day. To control for differences in initial cell number due to surface effects on cell attachment, signals were normalized to the signal 8 hours after seeding.

As observed by *Scott et al. (190)* for a similar but oxidized DS-$SILY_{20}$ molecule, DS-$SILY_4$ surface treatments significantly improve endothelial proliferation compared to untreated collagen alone. The effects of 1 µM DS-$SILY_4$ were only statistically significant over no treatment when compared in media lacking VEGF, but 10 µM DS-$SILY_4$ significantly improved proliferation in media with and without VEGF (Figure 4-3). The effects of 1 and 10 µM concentrations were very comparable, because although 10 µM DS-SILY$_4$ improved proliferation over 1 µM by day 6 in media with VEGF, 1 µM DS-SILY$_4$ was equally as effective as 10uM during the first 4 days of growth. The relative similarity between the 1 and 10 µM DS-SILY$_4$ concentrations could be expected given the apparently saturated collagen I-binding plateau found in the surface binding experiments (Figure 3-14).

4.4.2.4 Peg2V conjugated to DS-SILY$_4$ potentiates VEGF-mediated proliferation

A peg2V conjugated DS-SILY$_4$ variant was investigated in 2 concentrations to observe proliferative effects. In media lacking VEGF, (peg2V)$_3$-DS-SILY$_4$ did not have any significant proliferative effects, although the higher 10 µM concentration showed a trending improvement in proliferation (Figures 4-3 A & B). In contrast, (peg2V)$_3$-DS-SILY$_4$ surface treatment significantly improved proliferation over DS-SILY with VEGF supplementation, indicating an apparent synergistic effect of the conjugated peg2V with VEGF (Figures 4-3 C & D). At 1 µM, (peg2V)$_3$-DS-SILY$_4$ surface treatment was as effective as the 10 µM treatment, both resulting in ~9-fold increase after 144 hours of growth; however, the 1 µM more effectively potentiated VEGF activity compared to 10 µM, providing a 27% increase in proliferation over the 1 µM DS-SILY$_4$ control versus an 18% increase over the 10 µM DS-SILY$_4$ control. In summary, our results show that (peg2V)$_3$-DS-SILY$_4$ were not effective on their own, but significantly potentiated VEGF activity.

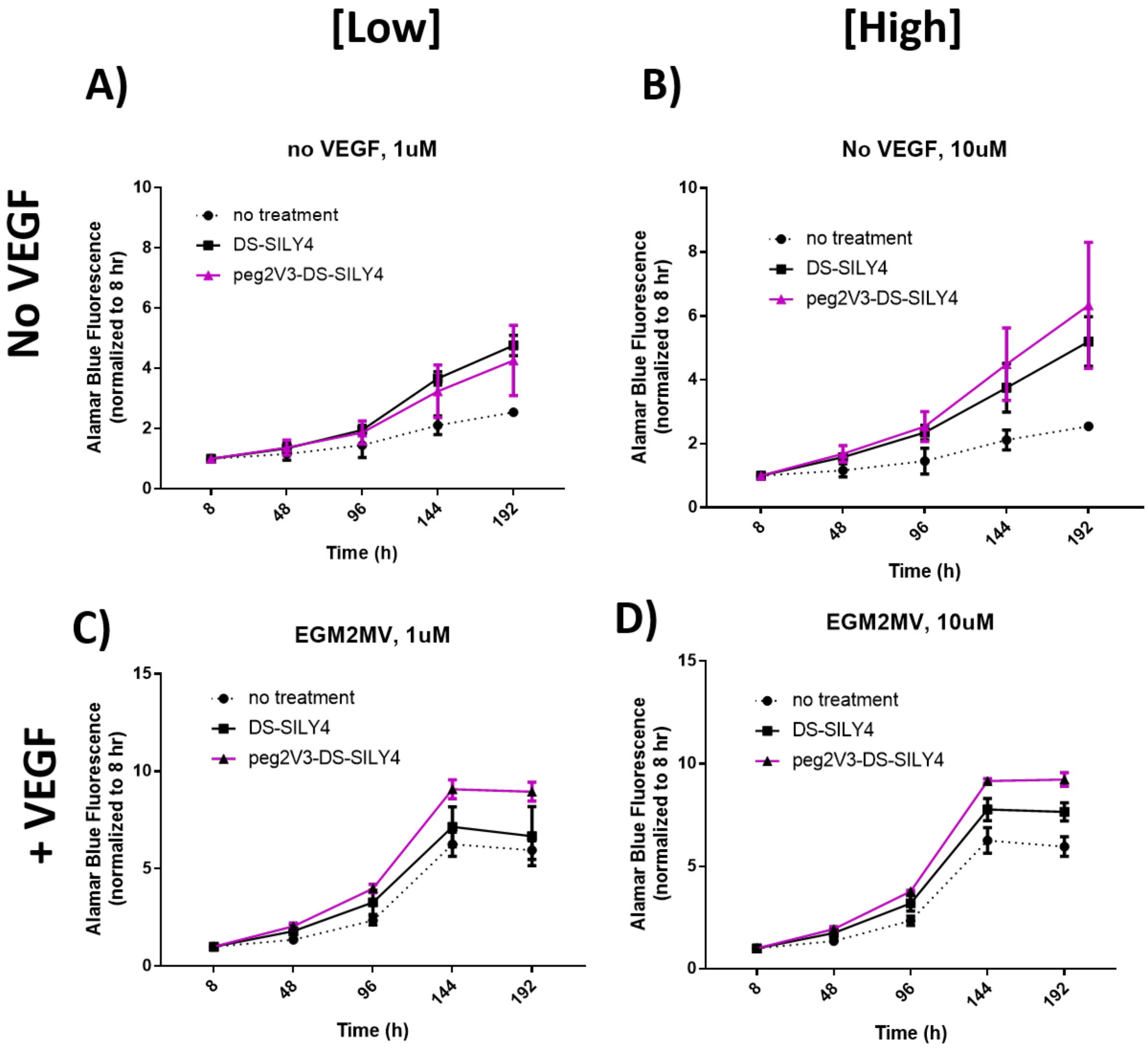

Figure 4-3. **HMVEC Proliferation in Response to Surface-bound VEGF-mimicking (peg2V)$_3$-DS-SILY$_4$.**

DS-SILY$_4$ alone produces a proliferative increase in media with and without VEGF. Although conjugated peg2V on (peg2V)$_3$-DS-SILY$_4$ does not provide additional proliferative activity in media lacking VEGF, this pro-angiogenic decorin mimic shows greater proliferation over DS-SILY$_4$ in the presence of VEGF supplementation, suggesting that peg2V exhibits synergistic proliferation with VEGF.

4.4.2.5 Surface densities of LXW7 conjugated to DS-SILY$_4$ impact the ability of LXW7-DS-SILY$_4$ variants to enhance endothelial proliferation, suggestive of optimal bioactivity dependent on integrin clustering

Multiple LXW7-DS-SILY$_4$ variants with differing degrees of substitution were tested to determine the effect of LXW7 density on endothelial proliferation, since varying RGD surface densities and patterning are known to affect integrin binding conformation and activation (212)and can thereby have significant effects on subsequent VEGF receptor clustering and activation. Figure 4-5 presents cross-sectional information from Figure 4-4 at the 144 hour time point for ease of interpretation; the 144 hour time point was chosen to show the greatest differences in responses to treatments before change in metabolic activity appears stagnant perhaps due to cells reaching confluence at 192 hours with media supplemented with VEGF (Figures 4-3 and 4-4).

When surfaces were treated with low 1 µM molecule concentrations, increasing LXW7 substitution produced unexpected bimodal trends. In media lacking VEGF (Figure 4-5A), HMVECs exhibited a bimodal proliferative response to increasing LXW7 substitution with optimal peaks at 2-3.5 and 5.5 LXW7. A similar bimodal shape, but somewhat left shifted, was also seen with VEGF supplementation, peaking at 1 and 4-5.5 LXW7 (Figure 4-5C). The left shift in the presence of VEGF can be expected since it indicates that lower LXW7 substitutions were now able to produce greater responses with the help of VEGF. The bimodal shape suggests that the very low surface LXW7 density present at 1 µM surface treatments caused complex cellular interactions both in the absence and presence VEGF. It is possible that at our very low surface densities, direct LXW7 integrin activation is insignificant such that response over the bioactivities of the DS-SILY$_4$ alone are negligible unless the LXW7 peptide density is in a configuration that promotes potentiated responses. This type of response trend could be at least partially explained by optimal LXW7 surface densities reported in literature for integrin activation, taking into account direct ligand activation as well as additional integrin clustering effects that strengthen downstream signaling (213) and interactions with actin fibers (214-216). Groups of 3 ligated integrins, spaced within 40-60 nm of each other (213, 217), have been reported to form an activated integrin cluster that acts synergistically through focal adhesions and cytoskeletal complexes (215). In fact, clustered integrin spacing induced by small groups of RGD has been shown to strengthen cell adhesions and promote higher cell motility than equivalent homogeneous RGD densities (213, 218-220). Given that dermatan sulfate components of *in vivo* proteoglycans have been reported at 40-70 nm in length (221), it is likely that LXW7 peptides conjugated to a single DS molecule would form an activated integrin cluster. Our data therefore suggests that an optimal substitution of approximately 3 (or multiples of 3) LXW7 per DS may promote optimal proliferative bioactivity through integrin clustering.

While the low concentration surface treatments exhibited bimodal responses, higher concentration treatments showed a more straightforward single optimal LXW7 substitution and positive effect even at 1 LXW7 per DS-SILY$_4$ (Figure 4-5B). At 10 µM without VEGF (Figure 4-5B), all substitutions less than 5.5 were able to significantly increase HMVEC proliferation with the most activity optimal at 3.5 LXW7. It is possible that the higher concentration surface coating enabled direct integrin activation. Interestingly, these variants at 10 µM were as effective as 10 ng/mL VEGF supplementation, causing a 6-fold increase in proliferation, and the 3.5 LXW7 variant appeared to be even more effective than 10 ng/mL VEGF at an 8-fold increase (Figures 4-5 B & D). At 5.5 LXW7 without VEGF (Figure 4-5B), there is an unexpected drop in molecule activity that cannot be explained, but this variant is synergistically effective in the presence of VEGF and appears to take on similar properties as the peg2V-conjugated variant. Since we observed that the 5.5 LXW7 variant was highly effective at the 1 µM concentration, but appears to lose direct efficacy at the 10 µM concentration, perhaps the unexpected effects can be accounted for by a desensitization response.

With VEGF and 10 µM treatments (Figure 4-5D), all degrees of substitution below 5.5 were statistically equivalent to DS-SILY$_4$, but 5.5LXW7-DS-SILY$_4$ showed significantly increased HMVEC proliferation over the DS-SILY$_4$ control. Based on this data, LXW7 synergy with 10 ng/mL VEGF only appeared to be present for the 5.5LXW7-DS-SILY$_4$ variant. The statistical equivalence of DS-SILY$_4$ with all lower LXW7 substitutions suggests that the 10 ng/mL VEGF tested masked the effects of low LXW7 substitution and therefore was too high to tease out synergistic effects. Experiments with lower VEGF concentrations may be necessary to further examine any synergistic effects of the low LXW7 substitution variants. Taken altogether, the results indicate that at 10 µM, lower LXW7 substitutions, optimal at 3.5, provide significant proliferative bioactivity without exogenous VEGF, while high LXW7 substitution variants may not be effective alone but are more effective at potentiating VEGF.

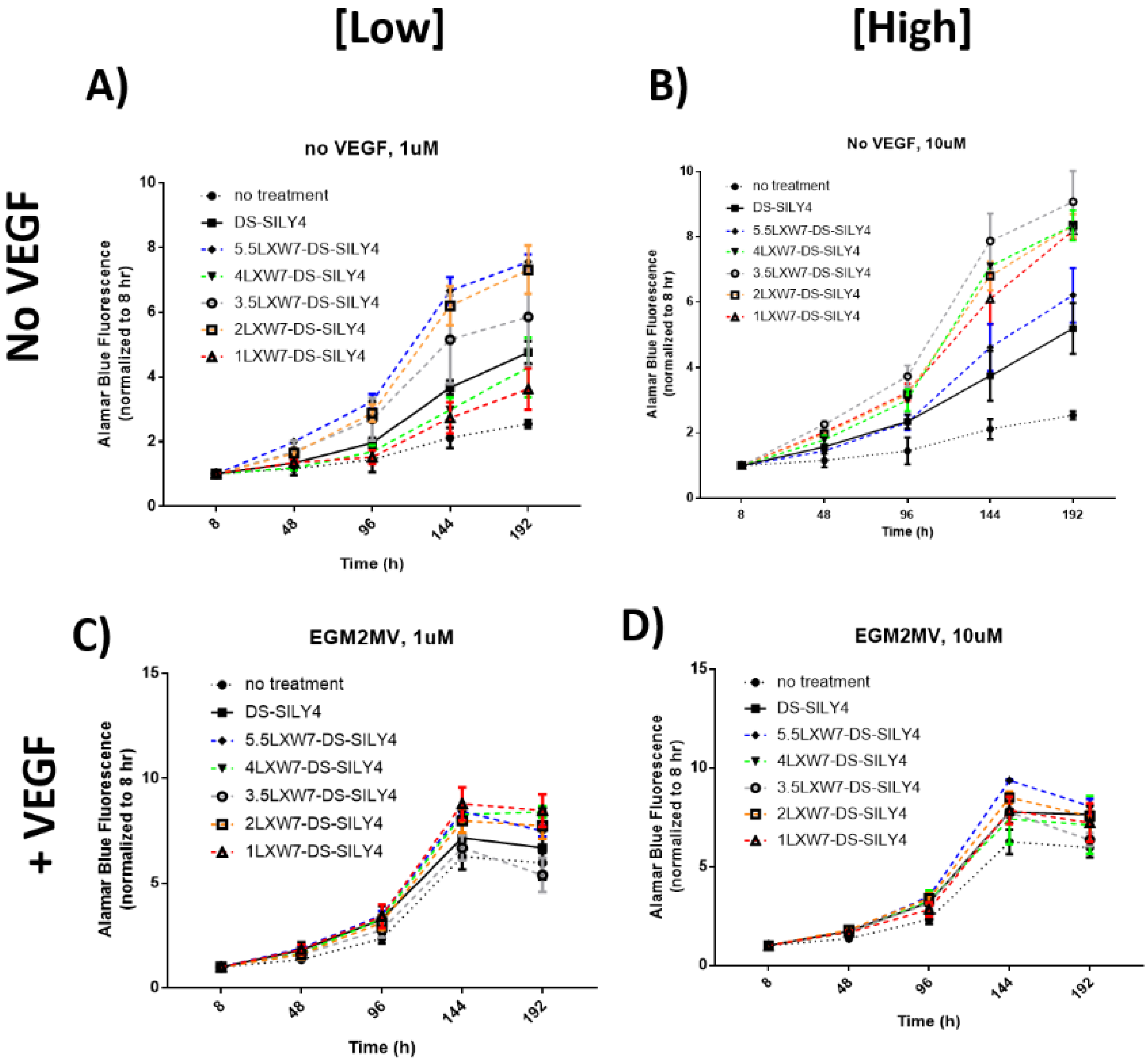

Figure 4-4. **HMVEC Proliferation in Response to LXW7-DS-SILY variants.**

Cell growth appeared to be exponential until 144 hours. Due to the plateauing growth at 192 hours, indicating that the cells were reaching confluence and/or cell density was inhibiting cell metabolism, statistical analyses of differences between groups were performed on measurements from the 144 hour time point, and results are depicted in Figure 4-5. Sample n = 3.

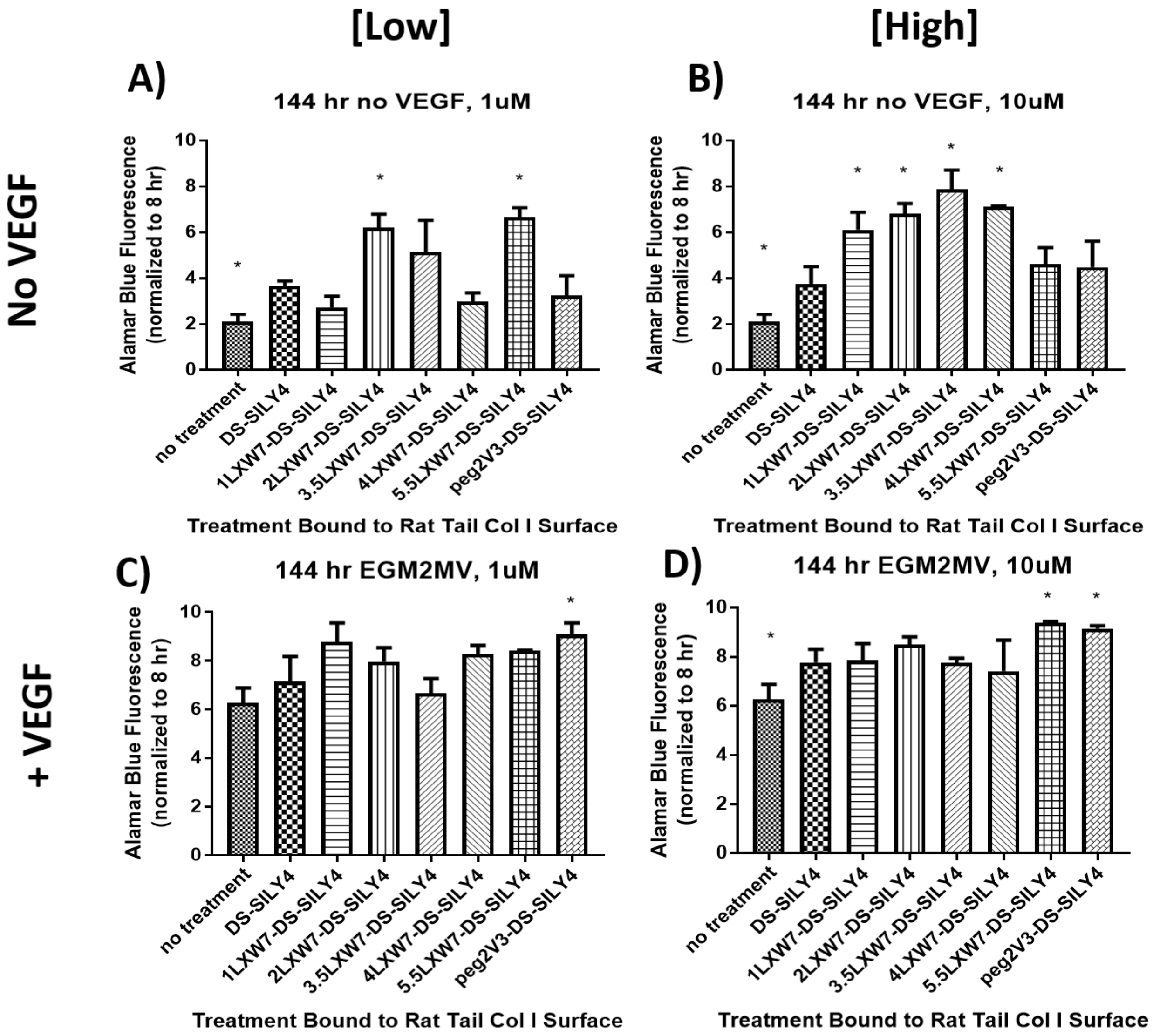

Figure 4-5. **144 hour HMVEC Proliferation in Response to Surface-bound Treatments.**

Figure 4-5 is a cross-sectional representation of Figure 4-4 showing treatment response after 144 hours of exposure, providing ease of interpretation. Sample n = 3, with measurements presented as mean ± standard deviation.

4.4.3 HMVEC Migration Responses to Surface-bound Molecules (ORIS assay)

Migration responses were explored with and without the application of the anti-proliferative agent mitomycin C (MMC) in the ORIS assay to study closure of a circular breach in a confluent endothelial monolayer. Without MMC, the gap closure could be accounted for by both proliferation and migration over the 48 hour assay. With MMC, gap closure was attributed to migratory effects alone.

When cells were exposed to MMC in the absence of VEGF, Peg2V and LXW7 conjugated to DS-SILY$_4$ both significantly stimulated endothelial migration more than DS-SILY$_4$ alone (Figure 4-6). Since the untreated surfaces exhibited a significant increase in gap closure without MMC, normal proliferation must have a significant role in gap closure (Figure 4-6). Without MMC treatment, there were no statistically significant differences in cell coverage between the variants, although the 4LXW7-DS-SILY$_4$ stimulated slightly greater cell coverage (not statistically significant). The results also show that while the gap closure was significantly higher for DS-SILY$_4$ when MMC was removed, gap closure was statistically similar for (peg2V)$_3$-DS-SILY$_4$ with and without MMC (Figure 4-6). Moreover, the gap closure was only slightly increased for 4LXW7-DS-SILY$_4$ when MMC was removed (Figure 4-6). These differences in monolayer closure with and without MMC suggest that the gap closure due to DS-SILY$_4$ is primarily a proliferative response, while coverage from (peg2V)$_3$-DS-SILY$_4$ was from a migratory response and 4LXW7-DS-SILY$_4$ had important contributions from both migration and proliferation. We also note that the migration data without MMC closely matched the observed 48 hour proliferative responses to surface-bound molecules discussed previously in our study (Figure 4-5B); in the absence of VEGF, (peg2V)$_3$-DS-SILY$_4$ stimulated proliferation about the same degree as DS-SILY$_4$ over an untreated collagen surface, while 4LXW7-DS-SILY$_4$ was able to produce a greater proliferative response.

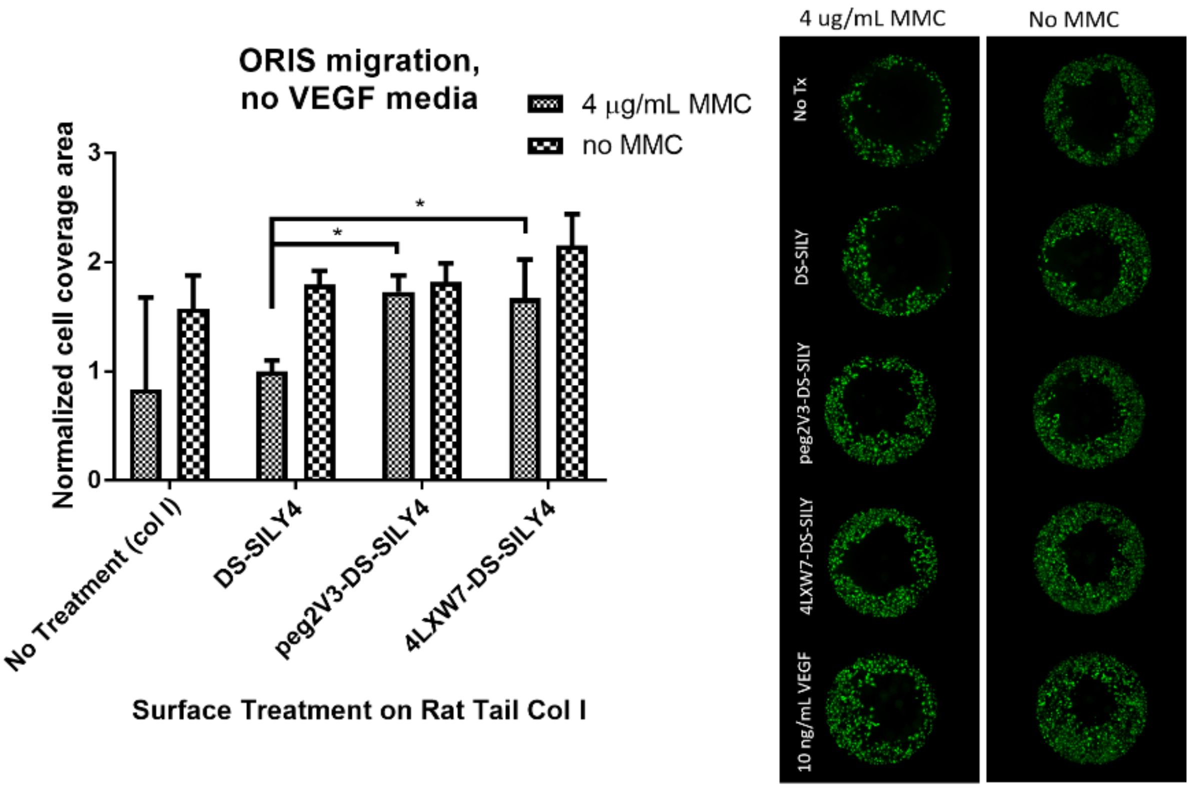

Figure 4-6. **Area of Cell Coverage (Normalized to DS-SILY$_4$) after 48 hours of HMVEC Migration in Response to Surface-Bound Treatments.**

With anti-proliferative MMC, both pro-angiogenic decorin mimic variants elicit a significant migratory response compared to DS-SILY$_4$. Without MMC, cell proliferation accounts for a significant amount of gap closure such that almost all treatments produce approximately the same response. The LXW7-conjugated variant exhibits a trending increase in gap closure even when proliferation is not inhibited. Sample n = 4, with measurements presented as mean ± standard deviation.

4.4.4 HMVEC 2D tubulogenesis in response to matrigel embedded molecules

In vitro matrigel tubulogenesis assays revealed that treatments embedded within gels at a 10 µM concentration had no significant effects on HMVEC tubule number compared to the untreated controls (Figure 4-7). However, tubule length, size, and number of junctions were significantly decreased (Figure 4-7). Increasing the embedded treatment concentration to 20 µM and 30 µM resulted in increased tubule number but also exhibited trending decreases in length, size, and junction number (Figure 4-7) and these effects were more pronounced with pro-angiogenic peptide conjugation to DS-SILY$_4$. Since this assay evaluates the responses of cells seeded on top of the gels, the data suggests that the 10 µM concentration may not present an adequate surface concentration to elicit a detectable response in tubule number. Given the proliferation data (Figures 4-2 through 4-5) and the fact that the tubule number increases, the shorter, thinner, and less branched tubules that form in response to the decorin mimics are unlikely to reflect anti-angiogenic properties; anti-angiogenic treatments cause reduction in all parameters including tubule number. Some limitations of the matrigel assay may convolute the interpretation of our results. While the rapid time course of the matrigel assay with tubules forming within a few hours and then regressing after 12 hours allows for quick screening of angiogenic factors, it may only reflect very acute cellular changes and their corresponding immediate effects on tubule formation. One possible explanation for our findings is that the decorin mimics promote accelerated tubule formation and regression such that regressing tubules were assessed at 8 hours. This tubulogenic response of earlier tubule formation and regression was observed by *Leslie-Barbick et al.* for HUVECs within PEG hydrogels with tethered QK (163). To fully assess this effect, dynamic analysis of tubule formation over time would be necessary. Despite the limitations of our study, it was clear from the matrigel assay that the vascular networks exposed to pro-angiogenic decorin mimics differed in structure compared to untreated controls. Further investigation of longer time-scale 3D *in vitro* tubulogenesis within collagen gels would provide more meaningful insight into the structural differences in tubulogenesis induced by the engineered pro-angiogenic decorin mimics.

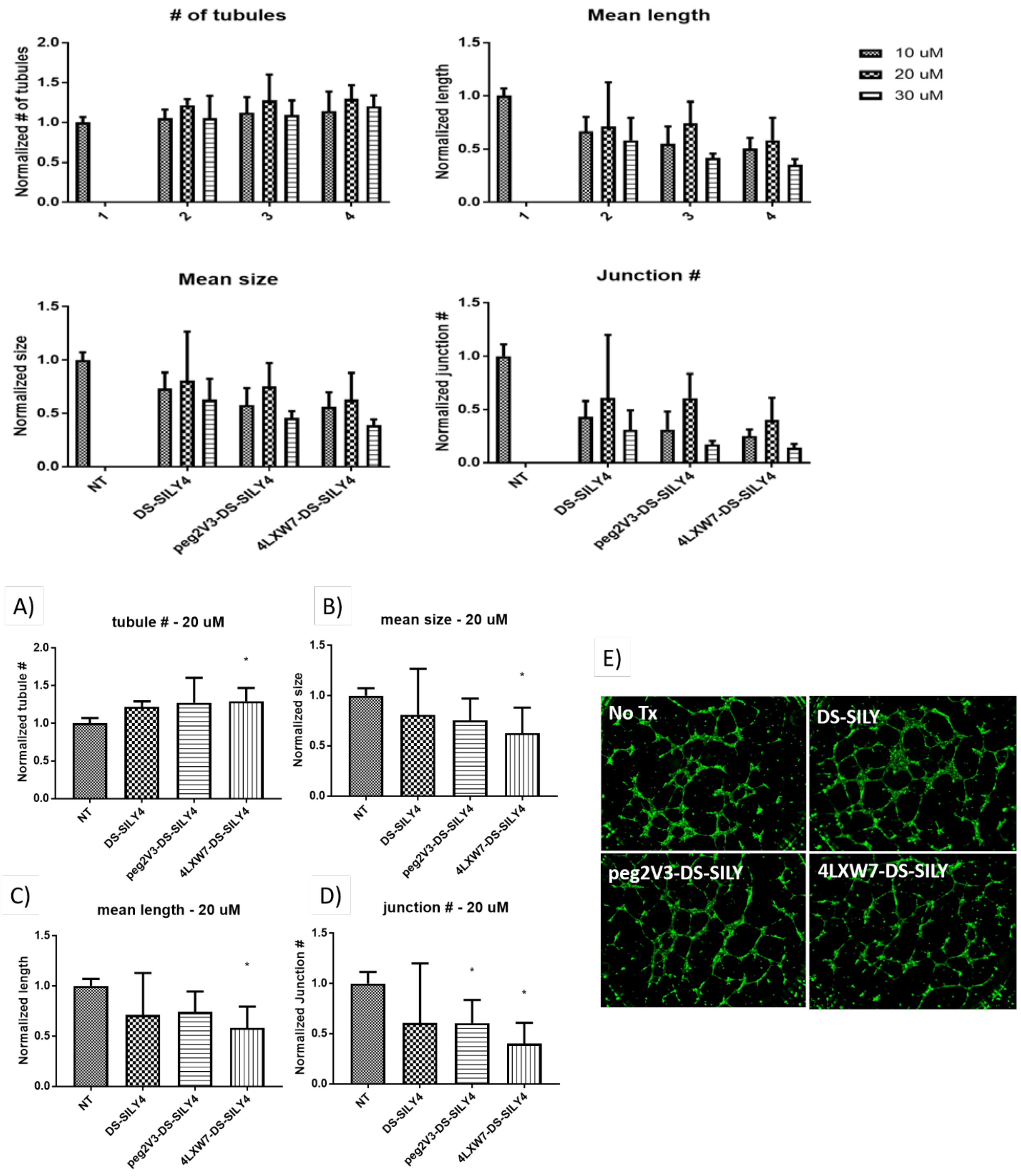

Figure 4-7. **Quantitative Assessment of HMVEC Tubular Networks formed after 8 hours over Matrigel Embedded with Pro-angiogenic Decorin Mimics.**

Treatments are normalized to untreated controls (NT) and values are presented as number of tubules, mean length, mean size, and junction number, as they are defined and determined by AngioQuant software. Subfigures A-E show the corresponding data with asterisks representing statistical significance compared to NT and representative images of tubular networks.

4.4.5 Changes in chick chorioallantoic membrane vascularization in response to collagen gels: eluted vs. embedded tethered molecules

4.4.5.1 Free VEGF-mimicking peptides eluted from collagen gels stimulate acute CAM angiogenesis, while the free integrin-binding LXW7 peptide hinders surrounding vessel formation

Figure 4-8 shows that 100 µM free V and QK peptides had comparable vasculogenic activity to each other and to 2 µg/mL VEGF-A, stimulating acute increases (30-50% compared to matched control gels on the same egg) in the number of blood vessels in a 2 mm radius surrounding implanted 10 mm diameter gels after 24 hours ($n \geq 5$). In contrast, elution of 100 µM LXW7 from collagen gels either decreased or caused no changes in surrounding vessel growth after 24 hours (Figure 4-8 shows a decrease that is not statistically significant). The lack of increased vascularity in response to free LXW7 seen here suggests that the LXW7 peptide needs to be surface-bound to promote angiogenesis. This result is supported by other studies where free LXW7 acts as a competitive inhibitor of αvβ3 integrin to block angiogenesis (203, 204) and is proposed to act by down-regulating VEGF and its associated pathways (175, 176).

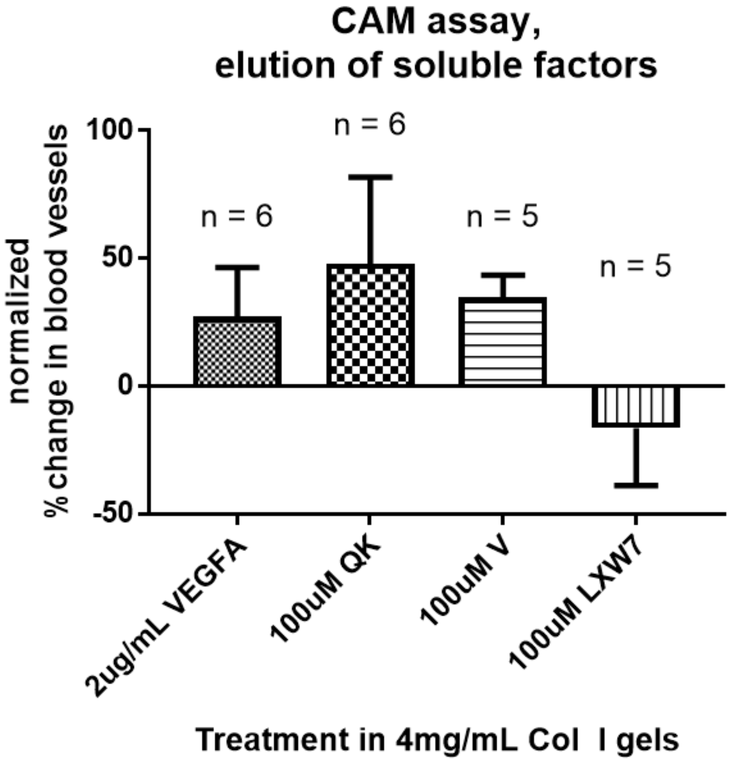

Figure 4-8. **Normalized % Change in CAM Blood Vessels over 24 hours in Response to Elution of Soluble Factors from Collagen I Gels.**

VEGF-A, QK, and V eluting from collagen gels all cause increases in blood vessels surrounding the collagen gels, while LXW7 exhibits a decrease or no change in surrounding vessels over 24 hours.

4.4.5.2 Peg2V conjugation to DS-SILY$_4$ significantly increases vascularization into collagen I gel implants

Both 10 µM and 20 µM DS-SILY$_4$ showed a very slight increase in gel vascularity that was not statistically significant over the blank controls (Figures 4-9 A top row, B, & C). However, Figure 4-9D demonstrates that 10 µM gel-embedded (peg2V)$_3$-DS-SILY$_4$ significantly increased the vascularized area within the gel compared to matched blank controls by day 4 after implantation. Since 10 µM (peg2V)$_3$-DS-SILY$_4$ already showed a significantly improved vascular response, the 20 µM concentration was not investigated. As can be seen in the representative vascularized gel images (Figure 4-9A), new vessels invaded the collagen gels in a radial fashion with many vessels going towards and then away from the center of the transplanted gel. Under high magnification through a stereoscope, rapidly flowing red blood cells were apparent within the invading capillaries with directional flow indicative of the presence of both new arterioles and venules (data not shown).

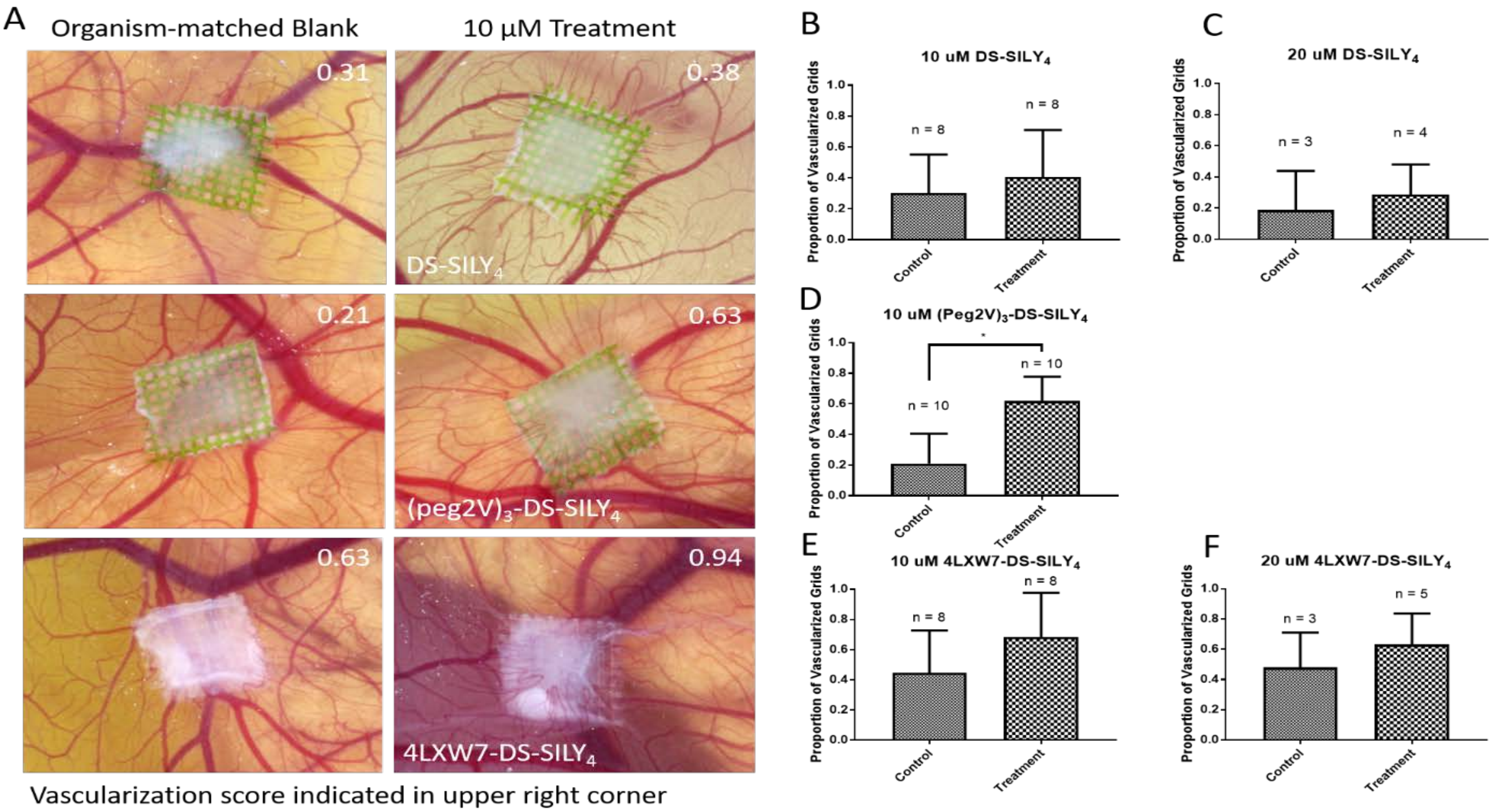

Figure 4-9. **CAM vascularization of collagen gels embedded with pro-angiogenic decorin mimics.**

Subfigure A displays representative images of vascularized gels with 10 µM treatments compared to their organism-matched control gels, with vascularization scores (scored by two independent observers) indicated in the upper right corner of each image. Subfigures B-F show the quantitative results for treatments. Peg2V3-DS-SILY4 was able to significantly increase vascularization into the treatment-embedded collagen gel. LXW7-DS-SILY4 treatment was able increase vascularization as well, but also appeared to increase vascularization of organism-matched controls. 10 µM DS-SILY$_4$: 8 control gels and 8 treatment gels over 4 chicken embryos; 20 µM DS-SILY$_4$: 3 control gels and 4 treatment gels over 2 embryos. 10 µM (peg2V)$_3$-DS-SILY$_4$: 10 control gels and 10 treatment gels over 5 chicken embryos. 10 µM 4LXW7-DS-SILY$_4$: 8 control gels and 8 treatment gels over 4 chicken embryos; 20 µM 4LXW7-DS-SILY$_4$: 3 control gels and 4 treatment gels over 2 embryos.

4.4.5.3 LXW7 conjugation to DS-SILY$_4$ increases vascularization into collagen I gel implants to a similar degree as (peg2V)$_3$-DS-SILY$_4$, but also increases vascularization into organism-matched blank control collagen gels

Both 10 µM and 20 µM 4LXW7-DS-SILY$_4$ embedded gels caused a large increase in vascularized gel area, but not statistically significant than the organism-matched blank controls (Figures 4-9 E & F). In fact, 10 µM and 20 µM 4LXW7-DS-SILY$_4$ treatments produced almost identical gel vascularization results (Figures 4-9 E & F). Interestingly, the proportion of vascularized gel area in 4LXW7-DS-SILY$_4$ treated gels was similar to that seen for (peg2V)$_3$-DS-SILY$_4$ treated gels, but the organism-matched blank controls exhibited an trending increase in vascularity compared to blank controls on eggs treated with DS-SILY$_4$ and (peg2V)$_3$-DS-SILY$_4$ (Figures 4-9 E & F compared with B & C). Since the increase in the blank controls was not present in the DS-SILY$_4$ or (peg2V)$_3$-DS-SILY$_4$ treated eggs, it is more likely that this unexpected increase in the blank control gels results from an LXW7-induced a systemic response perhaps by release of angiogenic factors into the blood circulation rather than 4LXW7-DS-SILY$_4$ releasing from the collagen gel.

4.4.5.4 New vasculature within collagen gels exhibit increased vascular permeability regardless of treatment

Vascular permeability was qualitatively assessed by high molecular weight RITC-dextran intravascular injection through fluorescent imaging of the *ex ovo* CAM model. In an attempt to better visualize new vasculature invading the implanted collagen gels, we injected ~100 µL 1 mg/mL high molecular weight fluorescent dextran (70 kDa RITC-dextran) into the CAM vessels 7 days after transplantation, cut out integrated collagen gels and surrounding membrane, and imaged with fluorescence microscopy. For proof-of-concept, control CAMs without transplanted gels were injected and imaged with this method and demonstrated that the fluorescent dextran reasonably represented the vasculature without leaking outside the vessels (Figure 4-10A). In our studies, both treatment and blank collagen gels showed diffuse red fluorescence in all eggs (Figure 4-10B). This fluorescent signal was not present in blank collagen gels not exposed to RITC-dextran (data not shown). Since all the collagen gels exhibited some degree of leakiness measured by the RITC-dextran fluorescence, it is difficult to infer the permeability effects of the collagen-bound treatment molecules. Injection of 100 µL of a 2% w/v Evans blue in PBS for better visualization of extravasate suggested that while all the collagen gels had some accumulation of the blue dye, the $(peg2V)_3$-DS-$SILY_4$ gels looked darker indicating increased vascular permeability in surrounding vessels (Figure 4-11). Due to the low yields of successful injection distributing fully through systemic CAM circulation, determined by a color change in all visible vessels, sufficient data was not acquired to make conclusions through the Evans blue vascular injection method. Further studies increasing the number of eggs and gels analyzed are needed to determine *in vivo* permeability.

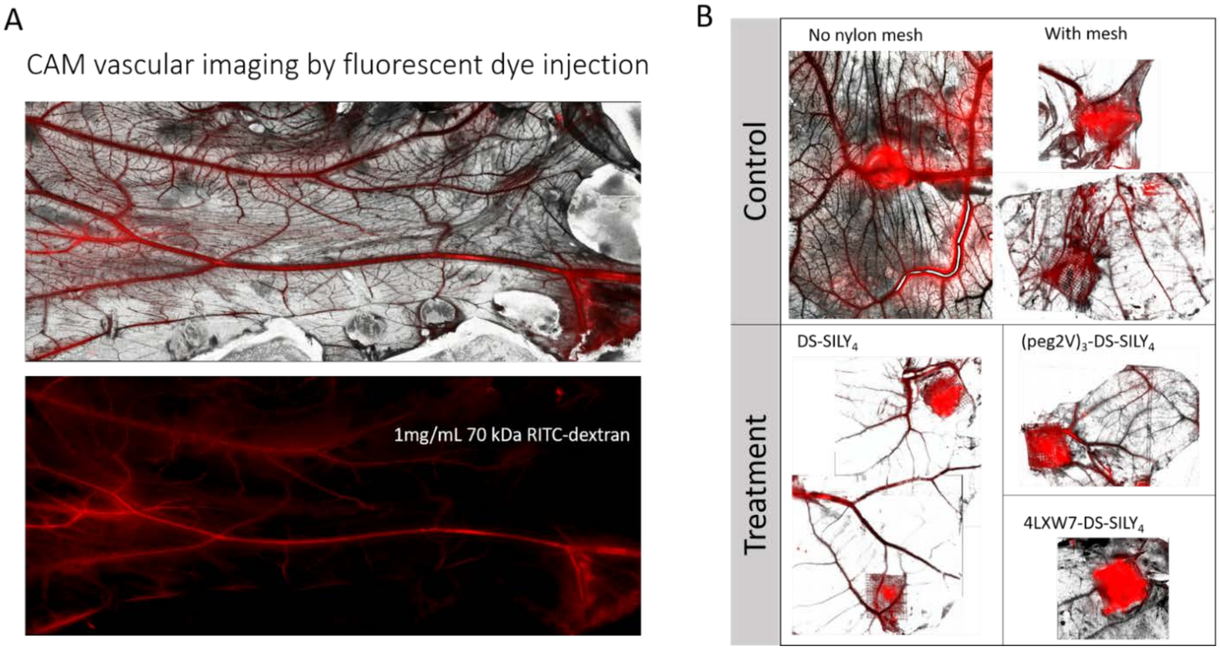

Figure 4-10. **Fluorescent vascular imaging of CAM by injection of high molecular weight RITC-dextran.**

Subfigure A shows vascular network highlighted in a control CAM without any gel, while subfigure B depicts CAM vascular networks with embedded collagen gels with and without embedded nylon mesh and/or pro-angiogenic decorin mimic treatments. Bright red signal within the collagen gels suggests hyperpermeable vasculature in both control and treatment gels.

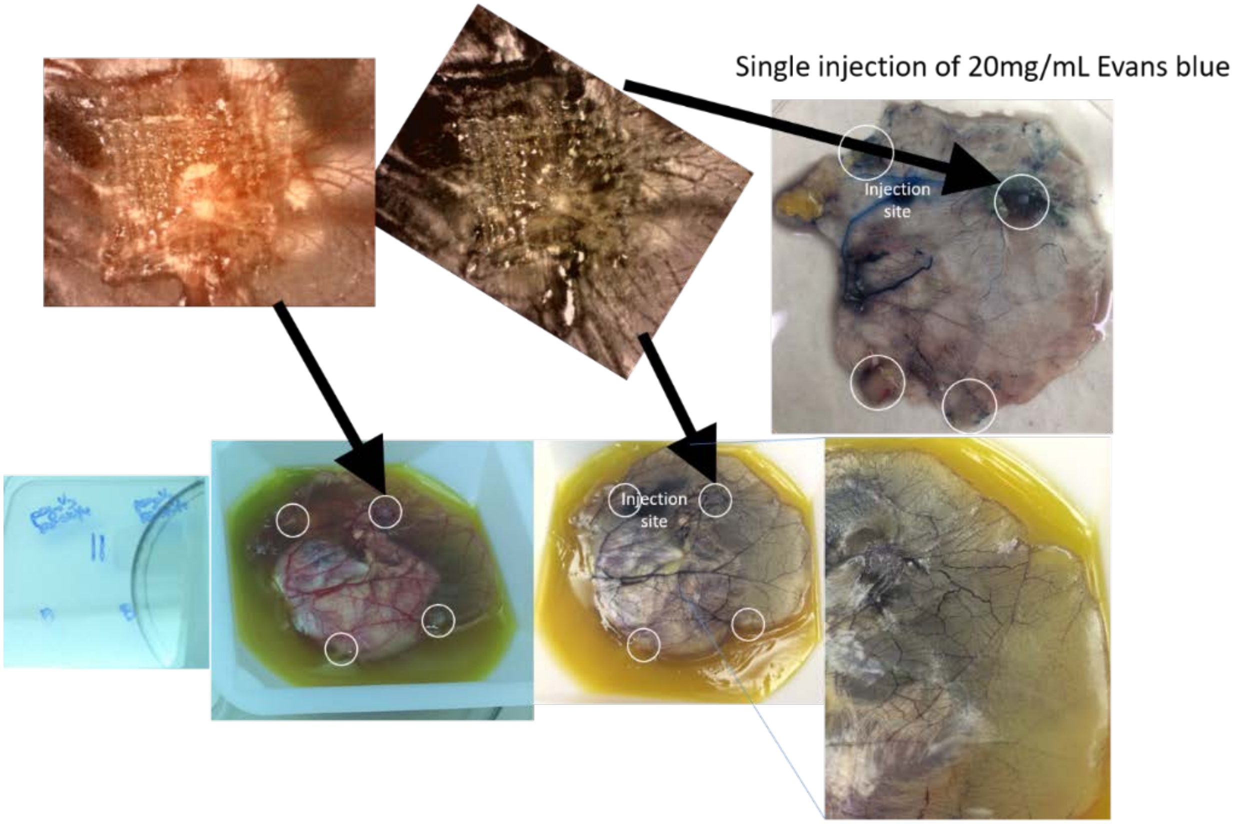

Figure 4-11. **Permeability of new vessels inside the embedded collagen gel assessed by injection of 20 mg/mL Evan's Blue.**

Pilot studies investigating *in vivo* permeability in the CAM model show that new vasculature induced by peg2V$_3$-DS-SILY$_4$ may be hyperpermeable due to increased extravasation and accumulation of Evans Blue at these treatment gel sites.

4.4.6 Effects of soluble VEGF-mimicking molecules on HMVEC monolayer permeability (Transwell)

Given that the CAM assay suggested that the tested molecules may be altering vascular permeability and that VEGF is also known as vascular permeability factor and is hence widely known to increase vascular permeability (222), we were interested in the effects of VEGF-mimicking peptides on endothelial permeability in comparison to VEGF. Multiple studies investigating endothelial permeability by various methods have shown that VEGF induces permeability in a transient, highly time-dependent manner with significant effects seen within 10 minutes to 1 hour of VEGF stimulation and changing over multiple days (222), although the specific dynamics varied depending on measurement method and endothelial cell type . We therefore followed treatments after 10 minutes through 3 days, although it is worth noting that our experimental method effectively investigated permeability effects after a series of repeated bolus treatments of soluble molecules on a HMVEC monolayer. The transwell results in Figure 4-12A demonstrate that the seeded HMVECs indeed formed a monolayer significantly decreasing permeation of the 70 kDa RITC-dextran compared to wells with no cells, while Figures 4-12 A and C indicate that EDC-reacted DS had no effects on permeability. Figure 4-12B shows that as short as 10 minute incubation of 10 ng/mL VEGF, 30 µM QK, and 10 µM DS-(peg2V)$_3$ increased monolayer permeability compared to the non-treated media (EGM2-MV lacking VEGF) and 10 µM EDC-reacted DS, although only the QK and DS-(peg2V)$_3$ groups showed statistically significant increases in our experiment. After 18 hours, the increases in VEGF- and QK- induced permeability had disappeared, while DS-(peg2V)$_3$ still maintained significantly increased permeability (Figure 4-12B). By 24 hours, the permeability of DS-(peg2V)$_3$ treated wells recovered to control levels (Figure 4-12B). By extending treatments out to 48 and 72 hours, both the VEGF and DS-(peg2V)$_3$ treatments actually showed trending decreases in monolayer permeability (Figure 4-12C). Both VEGF and DS-(peg2V)$_3$ were significantly different from untreated controls by 72 hours, and the effect of 10 µM DS-(peg2V)$_3$ was statistically equivalent to 10 ng/mL VEGF (Figure 4-12C).

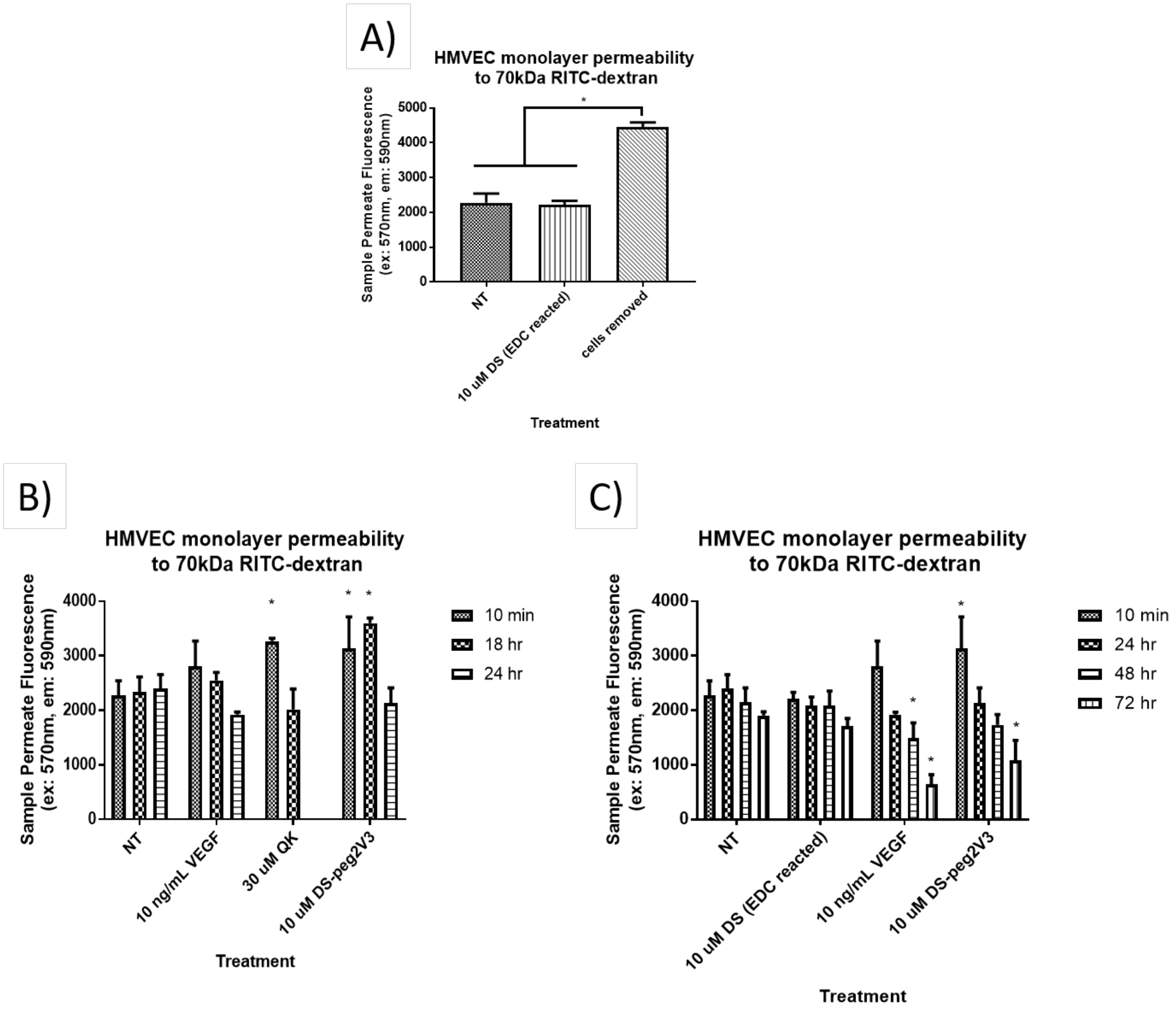

Figure 4-12. **HMVEC *in vitro* monolayer permeability assessed in Transwell chambers.**

The endothelial cell monolayer provides a measurable decrease in permeability to a high molecular weight 70kDa RITC-dextran (A). Both VEGF and QK stimulate transient hyperpermeability that resolves within 18 hours of treatment whereas DS-peg2V$_3$ has a slightly prolonged hyperpermeable response that recovers by 24 hours (B). Peg2V conjugated to DS at a substitution of 3 provides responses similar to VEGF, gradually tightening the monolayer after 24 hours of bolus treatments (C).

A preliminary study of the effects of free LXW7 and DS-(LXW7)$_4$ in the transwell system did not produce permeability effects comparable to VEGF treatment (data not shown). Although other groups have reported that free LXW7 inhibits VEGF-mediated permeability (176), we did not explore this property of free LXW7 in our transwell system because it would be difficult to use these experiments to infer the vascular permeability effects of surface-bound LXW7.

4.5 *Conclusions*

In summary, we report two variants of pro-angiogenic decorin mimics conjugated with VEGF-mimicking QK peptide and integrin-binding LXW7 peptide that activate VEGF pathways through direct and indirect mechanisms, respectively. While LXW7-conjugated variants appear to stimulate proliferation without VEGF, the peg2V-conjugated variant potentiated VEGF proliferative responses. In solution, the longer linker of peg2V peptide was necessary to exert effective proliferative response from the VEGF-mimicking sequence. Both (peg2V)$_3$-DS-SILY$_4$ and 4LXW7-DS-SILY$_4$ variants stimulate endothelial migration. Furthermore, the pro-angiogenic decorin mimics increased EC tubule formation although networks were thinner, shorter, and less branched. *In vivo*, CAM neovascularization into a collagen scaffold embedded with pro-angiogenic decorin mimics demonstrated increased angiogenesis for treated gels, although control gels on 4LXW7-DS-SILY$_4$ treated chicks also exhibited increased vascularity. Since pilot studies showed increased Evan’s blue and RITC-dextran accumulation at CAM collagen gel implant sites, EC monolayer permeability was also assessed *in vitro*. We found that peg2V conjugated to DS caused prolonged hyperpermeability that was not present with free QK. However, over longer periods of treatment, the DS(peg2V)$_3$ was able to reduce hyperpermeability on a similar time scale as VEGF.

In addition to discussing the angiogenic activity of the two variants, these results support the importance of peptide context in affecting bioactivity. We demonstrate that peg2V immobilized to collagen surfaces by DS-SILY$_4$ at low surface densities can stimulate migration and potentiate proliferation. Our results also show that LXW7 presented in specific patterns and surface densities could exhibit an amplified bioactive response, and that free LXW7 produces an anti-angiogenic response. The data therefore highlights that soluble peptides can have a drastically different response compared to surface-bound peptides and that densities promoting receptor clustering may be beneficial in exploiting potentiated receptor activation.

5. CONCLUSIONS

5.1 *Conclusions and Future Directions*

The complex pathophysiological environment of chronic ischemic diabetic foot ulcers presents a significant challenge for angiogenic growth factor therapies. Through the chapters of this dissertation, 3 therapies were proposed that could be used in combination and address multiple aspects of impaired healing. The focus of chapter 2 was the development of a nanoparticle system to protect and deliver VEGF over a sustained period of time to the wound bed. Incremental improvements were made in a system designed to deliver anti-inflammatory peptides in osteoarthritic models and the final improved system was adapted for VEGF loading and release. However, although the developed system was able to achieve high loading efficiency of VEGF, a very small fraction of the loaded VEGF was released and most of the release occurred within the first 12 hours. As most of the VEGF was still trapped in the particle, the particles' release capacity could be improved by incorporating degradability.

The combined focus of chapters 3 and 4 was the development and characterization of pro-angiogenic decorin mimics that simultaneously protect healing tissue, stimulate revascularization, and potentially recruit endothelial progenitor cells (in the case of LXW7-DS-SILY$_4$). Studies investigating endothelial recruitment by LXW7-DS-SILY$_4$ are also underway. As the (peg2V)$_3$-DS-SILY$_4$ and 5.5LXW7-DS-SILY$_4$ variants demonstrated VEGF potentiation, they would be appropriate therapies to combine with the VEGF-releasing nanoparticles. These variants could also be administered alone as they would potentiate endogenous VEGF, and the (peg2V)$_3$-DS-SILY$_4$ variant demonstrated revascularization efficacy *in vivo*. The lower substitution LXW7-DS-SILY$_4$ variants administered alone were shown to stimulate endothelial proliferation and migration *in vitro* and revascularization *in vivo*, although further investigation of the cause of increased vascularization in controls on LXW7-DS-SILY$_4$ treated animals is necessary as increased angiogenesis distant from the site of application is undesirable. Moreover, our CAM study serves only as a proof-of-concept for stimulation of angiogenesis. The next step in determining efficacy is to perform *in vivo* small animal studies specifically investigating diabetic ischemic wound healing.

Although we have shown angiogenic efficacy through proliferation, migration, and vascularization of collagen gels, many more studies will help better characterize the bioactivity of our molecules. First, with our limited understanding from 2D tubulogenesis assays, more in depth examination of *in vitro* tubulogenesis using 3D models in collagen gels would better characterize the angiogenic bioactivity. Further exploration of new vessel permeability is also warranted. The studies determined that all collagen gels induced leaky vessels in the CAM model, but pro-angiogenic decorin mimic-induced mimics might be leakier. In vitro assessment of permeability demonstrated that conjugated Peg2V prolongs VEGF-induced permeability, but has comparable effects to VEGF by tightening the endothelial barrier after several bolus treatments over 72 hours. The effects are likely the result of differing receptor activation kinetics and thus future dynamic studies of receptor activation and downstream second messengers would help elucidate the angiogenic mechanisms.

Overall, the nanoparticle delivery of VEGF and two pro-angiogenic decorin mimic variants show promise in tackling multiple aspects of disease in the diabetic wound. Given the two different mechanisms of action and different pro-angiogenic responses that we observed, it would also be interesting to conjugate both peptides simultaneously to exploit integrin-VEGF receptor crosstalk. If these pro-angiogenic therapies can be proven clinically to provide controlled, targeted angiogenesis, the engineered molecules could have even wider applications to many types of ischemic wounds, including injured myocardium or ischemic bowel.

REFERENCES

1. Control CfD, Prevention. National diabetes statistics report: estimates of diabetes and its burden in the United States, 2014. Atlanta, GA: US Department of Health and Human Services. 2014.

2. Singh N, Armstrong DG, Lipsky BA. Preventing foot ulcers in patients with diabetes. Jama. 2005;293(2):217-28. doi: 10.1001/jama.293.2.217. PubMed PMID: 15644549.

3. Boulton AJ. The pathway to foot ulceration in diabetes. The Medical clinics of North America. 2013;97(5):775-90. doi: 10.1016/j.mcna.2013.03.007. PubMed PMID: 23992891.

4. Alexiadou K, Doupis J. Management of diabetic foot ulcers. Diabetes therapy : research, treatment and education of diabetes and related disorders. 2012;3(1):4. doi: 10.1007/s13300-012-0004-9. PubMed PMID: 22529027; PMCID: 3508111.

5. Armstrong DG, Cohen K, Courric S, Bharara M, Marston W. Diabetic foot ulcers and vascular insufficiency: our population has changed, but our methods have not. Journal of diabetes science and technology. 2011;5(6):1591-5. PubMed PMID: 22226282; PMCID: 3262731.

6. Albayati MA, Shearman CP. Peripheral arterial disease and bypass surgery in the diabetic lower limb. The Medical clinics of North America. 2013;97(5):821-34. doi: 10.1016/j.mcna.2013.03.009. PubMed PMID: 23992894.

7. Baltzis D, Eleftheriadou I, Veves A. Pathogenesis and treatment of impaired wound healing in diabetes mellitus: new insights. Advances in therapy. 2014;31(8):817-36. doi: 10.1007/s12325-014-0140-x. PubMed PMID: 25069580.

8. Sen CK, Gordillo GM, Roy S, Kirsner R, Lambert L, Hunt TK, Gottrup F, Gurtner GC, Longaker MT. Human skin wounds: a major and snowballing threat to public health and the economy. Wound repair and regeneration : official publication of the Wound Healing Society [and] the European Tissue Repair Society. 2009;17(6):763-71. doi: 10.1111/j.1524-475X.2009.00543.x. PubMed PMID: 19903300; PMCID: 2810192.

9. Best Practice Guidelines: Wound Management in Diabetic Foot Ulcers. Wounds International. 2013.

10. Moura LI, Dias AM, Carvalho E, de Sousa HC. Recent advances on the development of wound dressings for diabetic foot ulcer treatment--a review. Acta biomaterialia. 2013;9(7):7093-114. doi: 10.1016/j.actbio.2013.03.033. PubMed PMID: 23542233.

11. Dumville JC, Soares MO, O'Meara S, Cullum N. Systematic review and mixed treatment comparison: dressings to heal diabetic foot ulcers. Diabetologia. 2012;55(7):1902-10. doi: 10.1007/s00125-012-2558-5. PubMed PMID: 22544222; PMCID: 3369130.

12. Marston WA, Hanft J, Norwood P, Pollak R, Dermagraft Diabetic Foot Ulcer Study G. The efficacy and safety of Dermagraft in improving the healing of chronic diabetic foot ulcers: results of a prospective randomized trial. Diabetes care. 2003;26(6):1701-5. PubMed PMID: 12766097.

13. Zaulyanov L, Kirsner RS. A review of a bi-layered living cell treatment (Apligraf) in the treatment of venous leg ulcers and diabetic foot ulcers. Clin Interv Aging. 2007;2(1):93-8. PubMed PMID: 18044080; PMCID: PMC2684073.

14. Smiell JM. Clinical safety of becaplermin (rhPDGF-BB) gel. Becaplermin Studies Group. American journal of surgery. 1998;176(2A Suppl):68S-73S. PubMed PMID: 9777975.

15. Berse B, Brown LF, Van De Water L, Dvorak HF, Senger DR. Vascular permeability factor (vascular endothelial growth factor) gene is expressed differentially in normal tissues, macrophages, and tumors. Molecular biology of the cell. 1992;3(2):211-20.

16. Li J, Zhang YP, Kirsner RS. Angiogenesis in wound repair: angiogenic growth factors and the extracellular matrix. Microscopy research and technique. 2003;60(1):107-14. doi: 10.1002/jemt.10249. PubMed PMID: 12500267.

17. Werner S, Grose R. Regulation of wound healing by growth factors and cytokines. Physiological reviews. 2003;83(3):835-70. Epub 2003/07/05. doi: 10.1152/physrev.00031.2002. PubMed PMID: 12843410.

18. Beer HD, Longaker MT, Werner S. Reduced expression of PDGF and PDGF receptors during impaired wound healing. The Journal of investigative dermatology. 1997;109(2):132-8. PubMed PMID: 9242497.

19. Doxey DL, Ng MC, Dill RE, Iacopino AM. Platelet-derived growth factor levels in wounds of diabetic rats. Life sciences. 1995;57(11):1111-23. PubMed PMID: 7658918.

20. Frank S, Hubner G, Breier G, Longaker MT, Greenhalgh DG, Werner S. Regulation of vascular endothelial growth factor expression in cultured keratinocytes. Implications for normal and impaired wound healing. The Journal of biological chemistry. 1995;270(21):12607-13. PubMed PMID: 7759509.

21. Lerman OZ, Galiano RD, Armour M, Levine JP, Gurtner GC. Cellular dysfunction in the diabetic fibroblast: impairment in migration, vascular endothelial growth factor production, and response to hypoxia. The American journal of pathology. 2003;162(1):303-12. doi: 10.1016/S0002-9440(10)63821-7. PubMed PMID: 12507913; PMCID: 1851127.

22. Thangarajah H, Yao D, Chang EI, Shi Y, Jazayeri L, Vial IN, Galiano RD, Du XL, Grogan R, Galvez MG, Januszyk M, Brownlee M, Gurtner GC. The molecular basis for impaired hypoxia-induced VEGF expression in diabetic tissues. Proceedings of the National Academy of Sciences of the United States of America. 2009;106(32):13505-10. doi: 10.1073/pnas.0906670106. PubMed PMID: 19666581; PMCID: 2726398.

23. Maruyama K, Asai J, Ii M, Thorne T, Losordo DW, D'Amore PA. Decreased macrophage number and activation lead to reduced lymphatic vessel formation and contribute to impaired diabetic wound healing. The American journal of pathology. 2007;170(4):1178-91. doi: 10.2353/ajpath.2007.060018. PubMed PMID: 17392158; PMCID: 1829452.

24. Schurmann C, Goren I, Linke A, Pfeilschifter J, Frank S. Deregulated unfolded protein response in chronic wounds of diabetic ob/ob mice: a potential connection to inflammatory and angiogenic disorders in diabetes-impaired wound healing. Biochemical and biophysical research communications. 2014;446(1):195-200. doi: 10.1016/j.bbrc.2014.02.085. PubMed PMID: 24583133.

25. Werner S, Breeden M, Hübner G, Greenhalgh DG, Longaker MT. Induction of keratinocyte growth factor expression is reduced and delayed during wound healing in the genetically diabetic mouse. Journal of Investigative Dermatology. 1994;103(4):469-73.

26. Werner S, Peters KG, Longaker MT, Fuller-Pace F, Banda MJ, Williams LT. Large induction of keratinocyte growth factor expression in the dermis during wound healing. Proceedings of the National Academy of Sciences of the United States of America. 1992;89(15):6896-900. PubMed PMID: 1379725; PMCID: 49611.

27. Galkowska H, Wojewodzka U, Olszewski WL. Chemokines, cytokines, and growth factors in keratinocytes and dermal endothelial cells in the margin of chronic diabetic foot ulcers. Wound repair and regeneration : official publication of the Wound Healing Society [and] the European Tissue Repair Society. 2006;14(5):558-65. doi: 10.1111/j.1743-6109.2006.00155.x. PubMed PMID: 17014667.

28. Buchberger B, Follmann M, Freyer D, Huppertz H, Ehm A, Wasem J. The importance of growth factors for the treatment of chronic wounds in the case of diabetic foot ulcers. GMS health technology assessment. 2010;6:Doc12. doi: 10.3205/hta000090. PubMed PMID: 21289885; PMCID: 3010891.

29. Buchberger B, Follmann M, Freyer D, Huppertz H, Ehm A, Wasem J. The evidence for the use of growth factors and active skin substitutes for the treatment of non-infected diabetic foot ulcers (DFU): a health technology assessment (HTA). Experimental and clinical endocrinology & diabetes : official journal, German Society of Endocrinology [and] German Diabetes Association. 2011;119(8):472-9. doi: 10.1055/s-0031-1279713. PubMed PMID: 21811960.

30. Kolluru GK, Bir SC, Kevil CG. Endothelial dysfunction and diabetes: effects on angiogenesis, vascular remodeling, and wound healing. International journal of vascular medicine. 2012;2012:918267. doi: 10.1155/2012/918267. PubMed PMID: 22611498; PMCID: 3348526.

31. Stout RW. Glucose inhibits replication of cultured human endothelial cells. Diabetologia. 1982;23(5):436-9. PubMed PMID: 7173520.

32. Doyle JW, Smith RM, Roth TP. The effect of hyperglycemia and insulin on the replication of cultured human microvascular endothelial cells. Hormone and metabolic research = Hormon- und Stoffwechselforschung = Hormones et metabolisme. 1997;29(1):43-5. doi: 10.1055/s-2007-978979. PubMed PMID: 9049654.

33. Lorenzi M, Nordberg JA, Toledo S. High glucose prolongs cell-cycle traversal of cultured human endothelial cells. Diabetes. 1987;36(11):1261-7. PubMed PMID: 3666318.

34. Baumgartner-Parzer SM, Wagner L, Pettermann M, Grillari J, Gessl A, Waldhausl W. High-glucose--triggered apoptosis in cultured endothelial cells. Diabetes. 1995;44(11):1323-7. PubMed PMID: 7589831.

35. Zou MH, Shi C, Cohen RA. High glucose via peroxynitrite causes tyrosine nitration and inactivation of prostacyclin synthase that is associated with thromboxane/prostaglandin H(2) receptor-mediated apoptosis and adhesion molecule expression in cultured human aortic endothelial cells. Diabetes. 2002;51(1):198-203. PubMed PMID: 11756341.

36. Shoji T, Koyama H, Morioka T, Tanaka S, Kizu A, Motoyama K, Mori K, Fukumoto S, Shioi A, Shimogaito N. Receptor for advanced glycation end products is involved in impaired angiogenic response in diabetes. Diabetes. 2006;55(8):2245-55.

37. Schmidt AM, Hori O, Chen JX, Li JF, Crandall J, Zhang J, Cao R, Yan SD, Brett J, Stern D. Advanced glycation endproducts interacting with their endothelial receptor induce expression of vascular cell adhesion molecule-1 (VCAM-1) in cultured human endothelial cells and in mice. A potential mechanism for the accelerated vasculopathy of diabetes. The Journal of clinical investigation. 1995;96(3):1395-403. doi: 10.1172/JCI118175. PubMed PMID: 7544803; PMCID: 185762.

38. Liu H, Yu S, Zhang H, Xu J. Angiogenesis impairment in diabetes: role of methylglyoxal-induced receptor for advanced glycation endproducts, autophagy and vascular endothelial growth factor receptor 2. PloS one. 2012;7(10):e46720. doi: 10.1371/journal.pone.0046720. PubMed PMID: 23056421; PMCID: 3463541.

39. Asai J, Takenaka H, Ii M, Asahi M, Kishimoto S, Katoh N, Losordo DW. Topical application of ex vivo expanded endothelial progenitor cells promotes vascularisation and wound healing in diabetic mice. International wound journal. 2013;10(5):527-33. doi: 10.1111/j.1742-481X.2012.01010.x. PubMed PMID: 22738265.

40. Zhuge Y, Gonzalez S, Velazquez OC. Diabetic Foot Ulcers: Effects of Hyperoxia and Stromal-Derived Factor-1α on Endothelial Progenitor Cells. The Diabetic Foot: Springer; 2012. p. 217-29.

41. Tecilazich F, Dinh T, Pradhan-Nabzdyk L, Leal E, Tellechea A, Kafanas A, Gnardellis C, Magargee ML, Dejam A, Toxavidis V, Tigges JC, Carvalho E, Lyons TE, Veves A. Role of endothelial progenitor cells and inflammatory cytokines in healing of diabetic foot ulcers. PloS one. 2013;8(12):e83314. doi: 10.1371/journal.pone.0083314. PubMed PMID: 24358275; PMCID: 3865213.

42. Loomans CJ, de Koning EJ, Staal FJ, Rookmaaker MB, Verseyden C, de Boer HC, Verhaar MC, Braam B, Rabelink TJ, van Zonneveld AJ. Endothelial progenitor cell dysfunction: a novel concept in the pathogenesis of vascular complications of type 1 diabetes. Diabetes. 2004;53(1):195-9. PubMed PMID: 14693715.

43. Gallagher KA, Liu ZJ, Xiao M, Chen H, Goldstein LJ, Buerk DG, Nedeau A, Thom SR, Velazquez OC. Diabetic impairments in NO-mediated endothelial progenitor cell mobilization and homing are reversed by hyperoxia and SDF-1 alpha. The Journal of clinical investigation. 2007;117(5):1249-59. doi: 10.1172/JCI29710. PubMed PMID: 17476357; PMCID: 1857264.

44. Tepper OM, Galiano RD, Capla JM, Kalka C, Gagne PJ, Jacobowitz GR, Levine JP, Gurtner GC. Human endothelial progenitor cells from type II diabetics exhibit impaired proliferation, adhesion, and incorporation into vascular structures. Circulation. 2002;106(22):2781-6. PubMed PMID: 12451003.

45. Tie L, Chen LY, Chen DD, Xie HH, Channon KM, Chen AF. GTP cyclohydrolase I prevents diabetic-impaired endothelial progenitor cells and wound healing by suppressing oxidative stress/thrombospondin-1. American journal of physiology Endocrinology and metabolism. 2014;306(10):E1120-31. doi: 10.1152/ajpendo.00696.2013. PubMed PMID: 24644242.

46. Schultz GS, Wysocki A. Interactions between extracellular matrix and growth factors in wound healing. Wound repair and regeneration : official publication of the Wound Healing Society [and] the European Tissue Repair Society. 2009;17(2):153-62. doi: 10.1111/j.1524-475X.2009.00466.x. PubMed PMID: 19320882.

47. Bitar MS, Labbad ZN. Transforming growth factor-beta and insulin-like growth factor-I in relation to diabetes-induced impairment of wound healing. The Journal of surgical research. 1996;61(1):113-9. doi: 10.1006/jsre.1996.0090. PubMed PMID: 8769952.

48. Singer AJ, Clark RA. Cutaneous wound healing. The New England journal of medicine. 1999;341(10):738-46. doi: 10.1056/NEJM199909023411006. PubMed PMID: 10471461.

49. Caskey RC, Zgheib C, Morris M, Allukian M, Dorsett-Martin W, Xu J, Wu W, Liechty KW. Dysregulation of collagen production in diabetes following recurrent skin injury: contribution to the development of a chronic wound. Wound repair and regeneration : official publication of the Wound Healing Society [and] the European Tissue Repair Society. 2014;22(4):515-20. doi: 10.1111/wrr.12199. PubMed PMID: 24898050.

50. Reddy GK. Comparison of the photostimulatory effects of visible He-Ne and infrared Ga-As lasers on healing impaired diabetic rat wounds. Lasers Surg Med. 2003;33(5):344-51. doi: 10.1002/lsm.10227. PubMed PMID: 14677162.

51. Reddy GK, Stehno-Bittel L, Enwemeka CS. Laser photostimulation accelerates wound healing in diabetic rats. Wound repair and regeneration : official publication of the Wound Healing Society [and] the European Tissue Repair Society. 2001;9(3):248-55. PubMed PMID: 11472621.

52. Hennessey PJ, Ford EG, Black CT, Andrassy RJ. Wound collagenase activity correlates directly with collagen glycosylation in diabetic rats. Journal of pediatric surgery. 1990;25(1):75-8. PubMed PMID: 2153794.

53. Bermudez DM, Herdrich BJ, Xu J, Lind R, Beason DP, Mitchell ME, Soslowsky LJ, Liechty KW. Impaired biomechanical properties of diabetic skin implications in pathogenesis of diabetic wound complications. The American journal of pathology. 2011;178(5):2215-23. doi: 10.1016/j.ajpath.2011.01.015. PubMed PMID: 21514435; PMCID: 3081147.

54. Phillips LG, Abdullah KM, Geldner PD, Dobbins S, Ko F, Linares HA, Broemeling LD, Robson MC. Application of basic fibroblast growth factor may reverse diabetic wound healing impairment. Annals of plastic surgery. 1993;31(4):331-4.

55. Edwards DR, Murphy G, Reynolds JJ, Whitham SE, Docherty AJ, Angel P, Heath JK. Transforming growth factor beta modulates the expression of collagenase and metalloproteinase inhibitor. EMBO J. 1987;6(7):1899-904. PubMed PMID: 2820711; PMCID: PMC553574.

56. Loots MA, Kenter SB, Au FL, Van Galen W, Middelkoop E, Bos JD, Mekkes JR. Fibroblasts derived from chronic diabetic ulcers differ in their response to stimulation with EGF, IGF-I, bFGF and PDGF-AB compared to controls. European journal of cell biology. 2002;81(3):153-60.

57. Loots MA, Lamme EN, Mekkes JR, Bos JD, Middelkoop E. Cultured fibroblasts from chronic diabetic wounds on the lower extremity (non-insulin-dependent diabetes mellitus) show disturbed proliferation. Archives of dermatological research. 1999;291(2-3):93-9. PubMed PMID: 10195396.

58. Hehenberger K, Kratz G, Hansson A, Brismar K. Fibroblasts derived from human chronic diabetic wounds have a decreased proliferation rate, which is recovered by the addition of heparin. Journal of dermatological science. 1998;16(2):144-51.

59. Black E, Vibe-Petersen J, Jorgensen LN, Madsen SM, Agren MS, Holstein PE, Perrild H, Gottrup F. Decrease of collagen deposition in wound repair in type 1 diabetes independent of glycemic control. Archives of surgery. 2003;138(1):34-40. PubMed PMID: 12511146.

60. Falanga V. Wound healing and its impairment in the diabetic foot. Lancet. 2005;366(9498):1736-43. doi: 10.1016/S0140-6736(05)67700-8. PubMed PMID: 16291068.

61. Liao H, Zakhaleva J, Chen W. Cells and tissue interactions with glycated collagen and their relevance to delayed diabetic wound healing. Biomaterials. 2009;30(9):1689-96. doi: 10.1016/j.biomaterials.2008.11.038. PubMed PMID: 19157537; PMCID: PMC2668700.

62. Armstrong DG, Jude EB. The role of matrix metalloproteinases in wound healing. J Am Podiatr Med Assoc. 2002;92(1):12-8. PubMed PMID: 11796794.

63. Sabino F, Hermes O, Egli FE, Kockmann T, Schlage P, Croizat P, Kizhakkedathu JN, Smola H, auf dem Keller U. In vivo assessment of protease dynamics in cutaneous wound healing by degradomics analysis of porcine wound exudates. Mol Cell Proteomics. 2015;14(2):354-70. doi: 10.1074/mcp.M114.043414. PubMed PMID: 25516628; PMCID: PMC4350031.

64. Neely AN, Clendening CE, Gardner J, Greenhalgh DG. Gelatinase activities in wounds of healing-impaired mice versus wounds of non-healing-impaired mice. J Burn Care Rehabil. 2000;21(5):395-402. PubMed PMID: 11020045.

65. Li Z, Guo S, Yao F, Zhang Y, Li T. Increased ratio of serum matrix metalloproteinase-9 against TIMP-1 predicts poor wound healing in diabetic foot ulcers. Journal of diabetes and its complications. 2013;27(4):380-2. doi: 10.1016/j.jdiacomp.2012.12.007. PubMed PMID: 23357650.

66. Muller M, Trocme C, Lardy B, Morel F, Halimi S, Benhamou PY. Matrix metalloproteinases and diabetic foot ulcers: the ratio of MMP-1 to TIMP-1 is a predictor of wound healing. Diabetic medicine : a journal of the British Diabetic Association. 2008;25(4):419-26. doi: 10.1111/j.1464-5491.2008.02414.x. PubMed PMID: 18387077; PMCID: 2326726.

67. Liu Y, Min D, Bolton T, Nube V, Twigg SM, Yue DK, McLennan SV. Increased matrix metalloproteinase-9 predicts poor wound healing in diabetic foot ulcers: Response to Muller et al. Diabetes care. 2009;32(11):e137. doi: 10.2337/dc09-1394. PubMed PMID: 19875600.

68. Lobmann R, Ambrosch A, Schultz G, Waldmann K, Schiweck S, Lehnert H. Expression of matrix-metalloproteinases and their inhibitors in the wounds of diabetic and non-diabetic patients. Diabetologia. 2002;45(7):1011-6. doi: 10.1007/s00125-002-0868-8. PubMed PMID: 12136400.

69. Signorelli SS, Malaponte G, Libra M, Di Pino L, Celotta G, Bevelacqua V, Petrina M, Nicotra GS, Indelicato M, Navolanic PM, Pennisi G, Mazzarino MC. Plasma levels and zymographic activities of matrix metalloproteinases 2 and 9 in type II diabetics with peripheral arterial disease. Vascular medicine. 2005;10(1):1-6. PubMed PMID: 15920993.

70. Singh K, Agrawal NK, Gupta SK, Mohan G, Chaturvedi S, Singh K. Differential Expression of Matrix Metalloproteinase-9 Gene in Wounds of Type 2 Diabetes Mellitus Cases With Susceptible -1562C>T Genotypes and Wound Severity. The international journal of lower extremity wounds. 2014;13(2):94-102. doi: 10.1177/1534734614534980. PubMed PMID: 24861096.

71. McLennan S, Min D, Yue D. Matrix metalloproteinases and their roles in poor wound healing in diabetes2008.

72. Singh K, Agrawal N, Gupta S, Singh K. A functional SNP-1562C> T in the matrix metalloproteinases-9 promoter is associated with type 2 diabetes and diabetic foot ulcers. The international journal of lower extremity wounds. 2013;12:199-204.

73. Singh K, Singh VK, Agrawal NK, Gupta SK, Singh K. Association of Toll-like receptor 4 polymorphisms with diabetic foot ulcers and application of artificial neural network in DFU risk assessment in type 2 diabetes patients. BioMed research international. 2013;2013:318686. doi: 10.1155/2013/318686. PubMed PMID: 23936790; PMCID: PMC3725976.

74. Liu Y, Min D, Bolton T, Nube V, Twigg SM, Yue DK, McLennan SV. Increased matrix metalloproteinase-9 predicts poor wound healing in diabetic foot ulcers. Diabetes care. 2009;32(1):117-9. doi: 10.2337/dc08-0763. PubMed PMID: 18835949; PMCID: PMC2606842.

75. Menghini R, Uccioli L, Vainieri E, Pecchioli C, Casagrande V, Stoehr R, Cardellini M, Porzio O, Rizza S, Federici M. Expression of tissue inhibitor of metalloprotease 3 is reduced in ischemic but not neuropathic ulcers from patients with type 2 diabetes mellitus. Acta diabetologica. 2013;50(6):907-10. doi: 10.1007/s00592-013-0478-6. PubMed PMID: 23636268.

76. Aparecida Da Silva A, Leal-Junior EC, Alves AC, Rambo CS, Dos Santos SA, Vieira RP, De Carvalho Pde T. Wound-healing effects of low-level laser therapy in diabetic rats involve the modulation of MMP-2 and MMP-9 and the redistribution of collagen types I and III. J Cosmet Laser Ther. 2013;15(4):210-6. doi: 10.3109/14764172.2012.761345. PubMed PMID: 23463906.

77. Gooyit M, Peng Z, Wolter WR, Pi H, Ding D, Hesek D, Lee M, Boggess B, Champion MM, Suckow MA, Mobashery S, Chang M. A chemical biological strategy to facilitate diabetic wound healing. ACS Chem Biol. 2014;9(1):105-10. doi: 10.1021/cb4005468. PubMed PMID: 24053680; PMCID: PMC3947039.

78. Li N, Luo H-C, Yang C, Deng J-J, Ren M, Xie X-Y, Lin D-Z, Yan L, Zhang L-M. Cationic star-shaped polymer as an siRNA carrier for reducing MMP-9 expression in skin fibroblast cells and promoting wound healing in diabetic rats. International journal of nanomedicine. 2014;9:3377.

79. Wong VW, Garg RK, Sorkin M, Rustad KC, Akaishi S, Levi K, Nelson ER, Tran M, Rennert R, Liu W, Longaker MT, Dauskardt RH, Gurtner GC. Loss of keratinocyte focal adhesion kinase stimulates dermal proteolysis through upregulation of MMP9 in wound healing. Ann Surg. 2014;260(6):1138-46. doi: 10.1097/SLA.0000000000000219. PubMed PMID: 25389925.

80. Lan CC, Liu IH, Fang AH, Wen CH, Wu CS. Hyperglycaemic conditions decrease cultured keratinocyte mobility: implications for impaired wound healing in patients with diabetes. The British journal of dermatology. 2008;159(5):1103-15. doi: 10.1111/j.1365-2133.2008.08789.x. PubMed PMID: 18717678.

81. Zhu P, Yang C, Chen LH, Ren M, Lao GJ, Yan L. Impairment of human keratinocyte mobility and proliferation by advanced glycation end products-modified BSA. Archives of dermatological research. 2011;303(5):339-50. doi: 10.1007/s00403-010-1102-z. PubMed PMID: 21132435.

82. Coultas L, Chawengsaksophak K, Rossant J. Endothelial cells and VEGF in vascular development. Nature. 2005;438(7070):937-45. doi: 10.1038/nature04479. PubMed PMID: 16355211.

83. Corral CJ, Siddiqui A, Wu L, Farrell CL, Lyons D, Mustoe TA. Vascular endothelial growth factor is more important than basic fibroblastic growth factor during ischemic wound healing. Archives of surgery. 1999;134(2):200-5. PubMed PMID: 10025464.

84. Brem H, Kodra A, Golinko MS, Entero H, Stojadinovic O, Wang VM, Sheahan CM, Weinberg AD, Woo SL, Ehrlich HP, Tomic-Canic M. Mechanism of sustained release of vascular endothelial growth factor in accelerating experimental diabetic healing. The Journal of investigative dermatology. 2009;129(9):2275-87. doi: 10.1038/jid.2009.26. PubMed PMID: 19282838.

85. Bao P, Kodra A, Tomic-Canic M, Golinko MS, Ehrlich HP, Brem H. The role of vascular endothelial growth factor in wound healing. The Journal of surgical research. 2009;153(2):347-58. doi: 10.1016/j.jss.2008.04.023. PubMed PMID: 19027922; PMCID: 2728016.

86. Stojadinovic O, Kodra A, Golinko M, Tomic-Canic M, Brem H, editors. A novel, non-angiogenic, mechanism of VEGF: Stimulation of keratinocyte and fibroblast migration. Wound Repair and Regeneration; 2007: BLACKWELL PUBLISHING 9600 GARSINGTON RD, OXFORD OX4 2DQ, OXON, ENGLAND.

87. Galiano RD, Tepper OM, Pelo CR, Bhatt KA, Callaghan M, Bastidas N, Bunting S, Steinmetz HG, Gurtner GC. Topical vascular endothelial growth factor accelerates diabetic wound healing through increased angiogenesis and by mobilizing and recruiting bone marrow-derived cells. The American journal of pathology. 2004;164(6):1935-47. doi: 10.1016/S0002-9440(10)63754-6. PubMed PMID: 15161630; PMCID: 1615774.

88. Losi P, Briganti E, Errico C, Lisella A, Sanguinetti E, Chiellini F, Soldani G. Fibrin-based scaffold incorporating VEGF- and bFGF-loaded nanoparticles stimulates wound healing in diabetic mice. Acta biomaterialia. 2013;9(8):7814-21. doi: 10.1016/j.actbio.2013.04.019. PubMed PMID: 23603001.

89. Saaristo A, Tammela T, Farkkila A, Karkkainen M, Suominen E, Yla-Herttuala S, Alitalo K. Vascular endothelial growth factor-C accelerates diabetic wound healing. The American journal of pathology. 2006;169(3):1080-7. doi: 10.2353/ajpath.2006.051251. PubMed PMID: 16936280; PMCID: PMC1698814.

90. Romano Di Peppe S, Mangoni A, Zambruno G, Spinetti G, Melillo G, Napolitano M, Capogrossi MC. Adenovirus-mediated VEGF(165) gene transfer enhances wound healing by promoting angiogenesis in CD1 diabetic mice. Gene Ther. 2002;9(19):1271-7. doi: 10.1038/sj.gt.3301798. PubMed PMID: 12224009.

91. Yoon CS, Jung HS, Kwon MJ, Lee SH, Kim CW, Kim MK, Lee M, Park JH. Sonoporation of the minicircle-VEGF(165) for wound healing of diabetic mice. Pharmaceutical research. 2009;26(4):794-801. doi: 10.1007/s11095-008-9778-x. PubMed PMID: 18998201.

92. Kusumanto YH, van Weel V, Mulder NH, Smit AJ, van den Dungen JJ, Hooymans JM, Sluiter WJ, Tio RA, Quax PH, Gans RO, Dullaart RP, Hospers GA. Treatment with intramuscular vascular endothelial growth factor gene compared with placebo for patients with diabetes mellitus and critical limb ischemia: a double-blind randomized trial. Hum Gene Ther. 2006;17(6):683-91. doi: 10.1089/hum.2006.17.683. PubMed PMID: 16776576.

93. Hopkins SP, Bulgrin JP, Sims RL, Bowman B, Donovan DL, Schmidt SP. Controlled delivery of vascular endothelial growth factor promotes neovascularization and maintains limb function in a rabbit model of ischemia. Journal of vascular surgery. 1998;27(5):886-94; discussion 95. PubMed PMID: 9620141.

94. Kryger Z, Zhang F, Dogan T, Cheng C, Lineaweaver WC, Buncke HJ. The effects of VEGF on survival of a random flap in the rat: examination of various routes of administration. British journal of plastic surgery. 2000;53(3):234-9. doi: 10.1054/bjps.1999.3315. PubMed PMID: 10738331.

95. Fang RC, Galiano RD. A review of becaplermin gel in the treatment of diabetic neuropathic foot ulcers. Biologics : targets & therapy. 2008;2(1):1-12. PubMed PMID: 19707423; PMCID: 2727777.

96. Lee S, Jilani SM, Nikolova GV, Carpizo D, Iruela-Arispe ML. Processing of VEGF-A by matrix metalloproteinases regulates bioavailability and vascular patterning in tumors. The Journal of cell biology. 2005;169(4):681-91. doi: 10.1083/jcb.200409115. PubMed PMID: 15911882; PMCID: 2171712.

97. Crawford TN, Alfaro DV, 3rd, Kerrison JB, Jablon EP. Diabetic retinopathy and angiogenesis. Current diabetes reviews. 2009;5(1):8-13. PubMed PMID: 19199892.

98. Akimoto M, Takeda A, Matsushita O, Inoue J, Sakamoto K, Hattori M, Kounoike N, Uchinuma E. Effects of CB-VEGF-A injection in rat flap models for improved survival. Plastic and reconstructive surgery. 2013;131(4):717-25. doi: 10.1097/PRS.0b013e3182818b34. PubMed PMID: 23542245.

99. Tan Q, Chen B, Yan X, Lin Y, Xiao Z, Hou X, Dai J. Promotion of diabetic wound healing by collagen scaffold with collagen-binding vascular endothelial growth factor in a diabetic rat model. J Tissue Eng Regen Med. 2014;8(3):195-201. doi: 10.1002/term.1513. PubMed PMID: 22570298.

100. Yan X, Chen B, Lin Y, Li Y, Xiao Z, Hou X, Tan Q, Dai J. Acceleration of diabetic wound healing by collagen-binding vascular endothelial growth factor in diabetic rat model. Diabetes research and clinical practice. 2010;90(1):66-72. Epub 2010/07/30. doi: 10.1016/j.diabres.2010.07.001. PubMed PMID: 20667614.

101. Martino MM, Briquez PS, Guc E, Tortelli F, Kilarski WW, Metzger S, Rice JJ, Kuhn GA, Muller R, Swartz MA, Hubbell JA. Growth factors engineered for super-affinity to the extracellular matrix enhance tissue healing. Science. 2014;343(6173):885-8. doi: 10.1126/science.1247663. PubMed PMID: 24558160.

102. Martino MM, Tortelli F, Mochizuki M, Traub S, Ben-David D, Kuhn GA, Muller R, Livne E, Eming SA, Hubbell JA. Engineering the growth factor microenvironment with fibronectin domains to promote wound and bone tissue healing. Science translational medicine. 2011;3(100):100ra89. doi: 10.1126/scitranslmed.3002614. PubMed PMID: 21918106.

103. Eaglstein WH, Kirsner RS, Robson MC. Food and Drug Administration (FDA) drug approval end points for chronic cutaneous ulcer studies. Wound repair and regeneration : official publication of the Wound Healing Society [and] the European Tissue Repair Society. 2012;20(6):793-6. doi: 10.1111/j.1524-475X.2012.00849.x. PubMed PMID: 23126458.

104. Hanft JR, Pollak RA, Barbul A, van Gils C, Kwon PS, Gray SM, Lynch CJ, Semba CP, Breen TJ. Phase I trial on the safety of topical rhVEGF on chronic neuropathic diabetic foot ulcers. J Wound Care. 2008;17(1):30-2, 4-7. doi: 10.12968/jowc.2008.17.1.27917. PubMed PMID: 18210954.

105. Barrientos S, Brem H, Stojadinovic O, Tomic-Canic M. Clinical application of growth factors and cytokines in wound healing. Wound repair and regeneration : official publication of the Wound Healing Society [and] the European Tissue Repair Society. 2014;22(5):569-78. doi: 10.1111/wrr.12205. PubMed PMID: 24942811.

106. Chen SM, Ward SI, Olutoye OO, Diegelmann RF, Kelman Cohen I. Ability of chronic wound fluids to degrade peptide growth factors is associated with increased levels of elastase activity and diminished levels of proteinase inhibitors. Wound repair and regeneration : official publication of the Wound Healing Society [and] the European Tissue Repair Society. 1997;5(1):23-32. doi: 10.1046/j.1524-475X.1997.50108.x. PubMed PMID: 16984454.

107. Futrega K, King M, Lott WB, Doran MR. Treating the whole not the hole: necessary coupling of technologies for diabetic foot ulcer treatment. Trends in molecular medicine. 2014;20(3):137-42.

108. Bartlett RL, 2nd, Medow MR, Panitch A, Seal B. Hemocompatible poly(NIPAm-MBA-AMPS) colloidal nanoparticles as carriers of anti-inflammatory cell penetrating peptides. Biomacromolecules. 2012;13(4):1204-11. Epub 2012/03/29. doi: 10.1021/bm300173x. PubMed PMID: 22452800.

109. Bartlett RL, 2nd, Panitch A. Thermosensitive nanoparticles with pH-triggered degradation and release of anti-inflammatory cell-penetrating peptides. Biomacromolecules. 2012;13(8):2578-84. Epub 2012/08/03. doi: 10.1021/bm300826v. PubMed PMID: 22852804.

110. Bartlett RL, 2nd, Sharma S, Panitch A. Cell-penetrating peptides released from thermosensitive nanoparticles suppress pro-inflammatory cytokine response by specifically targeting inflamed cartilage explants. Nanomedicine : nanotechnology, biology, and medicine. 2013;9(3):419-27. doi: 10.1016/j.nano.2012.09.003. PubMed PMID: 23041412; PMCID: 4006693.

111. Lin JB, Poh S, Panitch A. Controlled release of anti-inflammatory peptides from reducible thermosensitive nanoparticles suppresses cartilage inflammation. Nanomedicine : nanotechnology, biology, and medicine. 2016;12(7):2095-100. doi: 10.1016/j.nano.2016.05.010. PubMed PMID: 27241526; PMCID: PMC5065746.

112. McMasters J, Poh S, Lin JB, Panitch A. Delivery of anti-inflammatory peptides from hollow PEGylated poly(NIPAM) nanoparticles reduces inflammation in an ex vivo osteoarthritis model. J Control Release. 2017;258:161-70. doi: 10.1016/j.jconrel.2017.05.008. PubMed PMID: 28495577; PMCID: PMC5535751.

113. Poh S, Lin JB, Panitch A. Release of anti-inflammatory peptides from thermosensitive nanoparticles with degradable cross-links suppresses pro-inflammatory cytokine production. Biomacromolecules. 2015;16(4):1191-200. doi: 10.1021/bm501849p. PubMed PMID: 25728363.

114. McMasters J, Panitch A. Prevention of Collagen-Induced Platelet Binding and Activation by Thermosensitive Nanoparticles. AAPS J. 2015;17(5):1117-25. doi: 10.1208/s12248-015-9794-9. PubMed PMID: 26070443; PMCID: PMC4540739.

115. McMasters J, Panitch A. Collagen-binding nanoparticles for extracellular anti-inflammatory peptide delivery decrease platelet activation, promote endothelial migration, and suppress inflammation. Acta biomaterialia. 2017;49:78-88. doi: 10.1016/j.actbio.2016.11.023. PubMed PMID: 27840254; PMCID: PMC5253112.

116. Stuart K, Paderi J, Snyder PW, Freeman L, Panitch A. Collagen-binding peptidoglycans inhibit MMP mediated collagen degradation and reduce dermal scarring. PloS one. 2011;6(7):e22139. doi: 10.1371/journal.pone.0022139. PubMed PMID: 21779387; PMCID: 3133773.

117. Brugnano JL, Chan BK, Seal BL, Panitch A. Cell-penetrating peptides can confer biological function: regulation of inflammatory cytokines in human monocytes by MK2 inhibitor peptides. Journal of Controlled Release. 2011;155(2):128-33.

118. Lyon LA, Meng Z, Singh N, Sorrell CD, John AS. Thermoresponsive microgel-based materials. Chemical Society Reviews. 2009;38(4):865-74.

119. Karg M, Hellweg T. New “smart” poly (NIPAM) microgels and nanoparticle microgel hybrids: properties and advances in characterisation. Current Opinion in Colloid & Interface Science. 2009;14(6):438-50.

120. Schmaljohann D. Thermo- and pH-responsive polymers in drug delivery. Adv Drug Deliv Rev. 2006;58(15):1655-70. doi: 10.1016/j.addr.2006.09.020. PubMed PMID: 17125884.

121. Gulati N, Rastogi R, Dinda AK, Saxena R, Koul V. Characterization and cell material interactions of PEGylated PNIPAAM nanoparticles. Colloids and surfaces B, Biointerfaces. 2010;79(1):164-73. Epub 2010/05/08. doi: 10.1016/j.colsurfb.2010.03.049. PubMed PMID: 20447809.

122. Tenuta T, Monopoli MP, Kim J, Salvati A, Dawson KA, Sandin P, Lynch I. Elution of labile fluorescent dye from nanoparticles during biological use. PloS one. 2011;6(10):e25556. doi: 10.1371/journal.pone.0025556. PubMed PMID: 21998668; PMCID: PMC3188558.

123. Van Manen MD, Nace J, Mont MA. Management of primary knee osteoarthritis and indications for total knee arthroplasty for general practitioners. J Am Osteopath Assoc. 2012;112(11):709-15. Epub 2012/11/10. PubMed PMID: 23139341.

124. Berenbaum F. Osteoarthritis as an inflammatory disease (osteoarthritis is not osteoarthrosis!). Osteoarthritis Cartilage. 2013;21(1):16-21. Epub 2012/12/01. doi: 10.1016/j.joca.2012.11.012. PubMed PMID: 23194896.

125. Prevalence of disabilities and associated health conditions among adults--United States, 1999. MMWR Morb Mortal Wkly Rep. 2001;50(7):120-5. Epub 2001/06/08. PubMed PMID: 11393491.

126. Daghestani HN, Pieper CF, Kraus VB. Soluble macrophage biomarkers indicate inflammatory phenotypes in patients with knee osteoarthritis. Arthritis Rheumatol. 2015;67(4):956-65. Epub 2014/12/30. doi: 10.1002/art.39006. PubMed PMID: 25544994.

127. Pelletier JP, Martel-Pelletier J, Abramson SB. Osteoarthritis, an inflammatory disease: potential implication for the selection of new therapeutic targets. Arthritis Rheum. 2001;44(6):1237-47. Epub 2001/06/16. doi: 10.1002/1529-0131(200106)44:6<1237::aid-art214>3.0.co;2-f. PubMed PMID: 11407681.

128. Arner EC, Hughes CE, Decicco CP, Caterson B, Tortorella MD. Cytokine-induced cartilage proteoglycan degradation is mediated by aggrecanase. Osteoarthritis and cartilage. 1998;6(3):214-28.

129. Pratta MA, Yao W, Decicco C, Tortorella MD, Liu RQ, Copeland RA, Magolda R, Newton RC, Trzaskos JM, Arner EC. Aggrecan protects cartilage collagen from proteolytic cleavage. J Biol Chem. 2003;278(46):45539-45. Epub 2003/08/02. doi: 10.1074/jbc.M303737200. PubMed PMID: 12890681.

130. Roux PP, Blenis J. ERK and p38 MAPK-activated protein kinases: a family of protein kinases with diverse biological functions. Microbiology and molecular biology reviews. 2004;68(2):320-44.

131. Engel K, Ahlers A, Brach MA, Herrmann F, Gaestel M. MAPKAP kinase 2 is activated by heat shock and TNF-α: In vivo phosphorylation of small heat shock protein results from stimulation of the MAP kinase cascade. Journal of cellular biochemistry. 1995;57(2):321-30.

132. Belka C, Ahlers A, Sott C, Gaestel M, Herrmann F, Brach M. Interleukin (IL)-6 signaling leads to phosphorylation of the small heat shock protein (Hsp) 27 through activation of the MAP kinase and MAPKAP kinase 2 pathway in monocytes and monocytic leukemia cells. Leukemia. 1995;9(2):288-94.

133. Craik DJ, Fairlie DP, Liras S, Price D. The future of peptide-based drugs. Chemical biology & drug design. 2013;81(1):136-47.

134. Niikura T, Reddi AH. Differential regulation of lubricin/superficial zone protein by transforming growth factor beta/bone morphogenetic protein superfamily members in articular chondrocytes and synoviocytes. Arthritis Rheum. 2007;56(7):2312-21. doi: 10.1002/art.22659. PubMed PMID: 17599751.

135. Poole AR, Pidoux I, Reiner A, Tang LH, Choi H, Rosenberg L. Localization of proteoglycan monomer and link protein in the matrix of bovine articular cartilage: An immunohistochemical study. J Histochem Cytochem. 1980;28(7):621-35. Epub 1980/07/01. PubMed PMID: 6156200.

136. Zhao X, Yu SB, Wu FL, Mao ZB, Yu CL. Transfection of primary chondrocytes using chitosan-pEGFP nanoparticles. J Control Release. 2006;112(2):223-8. doi: 10.1016/j.jconrel.2006.01.016. PubMed PMID: 16556468.

137. Ramaswamy S, Greco JB, Uluer MC, Zhang Z, Fishbein KW, Spencer RG. Magnetic resonance imaging of chondrocytes labeled with superparamagnetic iron oxide nanoparticles in tissue-engineered cartilage. Tissue Eng Part A. 2009;15(12):3899-910. doi: 10.1089/ten.tea.2008.0677. PubMed PMID: 19788362; PMCID: PMC2792067.

138. Chen J, Wang F, Zhang Y, Jin X, Zhang L, Feng Y, Lin X, Yang L. In vivo tracking of superparamagnetic iron oxide nanoparticle labeled chondrocytes in large animal model. Ann Biomed Eng. 2012;40(12):2568-78. doi: 10.1007/s10439-012-0621-5. PubMed PMID: 22810839.

139. Park JS, Yang HN, Jeon SY, Woo DG, Kim MS, Park KH. The use of anti-COX2 siRNA coated onto PLGA nanoparticles loading dexamethasone in the treatment of rheumatoid arthritis. Biomaterials. 2012;33(33):8600-12. doi: 10.1016/j.biomaterials.2012.08.008. PubMed PMID: 22910222.

140. Greener B, Hughes AA, Bannister NP, Douglass J. Proteases and pH in chronic wounds. J Wound Care. 2005;14(2):59-61. doi: 10.12968/jowc.2005.14.2.26739. PubMed PMID: 15739652.

141. Schneider LA, Korber A, Grabbe S, Dissemond J. Influence of pH on wound-healing: a new perspective for wound-therapy? Archives of dermatological research. 2007;298(9):413-20. doi: 10.1007/s00403-006-0713-x. PubMed PMID: 17091276.

142. Wilson IA, Henry M, Quill RD, Byrne PJ. The pH of varicose ulcer surfaces and its relationship to healing. Vasa. 1979;8(4):339-42. PubMed PMID: 44410.

143. Sayegh N, Dawson J, Bloom N, Stahl W. Wound pH as a predictor of skin graft survival. Curr Surg. 1988;45(1):23-4. PubMed PMID: 3278864.

144. Reed CC, Iozzo RV. The role of decorin in collagen fibrillogenesis and skin homeostasis. Glycoconjugate journal. 2002;19(4-5):249-55. doi: 10.1023/A:1025383913444. PubMed PMID: 12975602.

145. Vogel KG, Trotter JA. The effect of proteoglycans on the morphology of collagen fibrils formed in vitro. Collagen and related research. 1987;7(2):105-14. PubMed PMID: 3621881.

146. Danielson KG, Baribault H, Holmes DF, Graham H, Kadler KE, Iozzo RV. Targeted disruption of decorin leads to abnormal collagen fibril morphology and skin fragility. The Journal of cell biology. 1997;136(3):729-43. PubMed PMID: 9024701; PMCID: 2134287.

147. Scott PG, Dodd CM, Tredget EE, Ghahary A, Rahemtulla F. Chemical characterization and quantification of proteoglycans in human post-burn hypertrophic and mature scars. Clinical science. 1996;90(5):417-25. PubMed PMID: 8665780.

148. Paderi JE, Panitch A. Design of a synthetic collagen-binding peptidoglycan that modulates collagen fibrillogenesis. Biomacromolecules. 2008;9(9):2562-6. doi: 10.1021/bm8006852. PubMed PMID: 18680341.

149. Hao D, Xiao W, Liu R, Kumar P, Li Y, Zhou P, Guo F, Farmer DL, Lam KS, Wang F, Wang A. Discovery and Characterization of a Potent and Specific Peptide Ligand Targeting Endothelial Progenitor Cells and Endothelial Cells for Tissue Regeneration. ACS Chem Biol. 2017;12(4):1075-86. doi: 10.1021/acschembio.7b00118. PubMed PMID: 28195700.

150. Wang Y, Xiao W, Zhang Y, Meza L, Tseng H, Takada Y, Ames JB, Lam KS. Optimization of RGD-Containing Cyclic Peptides against alphavbeta3 Integrin. Mol Cancer Ther. 2016;15(2):232-40. doi: 10.1158/1535-7163.MCT-15-0544. PubMed PMID: 26719578; PMCID: PMC4747864.

151. Plichta JK, Radek KA. Sugar-coating wound repair: a review of FGF-10 and dermatan sulfate in wound healing and their potential application in burn wounds. Journal of burn care & research : official publication of the American Burn Association. 2012;33(3):299-310. doi: 10.1097/BCR.0b013e318240540a. PubMed PMID: 22561305; PMCID: 3348504.

152. Trowbridge JM, Rudisill JA, Ron D, Gallo RL. Dermatan sulfate binds and potentiates activity of keratinocyte growth factor (FGF-7). The Journal of biological chemistry. 2002;277(45):42815-20. doi: 10.1074/jbc.M204959200. PubMed PMID: 12215437.

153. Penc SF, Pomahac B, Winkler T, Dorschner RA, Eriksson E, Herndon M, Gallo RL. Dermatan sulfate released after injury is a potent promoter of fibroblast growth factor-2 function. The Journal of biological chemistry. 1998;273(43):28116-21. PubMed PMID: 9774430.

154. Robinson CJ, Mulloy B, Gallagher JT, Stringer SE. VEGF165-binding sites within heparan sulfate encompass two highly sulfated domains and can be liberated by K5 lyase. The Journal of biological chemistry. 2006;281(3):1731-40. doi: 10.1074/jbc.M510760200. PubMed PMID: 16258170.

155. Peters MC, Isenberg BC, Rowley JA, Mooney DJ. Release from alginate enhances the biological activity of vascular endothelial growth factor. J Biomater Sci Polym Ed. 1998;9(12):1267-78. PubMed PMID: 9860169.

156. Chen TT, Luque A, Lee S, Anderson SM, Segura T, Iruela-Arispe ML. Anchorage of VEGF to the extracellular matrix conveys differential signaling responses to endothelial cells. The Journal of cell biology. 2010;188(4):595-609. doi: 10.1083/jcb.200906044. PubMed PMID: 20176926; PMCID: PMC2828913.

157. Teran M, Nugent MA. Synergistic Binding of Vascular Endothelial Growth Factor-A and Its Receptors to Heparin Selectively Modulates Complex Affinity. The Journal of biological chemistry. 2015;290(26):16451-62. doi: 10.1074/jbc.M114.627372. PubMed PMID: 25979342; PMCID: PMC4481241.

158. Gitay-Goren H, Soker S, Vlodavsky I, Neufeld G. The binding of vascular endothelial growth factor to its receptors is dependent on cell surface-associated heparin-like molecules. The Journal of biological chemistry. 1992;267(9):6093-8. PubMed PMID: 1556117.

159. D'Andrea LD, Iaccarino G, Fattorusso R, Sorriento D, Carannante C, Capasso D, Trimarco B, Pedone C. Targeting angiogenesis: structural characterization and biological properties of a de novo engineered VEGF mimicking peptide. Proceedings of the National Academy of Sciences of the United States of America. 2005;102(40):14215-20. doi: 10.1073/pnas.0505047102. PubMed PMID: 16186493; PMCID: 1242306.

160. Finetti F, Basile A, Capasso D, Di Gaetano S, Di Stasi R, Pascale M, Turco CM, Ziche M, Morbidelli L, D'Andrea LD. Functional and pharmacological characterization of a VEGF mimetic peptide on reparative angiogenesis. Biochemical pharmacology. 2012;84(3):303-11. doi: 10.1016/j.bcp.2012.04.011. PubMed PMID: 22554565.

161. Santulli G, Ciccarelli M, Palumbo G, Campanile A, Galasso G, Ziaco B, Altobelli GG, Cimini V, Piscione F, D'Andrea LD, Pedone C, Trimarco B, Iaccarino G. In vivo properties of the proangiogenic peptide QK. Journal of translational medicine. 2009;7:41. Epub 2009/06/10. doi: 10.1186/1479-5876-7-41. PubMed PMID: 19505323; PMCID: 2702279.

162. Wang L, Zhao M, Li S, Erasquin UJ, Wang H, Ren L, Chen C, Wang Y, Cai C. "Click" immobilization of a VEGF-mimetic peptide on decellularized endothelial extracellular matrix to enhance angiogenesis. ACS applied materials & interfaces. 2014;6(11):8401-6. Epub 2014/04/23. doi: 10.1021/am501309d. PubMed PMID: 24749832; PMCID: 4059262.

163. Leslie-Barbick JE, Saik JE, Gould DJ, Dickinson ME, West JL. The promotion of microvasculature formation in poly(ethylene glycol) diacrylate hydrogels by an immobilized VEGF-mimetic peptide. Biomaterials. 2011;32(25):5782-9. Epub 2011/05/27. doi: 10.1016/j.biomaterials.2011.04.060. PubMed PMID: 21612821.

164. Webber MJ, Tongers J, Newcomb CJ, Marquardt K-T, Bauersachs J, Losordo DW, Stupp SI. Supramolecular nanostructures that mimic VEGF as a strategy for ischemic tissue repair. Proceedings of the National Academy of Sciences. 2011;108(33):13438-43.

165. Chan TR, Stahl PJ, Yu SM. Matrix-Bound VEGF Mimetic Peptides: Design and Endothelial Cell Activation in Collagen Scaffolds. Adv Funct Mater. 2011;21(22):4252-62. doi: 10.1002/adfm.201101163. PubMed PMID: 26312060; PMCID: PMC4547390.

166. Cai L, Dinh CB, Heilshorn SC. One-pot Synthesis of Elastin-like Polypeptide Hydrogels with Grafted VEGF-Mimetic Peptides. Biomaterials science. 2014;2(5):757-65. Epub 2014/04/15. doi: 10.1039/C3BM60293A. PubMed PMID: 24729868; PMCID: 3979545.

167. Byzova TV, Goldman CK, Pampori N, Thomas KA, Bett A, Shattil SJ, Plow EF. A mechanism for modulation of cellular responses to VEGF: activation of the integrins. Mol Cell. 2000;6(4):851-60. PubMed PMID: 11090623.

168. Eliceiri BP, Cheresh DA. Role of alpha v integrins during angiogenesis. Cancer J. 2000;6 Suppl 3:S245-9. PubMed PMID: 10874494.

169. Shattil SJ, Ginsberg MH. Integrin signaling in vascular biology. The Journal of clinical investigation. 1997;100(11 Suppl):S91-5. PubMed PMID: 9413409.

170. Mahabeleshwar GH, Feng W, Reddy K, Plow EF, Byzova TV. Mechanisms of integrin-vascular endothelial growth factor receptor cross-activation in angiogenesis. Circulation research. 2007;101(6):570-80. doi: 10.1161/CIRCRESAHA.107.155655. PubMed PMID: 17641225; PMCID: PMC2723825.

171. Soldi R, Mitola S, Strasly M, Defilippi P, Tarone G, Bussolino F. Role of alphavbeta3 integrin in the activation of vascular endothelial growth factor receptor-2. EMBO J. 1999;18(4):882-92. doi: 10.1093/emboj/18.4.882. PubMed PMID: 10022831; PMCID: PMC1171181.

172. Brooks PC, Stromblad S, Sanders LC, von Schalscha TL, Aimes RT, Stetler-Stevenson WG, Quigley JP, Cheresh DA. Localization of matrix metalloproteinase MMP-2 to the surface of invasive cells by interaction with integrin alpha v beta 3. Cell. 1996;85(5):683-93. PubMed PMID: 8646777.

173. Stromblad S, Becker JC, Yebra M, Brooks PC, Cheresh DA. Suppression of p53 activity and p21WAF1/CIP1 expression by vascular cell integrin alphaVbeta3 during angiogenesis. The Journal of clinical investigation. 1996;98(2):426-33. doi: 10.1172/JCI118808. PubMed PMID: 8755653; PMCID: PMC507446.

174. Somanath PR, Malinin NL, Byzova TV. Cooperation between integrin alphavbeta3 and VEGFR2 in angiogenesis. Angiogenesis. 2009;12(2):177-85. doi: 10.1007/s10456-009-9141-9. PubMed PMID: 19267251; PMCID: PMC2863048.

175. Zhou D. FT, Lu L., Wu J., Tong X., Yi L. Administration of LXW7 following transient cerebral ischemic stroke confers neuroprotection in rats. Int J Clin Exp Med. 2017;10(1):455-66. Epub January 15, 2017.

176. Fang T, Zhou D, Lu L, Tong X, Wu J, Yi L. LXW7 ameliorates focal cerebral ischemia injury and attenuates inflammatory responses in activated microglia in rats. Braz J Med Biol Res. 2016;49(9):e5287. doi: 10.1590/1414-431X20165287. PubMed PMID: 27533766; PMCID: PMC4988477.

177. Bauer SM, Goldstein LJ, Bauer RJ, Chen H, Putt M, Velazquez OC. The bone marrow-derived endothelial progenitor cell response is impaired in delayed wound healing from ischemia. Journal of vascular surgery. 2006;43(1):134-41. doi: 10.1016/j.jvs.2005.08.038. PubMed PMID: 16414400.

178. Zheng JS, Tang S, Qi YK, Wang ZP, Liu L. Chemical synthesis of proteins using peptide hydrazides as thioester surrogates. Nature protocols. 2013;8(12):2483-95. doi: 10.1038/nprot.2013.152. PubMed PMID: 24232250.

179. Totaro KA, Liao X, Bhattacharya K, Finneman JI, Sperry JB, Massa MA, Thorn J, Ho SV, Pentelute BL. Systematic Investigation of EDC/sNHS-Mediated Bioconjugation Reactions for Carboxylated Peptide Substrates. Bioconjug Chem. 2016;27(4):994-1004. doi: 10.1021/acs.bioconjchem.6b00043. PubMed PMID: 26974183.

180. D'Este M, Eglin D, Alini M. A systematic analysis of DMTMM vs EDC/NHS for ligation of amines to hyaluronan in water. Carbohydr Polym. 2014;108:239-46. doi: 10.1016/j.carbpol.2014.02.070. PubMed PMID: 24751270.

181. Loebel C, D'Este M, Alini M, Zenobi-Wong M, Eglin D. Precise tailoring of tyramine-based hyaluronan hydrogel properties using DMTMM conjugation. Carbohydr Polym. 2015;115:325-33. doi: 10.1016/j.carbpol.2014.08.097. PubMed PMID: 25439901.

182. Wijelath E, Namekata M, Murray J, Furuyashiki M, Zhang S, Coan D, Wakao M, Harris RB, Suda Y, Wang L, Sobel M. Multiple mechanisms for exogenous heparin modulation of vascular endothelial growth factor activity. Journal of cellular biochemistry. 2010;111(2):461-8. doi: 10.1002/jcb.22727. PubMed PMID: 20524207; PMCID: PMC3175432.

183. Thevenet P, Shen Y, Maupetit J, Guyon F, Derreumaux P, Tuffery P. PEP-FOLD: an updated de novo structure prediction server for both linear and disulfide bonded cyclic peptides. Nucleic acids research. 2012;40(Web Server issue):W288-93. doi: 10.1093/nar/gks419. PubMed PMID: 22581768; PMCID: 3394260.

184. Shen Y, Maupetit J, Derreumaux P, Tuffery P. Improved PEP-FOLD Approach for Peptide and Miniprotein Structure Prediction. J Chem Theory Comput. 2014;10(10):4745-58. doi: 10.1021/ct500592m. PubMed PMID: 26588162.

185. Greenfield NJ. Using circular dichroism spectra to estimate protein secondary structure. Nature protocols. 2006;1(6):2876-90. doi: 10.1038/nprot.2006.202. PubMed PMID: 17406547; PMCID: PMC2728378.

186. Nakajima N, Ikada Y. Mechanism of amide formation by carbodiimide for bioconjugation in aqueous media. Bioconjug Chem. 1995;6(1):123-30. PubMed PMID: 7711098.

187. Pouyani T, Kuo JW, Harbison GS, Prestwich GD. Solid-state NMR of N-acylureas derived from the reaction of hyaluronic acid with isotopically-labeled carbodiimides. Journal of the American Chemical Society. 1992;114(15):5972-6. doi: 10.1021/ja00041a010.

188. Huckett B, Gordhan H, Hawtrey R, Moodley N, Ariatti M, Hawtrey A. Binding of DNA to albumin and transferrin modified by treatment with water-soluble carbodiimides. Biochemical pharmacology. 1986;35(8):1249-57. PubMed PMID: 3964300.

189. Oliveira GB, Carvalho LB, Jr., Silva MP. Properties of carbodiimide treated heparin. Biomaterials. 2003;24(26):4777-83. PubMed PMID: 14530075.

190. Scott RA, Ramaswamy AK, Park K, Panitch A. Decorin mimic promotes endothelial cell health in endothelial monolayers and endothelial-smooth muscle co-cultures. J Tissue Eng Regen Med. 2015. doi: 10.1002/term.2035. PubMed PMID: 26033955.

191. Paderi JE, Stuart K, Sturek M, Park K, Panitch A. The inhibition of platelet adhesion and activation on collagen during balloon angioplasty by collagen-binding peptidoglycans. Biomaterials. 2011;32(10):2516-23. doi: 10.1016/j.biomaterials.2010.12.025. PubMed PMID: 21216002.

192. Li J, Chen J, Kirsner R. Pathophysiology of acute wound healing. Clin Dermatol. 2007;25(1):9-18. doi: 10.1016/j.clindermatol.2006.09.007. PubMed PMID: 17276196.

193. Tollefsen DM, Peacock ME, Monafo WJ. Molecular size of dermatan sulfate oligosaccharides required to bind and activate heparin cofactor II. The Journal of biological chemistry. 1986;261(19):8854-8. PubMed PMID: 3755134.

194. Tovar AM, de Mattos DA, Stelling MP, Sarcinelli-Luz BS, Nazareth RA, Mourao PA. Dermatan sulfate is the predominant antithrombotic glycosaminoglycan in vessel walls: implications for a possible physiological function of heparin cofactor II. Biochim Biophys Acta. 2005;1740(1):45-53. doi: 10.1016/j.bbadis.2005.02.008. PubMed PMID: 15878740.

195. Mulloy B, Mourao PA, Gray E. Structure/function studies of anticoagulant sulphated polysaccharides using NMR. J Biotechnol. 2000;77(1):123-35. PubMed PMID: 10674219.

196. Saito A, Munakata H. Analysis of plasma proteins that bind to glycosaminoglycans. Biochim Biophys Acta. 2007;1770(2):241-6. doi: 10.1016/j.bbagen.2006.10.015. PubMed PMID: 17178194.

197. Zammit A, Dawes J. Fibrinogen inhibits the heparin cofactor II-mediated antithrombin activity of dermatan sulfate. Blood. 1995;85(3):720-6. PubMed PMID: 7833476.

198. Sawano A, Takahashi T, Yamaguchi S, Aonuma M, Shibuya M. Flt-1 but not KDR/Flk-1 tyrosine kinase is a receptor for placenta growth factor, which is related to vascular endothelial growth factor. Cell Growth Differ. 1996;7(2):213-21. PubMed PMID: 8822205.

199. Koepsel JT, Nguyen EH, Murphy WL. Differential effects of a soluble or immobilized VEGFR-binding peptide. Integr Biol (Camb). 2012;4(8):914-24. doi: 10.1039/c2ib20055d. PubMed PMID: 22733256; PMCID: PMC3415255.

200. Olsson AK, Dimberg A, Kreuger J, Claesson-Welsh L. VEGF receptor signalling - in control of vascular function. Nat Rev Mol Cell Biol. 2006;7(5):359-71. doi: 10.1038/nrm1911. PubMed PMID: 16633338.

201. Shibuya M. Vascular Endothelial Growth Factor (VEGF) and Its Receptor (VEGFR) Signaling in Angiogenesis: A Crucial Target for Anti- and Pro-Angiogenic Therapies. Genes Cancer. 2011;2(12):1097-105. doi: 10.1177/1947601911423031. PubMed PMID: 22866201; PMCID: PMC3411125.

202. Xiao W, Wang Y, Lau EY, Luo J, Yao N, Shi C, Meza L, Tseng H, Maeda Y, Kumaresan P, Liu R, Lightstone FC, Takada Y, Lam KS. The use of one-bead one-compound combinatorial library technology to discover high-affinity alphavbeta3 integrin and cancer targeting arginine-glycine-aspartic acid ligands with a built-in handle. Mol Cancer Ther. 2010;9(10):2714-23. doi: 10.1158/1535-7163.MCT-10-0308. PubMed PMID: 20858725; PMCID: PMC3571112.

203. Kumar CC, Armstrong L, Yin Z, Malkowski M, Maxwell E, Ling H, Yaremko B, Liu M, Varner J, Smith EM, Neustadt B, Nechuta T. Targeting integrins alpha v beta 3 and alpha v beta 5 for blocking tumor-induced angiogenesis. Adv Exp Med Biol. 2000;476:169-80. PubMed PMID: 10949664.

204. Tucker GC. Integrins: molecular targets in cancer therapy. Curr Oncol Rep. 2006;8(2):96-103. PubMed PMID: 16507218.

205. Niemisto A, Dunmire V, Yli-Harja O, Zhang W, Shmulevich I. Robust quantification of in vitro angiogenesis through image analysis. IEEE Trans Med Imaging. 2005;24(4):549-53. PubMed PMID: 15822812.

206. Williams PA, Campbell KT, Gharaviram H, Madrigal JL, Silva EA. Alginate-Chitosan Hydrogels Provide a Sustained Gradient of Sphingosine-1-Phosphate for Therapeutic Angiogenesis. Ann Biomed Eng. 2017;45(4):1003-14. doi: 10.1007/s10439-016-1768-2. PubMed PMID: 27904998.

207. Williams PA, Campbell KT, Silva EA. Alginate hydrogels of varied molecular weight distribution enable sustained release of sphingosine-1-phosphate and promote angiogenesis. J Biomed Mater Res A. 2018;106(1):138-46. doi: 10.1002/jbm.a.36217. PubMed PMID: 28875559.

208. Campbell KT, Hadley DJ, Kukis DL, Silva EA. Alginate hydrogels allow for bioactive and sustained release of VEGF-C and VEGF-D for lymphangiogenic therapeutic applications. PloS one. 2017;12(7):e0181484. doi: 10.1371/journal.pone.0181484. PubMed PMID: 28723974; PMCID: PMC5517064.

209. Nguyen M, Shing Y, Folkman J. Quantitation of angiogenesis and antiangiogenesis in the chick embryo chorioallantoic membrane. Microvasc Res. 1994;47(1):31-40. doi: 10.1006/mvre.1994.1003. PubMed PMID: 7517489.

210. Zijlstra A, Lewis JD, Zudaire E, Cuttitta F. The textbook of angiogenesis and lymphangiogenesis methods and applications. Dordrecht; New York: Springer; 2012.

211. Quent VM, Loessner D, Friis T, Reichert JC, Hutmacher DW. Discrepancies between metabolic activity and DNA content as tool to assess cell proliferation in cancer research. Journal of cellular and molecular medicine. 2010;14(4):1003-13. doi: 10.1111/j.1582-4934.2010.01013.x. PubMed PMID: 20082656; PMCID: PMC3823131.

212. Bellis SL. Advantages of RGD peptides for directing cell association with biomaterials. Biomaterials. 2011;32(18):4205-10. doi: 10.1016/j.biomaterials.2011.02.029. PubMed PMID: 21515168; PMCID: PMC3091033.

213. Le Saux G, Magenau A, Gunaratnam K, Kilian KA, Bocking T, Gooding JJ, Gaus K. Spacing of integrin ligands influences signal transduction in endothelial cells. Biophys J. 2011;101(4):764-73. doi: 10.1016/j.bpj.2011.06.064. PubMed PMID: 21843466; PMCID: PMC3175083.

214. Miyamoto S, Akiyama SK, Yamada KM. Synergistic roles for receptor occupancy and aggregation in integrin transmembrane function. Science. 1995;267(5199):883-5. PubMed PMID: 7846531.

215. Coussen F, Choquet D, Sheetz MP, Erickson HP. Trimers of the fibronectin cell adhesion domain localize to actin filament bundles and undergo rearward translocation. J Cell Sci. 2002;115(Pt 12):2581-90. PubMed PMID: 12045228.

216. Slater JH, Frey W. Nanopatterning of fibronectin and the influence of integrin clustering on endothelial cell spreading and proliferation. J Biomed Mater Res A. 2008;87(1):176-95. doi: 10.1002/jbm.a.31725. PubMed PMID: 18085648.

217. Arnold M, Cavalcanti-Adam EA, Glass R, Blummel J, Eck W, Kantlehner M, Kessler H, Spatz JP. Activation of integrin function by nanopatterned adhesive interfaces. Chemphyschem. 2004;5(3):383-8. doi: 10.1002/cphc.200301014. PubMed PMID: 15067875.

218. Koo LY, Irvine DJ, Mayes AM, Lauffenburger DA, Griffith LG. Co-regulation of cell adhesion by nanoscale RGD organization and mechanical stimulus. J Cell Sci. 2002;115(Pt 7):1423-33. PubMed PMID: 11896190.

219. Maheshwari G, Brown G, Lauffenburger DA, Wells A, Griffith LG. Cell adhesion and motility depend on nanoscale RGD clustering. J Cell Sci. 2000;113 (Pt 10):1677-86. PubMed PMID: 10769199.

220. Comisar WA, Hsiong SX, Kong HJ, Mooney DJ, Linderman JJ. Multi-scale modeling to predict ligand presentation within RGD nanopatterned hydrogels. Biomaterials. 2006;27(10):2322-9. doi: 10.1016/j.biomaterials.2005.10.037. PubMed PMID: 16316682.

221. Gotlieb AI. Atherosclerosis Cellular and Molecular Interactions in the Artery Wall1991.

222. Bates DO. Vascular endothelial growth factors and vascular permeability. Cardiovasc Res. 2010;87(2):262-71. doi: 10.1093/cvr/cvq105. PubMed PMID: 20400620; PMCID: PMC2895541.

VITA

Jenny B. Lin grew up in Lexington, Massachusetts. She obtained her undergraduate degree in Chemical and Biomolecular Engineering from Cornell University in 2010. During her undergraduate studies, she worked with Dr. Lawrence Bonassar in orthopedic biomedical engineering research, investigating the structure-to-function relationship of the joint lubricating glycosaminoglycan lubricin and a shorter recombinant form through atomic force microscopy. In addition to engaging in research, Jenny was a private tutor in general chemistry, physics, and biochemistry. After graduation, Jenny continued work as a private tutor in mathematics and science, while simultaneously completing 2 years of post-baccalaureate research at Boston University in the Biomimetic Materials Laboratory with Dr. Joyce Wong as a visiting scholar. It was through her studies in synthesizing micropatterned polymeric thermoresponsive surfaces for cell sheet tissue engineering that she developed a growing interest in regenerative medicine, focusing on biomaterial approaches.

In 2012, Jenny matriculated into the joint Medical Scientist Training Program at Indiana University School of Medicine and Purdue University. Jenny began her graduate education at Purdue University in the Weldon School of Biomedical Engineering in 2014 with Dr. Alyssa Panitch in the Laboratory for Engineered Therapeutics. She began her graduate research focusing on developing fluorescently tagged thermoresponsive nanoparticles for anti-inflammatory peptide delivery, with the goal of better understanding the mechanisms by which nanoparticles improved peptide efficacy. She also worked to develop acid-degradable and hollow nanoparticles to improve drug release profiles in the treatment of osteoarthritis and gained expertise in solid phase peptide synthesis. She later focused on the development and characterization of pro-angiogenic glycosaminoglycans for accelerating healing of chronic ischemic wounds, such as diabetic foot ulcers. In 2016, Jenny moved with the Panitch laboratory to the University of California, Davis, where she collaborated in pro-angiogenic studies to develop peptide-conjugated biomaterials promoting bone regeneration. She will finish her medical degree in 2020.

Jenny is active within her graduate Biomedical Engineering department and has served as the Treasurer and the first-year class representative in the Biomedical Engineering Graduate Student

Association (BMEGSA). Her PhD dissertation work was funded by a diabetes T32 award and the Clinical and Translational Sciences Institute (CTSI) through the NIH. In her final year at Purdue, Jenny was awarded the Purdue Bilsland Dissertation Fellowship.

PUBLICATIONS AND PRESENTATIONS

PUBLICATIONS

1) McMasters J*, Poh S*, **Lin JB**, and Panitch A. "Delivery of Anti-inflammatory Peptides from Hollow PEGylated Poly(NIPAM) Nanoparticles Reduces Inflammation in an Ex Vivo Osteoarthritis Model", *Journal of Controlled Release (2017),* doi:10.1016/j.jconrel.2017.05.008.

2) **Lin JB***, Poh S*, and Panitch A. "Controlled Release of Anti-Inflammatory Peptides from Reducible Thermosensitive Nanoparticles Suppresses Cartilage Inflammation", *Nanomedicine: Nanotechnology, Biology, and Medicine (2016),* doi:10.1016/j.nano.2016.05.010; *contributed equally to this work.

3) **Lin JB***, Phillips EH*, Riggins TE*, Sangha GS*, Chakraborty S, Lee JY, Lycke RJ, Hernandez CL, Soepriatna AH, Thorne BRH, Yrineo AA, and Goergen CJ. "Review: Imaging of Small Animal Peripheral Artery Disease Models: Recent Advancements and Translational Potential", *International Journal of Molecular Sciences (2015),* doi:10.3390/ijms160511131; *contributed equally to this work

4) Poh S, **Lin JB**, and Panitch A. "Release of anti-inflammatory peptides from thermosensitive nanoparticles with degradable cross-links suppresses pro-inflammatory cytokine production", *Biomacromolecules (2015),* doi: 10.1021/bm501849p.

5) **Lin JB**, Isenberg BC, Shen Y, Schorsch K, Sazonova OV, and Wong JY. "Thermo-responsive Poly(*N*-isopropylacrylamide) Grafted onto Microtextured Poly(dimethylsiloxane) for Aligned Cell Sheet Engineering", *Colloids and Surfaces B: Smart Biointerfaces* (2011), doi:10.1016/j.colsurfb.2011.10.040.

POSTER PRESENTATIONS

1) **Lin JB,** and Panitch A. “Developing an Angiogenic Proteoglycan Mimic for Ischemic Diabetic Foot Ulcer Repair”; Translational Sciences 2017, Washington DC; Apr 2017

2) **Lin JB,** and Panitch A. “Developing an Angiogenic Proteoglycan Mimic for Ischemic Diabetic Foot Ulcer Repair”; San Diego Glycobiology Symposium, San Diego, CA; Feb 2017

3) **Lin JB,** and Panitch A. “Developing an Angiogenic Proteoglycan Mimic for Ischemic Diabetic Foot Ulcer Repair”; Gordon Research Conference: Signal Transduction by Engineering Extracellular Matrices, New Biddeford, ME; June 2016

4) **Lin JB,** Poh S, and Panitch A. “Nanoparticles with Reducible Crosslinks for Anti-Inflammatory Drug Delivery in Osteoarthritis”; Biomedical Engineering Society, Tampa, FL; Oct 2015

5) **Lin JB**, and Panitch A. “Developing an Angiogenic Proteoglycan Mimic for Ischemic Diabetic Foot Ulcer Repair”; Diabetes Day Symposium, IUPUI, Indianapolis, IN; August 2015

6) **Lin JB**, and Panitch A. “Developing an Angiogenic Proteoglycan Mimic for Ischemic Diabetic Foot Ulcer Repair”; Gordon Research Conference: Tissue Repair and Regeneration, New London, NH; June 2015

7) **Lin JB***, Kim CJ*, and Lah MD; “Defiant Adolescent Behavior? No, The Mitochondrial Disease Dilemma”; American Medical Women’s Association Annual Meeting, Washington, DC; March 2014

8) **Lin JB*,** Kim CJ*, and Rohr-Kirchgraber T; “Anorexia Nervosa: An Unusual Cause of Hepatic Portal Venous Gas”; American Medical Women’s Association Annual Meeting, New York, NY; March 2013

9) **Lin JB**, Isenberg BC, Shen Y, Schorsch K, Sazonova OV, and Wong JY. “Thermo-responsive Poly(*N*-isopropylacrylamide) Grafted onto Microtextured Poly(dimethylsiloxane) for Aligned Cell Sheet Engineering”; Tissue Engineering and Regenerative Medicine International Society – North America 2011 Conference, Houston, TX; 11-14 Dec 2011

10) **Lin JB**, Galley NM, and Bonassar LJ. “Characterization of Lubricin through Atomic Force Microscopy”; Engineering Learning Initiatives Symposium, Cornell University, Ithaca, NY; Feb 2009